

LARGE-SCALE ASSEMBLY OF COLLOIDAL PARTICLES

By

HONGTA YANG

A DISSERTATION PRESENTED TO THE GRADUATE SCHOOL  
OF THE UNIVERSITY OF FLORIDA IN PARTIAL FULFILLMENT  
OF THE REQUIREMENTS FOR THE DEGREE OF  
DOCTOR OF PHILOSOPHY

UNIVERSITY OF FLORIDA

2011

© 2011 Hongta Yang

To my family, who, always support all my efforts especially for my PhD

## ACKNOWLEDGMENTS

I would like to express my deepest appreciation to Professor Peng Jiang, who served as my research supervisor over the past three years, showing me different ways to approach and resolve many challenging research problems, and continuously giving me tolerance, encouragement and advice in my research work. With his broad knowledge, diligent working attitude, and optimistic and kind spirit in daily life, Professor Peng Jiang acted not only as an academic mentor, but also as a good friend who impacted me in my future career. My special thanks go to Professor Ranga Narayanan, Professor Sergey Vasenkov, and Professor Paul Holloway for actively participating in my committee. I am grateful to National Science Foundation for financial support of this research.

My appreciation to Dr. Chih-Hung Sun, who gave me lots of suggestions and assistance in my research, is beyond my expression. My great thanks are given to Professor Xuefeng Liu, for his kindly assistance in my research work. I am indebted to my fellow colleagues, Dr. Nicholas Linn, Dr. Wei-Lun Min, Dr. In-Kook Jun, and Dr. Tzung-Hua Lin, who always helped me in the lab. It would have been impossible to complete this work without their efforts.

Finally, and most importantly, I express my thanks and gratitude to my parents, my wife, and my son, who have always supported me in spirit along this journey. They gave me the courage to pursue my dreams, and encouraged me to be a successful researcher with an aggressive attitude in life and work. I am always going to be grateful for having them by my side.

## TABLE OF CONTENTS

	<u>page</u>
ACKNOWLEDGMENTS.....	4
LIST OF FIGURES.....	7
ABSTRACT .....	11
CHAPTER	
1 INTRODUCTION.....	14
1.1 Top-Down and Bottom-Up Fabrication.....	14
1.2 Colloidal Self-Assembly .....	15
1.3 Color Reflective Displays .....	16
1.4 Vapor Detectors .....	18
1.5 Smart Windows.....	19
1.6 Superhydrophobic and Self-Cleaning Coatings .....	20
1.7 Particle Separations and Bacteria Filtrations .....	21
2 SELF-ASSEMBLY OF COLLOIDAL CRYSTALS BY DOCTOR BLADE COATING .....	26
2.1 Experimental Procedure .....	26
2.2 Results and Discussion.....	28
3 HEAT PIPE-INSPIRED COLOR REFLECTIVE DISPLAYS .....	44
3.1 Experimental Procedure .....	45
3.2 Results and Discussion.....	46
4 MACROPOROUS PHOTONIC CRYSTAL-BASED VAPOR DETECTORS .....	57
4.1 Experimental Procedure .....	58
4.2 Results and Discussion.....	59
5 SELF-ADJUSTING SMART WINDOWS .....	66
5.1 Experimental Procedure .....	66
5.2 Results and Discussion.....	67
6 SELF-CLEANING DIFFRACTIVE MACROPOROUS FILMS .....	72
6.1 Experimental Procedure .....	72
6.2 Results and Discussion.....	74

7	PARTICLE SEPARATIONS AND BACTERIA FILTRATIONS BY MACROPOROUS MEMBRANES .....	87
	7.1 Experimental Procedure .....	87
	7.2 Results and Discussion.....	89
8	CONCLUSIONS AND RECOMMENDATIONS .....	95
	8.1 Heat-Pipe Inspired Color Reflective Displays .....	95
	8.2 Vapor Detections .....	95
	8.3 Smart Windows.....	96
	8.4 Superhydrophobic and Self-Cleaning Coatings .....	96
	8.5 Particle Separations and Bacteria Filtrations .....	96
	8.6 Recommendations .....	97
	LIST OF REFERENCES .....	98
	BIOGRAPHICAL SKETCH.....	110

## LIST OF FIGURES

<u>Figure</u>	<u>page</u>
1-1 A flowchart describes the self-assembly approach.....	22
1-2 Photograph of a spin-coated silica/polymer composite.....	23
1-3 Scheme of heat pipe mechanism .....	23
1-4 Photograph of a blue morpho butterfly .....	24
1-5 Switching sequence of an electrochromic laminated glass.....	24
1-6 Photograph of lotus leaves .....	25
1-7 SEM image of a filtration membrane prepared by heavy ion track etching technology .....	25
2-1 Schematic illustration of the experimental setup for assembling large-area colloidal crystal/polymer composites by using a simple doctor blade coating technique.....	37
2-2 Colloidal crystal/polymer composites fabricated by the doctor blade coating technique.....	38
2-3 Thickness dependence of the doctor blade coated colloidal crystal/ETPTA composites on the coating speed and particle volume fraction.....	39
2-4 Schematic illustration of the velocity profile and the pressure head in the doctor blade coating process.....	40
2-5 Relative viscosity of 330 nm silica spheres/ETPTA suspensions with different particle volume fractions at various shear rates.....	40
2-6 Cross-sectional SEM image of a silica colloidal crystal after removing the ETPTA matrix by 10 min of oxygen plasma etching. ....	41
2-7 Macroporous polymer membrane after the selective removal of templating silica spheres.....	41
2-8 Normal incidence optical reflection spectra of an ETPTA/silica colloidal crystal composite, a corresponding macroporous ETPTA film, and a released silica colloidal crystal with 290 nm spheres and 12 colloidal layers.....	42
2-9 Schematic illustration of the dual-blade setup, and photograph of a multilayer composite consisting of 290 nm silica spheres embedded in an ETPTA matrix aligned by a dual-blade system at a coating speed of 1 mm/s.....	43

3-1	Schematic illustration of the experimental setup for heat pipe-inspired color reflective displays. ....	49
3-2	Working principle of macroporous polymer reflective color displays.....	50
3-3	Patterned macroporous polymer reflective color displays .....	51
3-4	Two-color displays are feasible by a macroporous polymer membrane.....	52
3-5	Two-color displays are feasible by a macroporous polymer membrane. ....	53
3-6	Multi-color displays are feasible by fabricating macroporous polymer films with stacked air cavities of different sizes.....	54
3-7	Protocol of an electrically driven reflective color display. The macroporous polymer is with 280 nm sized pores.....	54
3-8	Protocol of an electrically driven reflective color display. The patterned macroporous polymer is with 330 nm sized pores.....	55
3-9	Full-color reflective displays are feasible by introducing solvent with higher refractive index. ....	55
3-10	Proof-of-concept experiment demonstrates the feasibility of constructing reflective color displays on curve surface. ....	56
4-1	Schematic illustration of the experimental setup for vapor detection. ....	62
4-2	SEM image of a doctor blade coated silica colloidal crystal/polymer composite and a templated macroporous polymer film .....	63
4-3	Specular reflection spectra obtained from a macroporous polymer film exposed to ethanol vapors with different partial pressures.....	63
4-4	Time dependence of specular reflection spectra obtained from a macroporous polymer film exposed to ethanol vapor with a partial pressure of 0.5 P <sub>0</sub> .....	64
4-5	Calculated volume fractions of air and the corresponding adsorbed ethanol layer thickness and simulated specular reflection spectra obtained from a macroporous polymer film exposed to ethanol vapors with different partial pressures.....	64
4-6	Dependence of $\ln P/P_0$ vs. the reciprocal of the radius of curvature of the condensed liquid films. ....	65
4-7	Specular reflection spectra obtained from a macroporous polymer film exposed to water vapors with different partial pressures, and dependence of the wavelength shift of the Bragg diffraction peak vs. water partial pressure. ....	65

5-1	Schematic illustration of the methodology for self-adjusting smart windows. ....	69
5-2	SEM image of a doctor blade coated silica colloidal crystal-polymer composite and a templated macroporous film .....	70
5-3	Optical reflection spectra showing the color change process when the air cavities of macroporous polymer are gradually replaced by ethanol .....	70
5-4	Schematic illustration of the prove-of-concept experimental setup for self-adjusting smart windows. ....	71
5-5	Ice cubic temperatures under different windows vs. exposure time.....	71
6-1	Schematic illustration of the experimental procedures for preparing superhydrophobic macroporous polymer films. ....	81
6-2	Top-view SEM images of macroporous ETPTA films templated from 260 nm silica spheres. These films were prepared by plasma etching a doctor blade coated composite for different time, followed by selective removal of the templating silica spheres .....	82
6-3	Dependence of the void size of macroporous ETPTA films templated from 260 nm silica spheres vs oxygen RIE etching durations.....	83
6-4	Water drop profiles on fluorosilane-modified macroporous ETPTA films after oxygen plasma etching, and apparent water contact angles of fluorosilane-modified macroporous ETPTA films etched at different RIE durations. ....	83
6-5	Advancing and receding water contact angles, and sliding angles of fluorosilane-modified macroporous ETPTA film etched at different RIE durations.....	84
6-6	Dependence of the apparent water contact angle vs the fraction of solid/liquid interface.....	84
6-7	Photograph of bacterial cultures on four specimens after applying an inclining angle of 5o for 5 seconds .....	85
6-8	Counts of the colony forming units for four specimens after applying an inclining angle of 5o for 5 seconds. ....	85
6-9	Experimental and SWA-simulated optical reflection spectra at normal incidence from a macroporous ETPTA film with 260 nm air cavities and 12 layers, and comparison of normal-incidence optical reflection spectra from macroporous ETPTA films etched at different RIE durations.. ....	86
7-1	Separation of 10 nm gold nanoparticles from 330 nm silica spheres by using a free-standing, macroporous ETPTA membrane filter .....	92

7-2	Comparison of the extinction spectra of the 10 nm gold nanoparticles solutions, and calibration curve for calculating the concentration of gold nanoparticles in filtrate solutions.....	93
7-3	Schematic illustration of the bacteria filtration process.....	93
7-4	Photograph of bacterial cultures on three specimens before and after bacteria filtration. ....	94

Abstract of Dissertation Presented to the Graduate School  
of the University of Florida in Partial Fulfillment of the  
Requirements for the Degree of Doctor of Philosophy

## LARGE-SCALE ASSEMBLY OF COLLOIDAL PARTICLES

By

Hongta Yang

May 2011

Chair: Peng Jiang  
Major: Chemical Engineering

This study reports a simple, roll-to-roll compatible coating technology for producing three-dimensional highly ordered colloidal crystal-polymer composites, colloidal crystals, and macroporous polymer membranes. A vertically beveled doctor blade is utilized to shear align silica microsphere-monomer suspensions to form large-area composites in a single step. The polymer matrix and the silica microspheres can be selectively removed to create colloidal crystals and self-standing macroporous polymer membranes. The thickness of the shear-aligned crystal is correlated with the viscosity of the colloidal suspension and the coating speed, and the correlations can be qualitatively explained by adapting the mechanisms developed for conventional doctor blade coating.

Five important research topics related to the application of large-scale three-dimensional highly ordered macroporous films by doctor blade coating are covered in this study. The first topic describes the invention in large area and low cost color reflective displays. This invention is inspired by the heat pipe technology. The self-standing macroporous polymer films exhibit brilliant colors which originate from the

Bragg diffractive of visible light from the three-dimensional highly ordered air cavities. The colors can be easily changed by tuning the size of the air cavities to cover the whole visible spectrum. When the air cavities are filled with a solvent which has the same refractive index as that of the polymer, the macroporous polymer films become completely transparent due to the index matching. When the solvent trapped in the cavities is evaporated by in-situ heating, the sample color changes back to brilliant color. This process is highly reversible and reproducible for thousands of cycles.

The second topic reports the achievement of rapid and reversible vapor detection by using 3-D macroporous photonic crystals. Capillary condensation of a condensable vapor in the interconnected macropores leads to the increase of the effective refractive index of the diffractive medium, resulting in the red-shift of the optical stop bands. The wavelength shift is linearly proportional to the vapor partial pressure for a spectrum of vapors. Optical simulation and theoretical prediction based on Kelvin equation suggest that a liquid film is formed on the walls of the macropores during vapor condensation.

The third topic describes introducing doctor blade coating fabricated large area and low cost macroporous films for thermochromic smart windows, which are useful for energy control in glazed buildings. The fabricated macroporous polymer films exhibit brilliant colors and are capable of reflecting solar radiation when in-situ heated, and become transparent as cavities are filled with a solvent which has the same refractive index as that of the polymer when cooled to building temperature.

The fourth topic reports the roll-to roll fabricated excellent water-repelling and self-cleaning macroporous polymer films. The size of the voids can be easily controlled by tuning the duration of an oxygen reactive-ion etching process prior to the removal of the

templating silica spheres from silica colloidal-polymer composites. After surface functionalization with fluorosilane, superhydrophobic surface with large apparent water contact angle and small sliding angle can be obtained. The self-cleaning functionality can be achieved on superhydrophobic macroporous coatings by preventing bacterial contamination is further demonstrated.

The fifth topic presented is that the template macroporous polymer films with interconnected voids and uniform interconnecting nanopores can be directly used as filtration membranes to achieve size-exclusive separation of particles. The results also demonstrate that more than 85% of small sized particles are recovered after filtration. The results also demonstrate that *Escherichia coli* can be filtrated by the from macroporous polymer films aqueous solution.

## CHAPTER 1 INTRODUCTION

### 1.1 Top-Down and Bottom-Up Fabrication

Top-down fabrication has been widely used in the semiconductor industry to fabricate cheap and fast electronic devices which are the hallmark of modern life and technology. Photolithography is the most commonly used top-down technology to fabricate three dimensional components. Due to the light diffraction limit, feature sizes smaller than the wavelength of light cannot be achieved by conventional photolithography.<sup>1</sup> Lithography techniques such as extreme ultraviolet light or soft X-rays lithography, electron beam lithography, and dip pen lithography have been used to generate smaller patterns.<sup>2</sup> These high cost and low throughput techniques cannot be used for mass production and are only lab-oriented processes. Another challenge of top down fabrication is the choice of materials. The use of short wavelength as the exposure light source and smaller features size requires materials with suitable optical and mechanical properties.

Aside from top-down engineering technique, bottom-up nanofabrication offers a new paradigm for material fabrication. Complex structures found in nature are assembled with building blocks like atoms, protein, RNA and DNA. The self assembly building blocks can be made by organic, inorganic, polymeric and hybrid materials. Building blocks can be assembled into spheres and cubes, sheets and discs, wires and tubes, rings and spirals with nm to cm dimensions. A flowchart describing the ideas of self assembly is shown in Figure 1-1.

## 1.2 Colloidal Self-Assembly

The ability to synthesize monodisperse latex and silica nanoparticles by heterogeneous emulsion polymerizations and sol-gel chemistry, respectively with diameters in the range of tens of nanometer to several micrometers provides a new class of materials with a range of applications in chemistry and physics. A variety of methods, such as gravitational sedimentation,<sup>3-4</sup> template assisted assembly,<sup>5-7</sup> electrostatic repulsion,<sup>8-10</sup> electric field induced assembly,<sup>11-12</sup> robotic manipulation,<sup>13</sup> Langmuir-Blodgett deposition,<sup>14</sup> spin coating and capillary forces induced convective self-assembly,<sup>15-17</sup> have been developed to create both three-dimensional and two-dimensional colloidal crystals.

The application of the colloidal crystal has been widely exploited recently. One of the most appealing properties of these periodic dielectric lattices is three-dimensional photonic crystals behavior.<sup>18-20</sup> Colloidal crystals can function as the optical analog of the electronic semiconductor. The three-dimensional colloidal crystal can also be used as a template for preparation of three-dimensionally ordered porous replicas, which are known as inverse opals. A wide variety of macroporous materials based on colloidal templates have been synthesized. The applications of these inverse opals include chemical and biological sensors,<sup>21-23</sup> simultaneous chromatographic separation,<sup>24</sup> optical sensing, power storage and generation,<sup>25</sup> low-threshold laser,<sup>26</sup> and full color displays.<sup>27</sup>

Monolayer colloidal crystal can be used for lithographic patterning of surfaces, projection lithography, micromolds and surface relief patterns.<sup>28</sup> Nanostructures such as nanodots, nanorings, nanoprisms, nanoholes, nanobowls, nanocrescent and hollow spheres nanostructures can be fabricated by two-dimensional lithography. Applications

include optical antennas, catalysts, chemical and biological sensors.<sup>29-32</sup> The sizes, periodicities, and materials of these nanostructures can be controlled by adjusting the size of the colloidal templates and the filling materials from organic, inorganic to polymeric materials.

To resolve the scale-up and compatibility issues of current colloidal self-assembly, a spin-coating technology has recently been developed.<sup>33-35</sup> The methodology is based on shear aligning concentrated colloidal suspensions by using standard spin-coating equipment. Spin-coating enables the rapid production of wafer-sized colloidal arrays with remarkably large domain sizes and unusual non-close-packed structures. However, this scalable technology is still a batch process. Compared with continuous process, the batch process is with lower productivity, higher costs, and less efficiency, which limits the applications. For industrial-scale mass production, a roll-to-roll compatible, continuous process is highly desired. Additionally, the shear force direction changes circularly in the spin-coating process. This leads to the formation of six-arm diffraction patterns on the sample surface (Figure 1-2),<sup>36-38</sup> impeding many optical applications (e.g., displays and optical filters) that require a uniform diffractive color.

### **1.3 Color Reflective Displays**

In the information-rich world, it is becoming increasingly important to develop technologies capable of displaying dynamic and changeable data, for reasons ranging from value-added advertising to environmental sustainability. There is an intense drive at the moment towards ultrathin displays, devices having a high reflectivity and contrast to provide viewability in a variety of environments, particularly in sunlight where emissive or backlight devices perform very poorly. The list of possible technologies is extensive, including electrophoresis, chiral nematic liquid crystals, electrochromism,

electrodewetting, interferometric, and more. Despite tremendous advances, the key drawback of all these existing display options relates to color. As soon as an RGB (red, green, and blue) color filter or spatially modulated color scheme is implemented, substantial light losses are inevitable even if the intrinsic reflectivity of the material is very good.

Photonic crystals materials with a periodic modulation in refractive index can be sources of exceptionally bright and brilliant reflected colors arising from coherent Bragg optical diffraction.<sup>39</sup> Exemplified by gemstone opals, three-dimensional photonic crystals are readily available by means of colloidal self-assembly, making them a fertile test-bed for investigating concepts based on tunable structural color. A variety of methods have been developed to create colloidal photonic crystals.<sup>3-17</sup> However, current colloidal self-assemblies are only favorable for low volume, laboratory-scale production. It usually takes days or even weeks to grow a centimeter-size colloidal crystal.<sup>40-42</sup> Another major issue is the limitation on achievable crystal structures. The realization of photonic crystals by self-assembly is challenging.<sup>43</sup> Even more challenging is the creation of photonic crystals with arbitrary defects that enable photons to enter the band gap.<sup>44</sup> These drawbacks and challenges greatly impede the mass-fabrication and on-chip integration of practical photonic crystal devices.

Three-dimensional ordered macroporous polymers offer a route to solve the problem. Synthetic preparations for colloidal crystals with low dispersity are well-developed, and their self-assembly into a close-packed ordered structure leaves a void volume of 26% available for further material infiltration or modification.<sup>45-46</sup> Tuning of colloidal PC optical properties has been effected by the infilling of metals, insulators,

semiconductors and polymers of all types, and by the inversion of such constructs through removal of the template spheres. Recently, we developed a new concept, inspired by heat pipe mechanism (Figure 1-3), that realizes color tunable displays by using macroporous polymer membranes. Macroporous membranes with three-dimensionally ordered voids are prepared from self-assembled colloidal crystal/polymer matrices, followed by removing particles. The resulting films exhibit brilliant iridescent colors due to the Bragg diffraction of visible light by the periodic voids. The voids can be filled up by a refractive index-matched liquid using controlled capillary condensation, resulting in transparent films with no reflective colors. By using this simple and inexpensive approach, it demonstrates that color reflective displays can be manufactured.

#### **1.4 Vapor Detectors**

Mesoporous membranes, such as two-dimensional porous silicon and one-dimensional titania photonic crystals, have been widely used in sensitive vapor detection.<sup>47-60</sup> By monitoring the change of the optical properties (e.g., wavelength shift of the photonic band gaps or the Fabry-Perot fringes) of the diffractive media during vapor condensation, the concentration of the vapors can be deduced. Blue-colored Morpho butterfly wing scales (Figure 1-4), which are intrinsic three-dimensional photonic crystals exhibiting unique optical diffraction and interference, have also been demonstrated for highly selective vapor detection.<sup>61</sup> However, the limited size and material selection of these natural photonic crystals impede the development of reproducible and reusable vapor detectors. Therefore, three-dimensional macroporous polymer photonic crystals created by an inexpensive and scalable bottom-up technology enable the rapid and reversible detection of a wide range of vapors is desired. The

capillary condensation of vapors in the submicrometer-scale macropores, a topic that has received little examination,<sup>62-65</sup> has also been investigated by both experiments and theoretical calculations.

### **1.5 Smart Windows**

Windows are often regarded as a less energy efficient building component with a larger maintenance requirement. Nevertheless, their technology has grown by leaps over the last several years. A new class of windows promises to set the technology bar even higher. Dynamic tintable or the so-called smart windows, where an example is shown in Figure 1-5, can change properties such as the solar factor and the transmission of radiation in the solar spectrum in response to an electric current or to the changing environmental conditions themselves.<sup>66-68</sup> The application of such windows may lead towards a drastic reduction of the energy consumption of highly glazed buildings by reducing cooling loads, heating loads and the demand for electric lighting.

Various techniques are known to derive switchable windows.<sup>69-70</sup> However, taking into account the specific properties of window glazing in buildings, one strict rule has to be reckoned with: A transparent mode of the glazing has to be possible. Presently, three different technologies with external triggering signal are commonly known for this purpose and start to be available on the market: Chromic materials,<sup>71-76</sup> liquid crystals,<sup>77-80</sup> and electrophoretic or suspended-particle devices.<sup>81-82</sup> Here, the chromic devices may be divided in four categories, i.e. electrochromic,<sup>83-85</sup> gasochromic,<sup>86-87</sup> photochromic,<sup>88-90</sup> and thermochromic devices,<sup>91</sup> where the last two possibilities will respond automatically to, respectively, changes in light and temperature.

Smart windows are to be judged on several specific factors. Of most importance is their transmittance modulation range in the visible and whole solar spectrum. The modulation range is often expressed for a single wavelength in literature, but this gives little or no information on the overall performance of the smart device. Secondly, the expected lifetime and number of achieved cycles without or only minor degradation are of uttermost importance. Thirdly, the switching time for colouration and bleaching is important, mostly expressed as the time necessary to reach 90% of its maximum modulation range. The magnitude of the switching time is strongly connected to the size of the device, as large devices tend to have long switching times. Furthermore, the achieved window size, the total energy consumption, the operating voltage and the operating temperature range are of importance.

### **1.6 Superhydrophobic and Self-Cleaning Coatings**

Inspired by the unique water-repelling property of lotus leaves (Figure 1-6), superhydrophobic coatings with large water contact angle ( $>150^\circ$ ) and small sliding angle ( $<10^\circ$ ) have attracted great recent interests.<sup>92-97</sup> These biomimetic coatings are of considerable technological importance in developing self-cleaning surfaces,<sup>98</sup> antifouling substrates,<sup>98</sup> antifogging coatings,<sup>99-100</sup> efficient microfluidic devices,<sup>101-102</sup> bioseparation media,<sup>103</sup> anticorrosive coatings,<sup>104-105</sup> and more. A large variety of technologies, such as layer-by-layer (LBL) assembly,<sup>98,106-108</sup> lithography,<sup>108-111</sup> phase separation,<sup>112-113</sup> electrospinning,<sup>114-116</sup> plasma etching,<sup>100,117</sup> and electrochemical treatment,<sup>118-119</sup> have been developed to create superhydrophobic coatings. As air is the most hydrophobic material, porous coatings with a large fraction of entrapped air have been widely exploited to control the wettability of the films. Various methodologies, like LBL assembly of nanoparticles and polyelectrolytes,<sup>98,107</sup> breath figure-based assembly,<sup>120-</sup>

<sup>121</sup> block copolymer microphase separation, <sup>122-123</sup> glancing angle deposition, <sup>124</sup> sol-gel processing, <sup>125-129</sup> template-assisted nanofabrication, <sup>130-134</sup> and electron irradiation of composites, <sup>135-137</sup> have been demonstrated to produce superhydrophobic porous coatings.

Spontaneous crystallization of colloidal particles is a simple, fast, and inexpensive approach for creating water-repellent coatings. <sup>138-149</sup> The self-assembled colloidal arrays can also be used as template to create superhydrophobic macroporous films. <sup>150-153</sup> These macroporous films with crystalline arrays of voids are intrinsic photonic crystals and are of great technological importance in developing diffractive optical devices for all-optical integrated circuits. <sup>154-155</sup> Polymeric macroporous membranes with interconnecting voids have also been demonstrated as separation media for macromolecules and DNA <sup>156-157</sup> and biosensors. <sup>158</sup> Unfortunately, most of the current colloidal self-assembly and templating technologies are not compatible with standard industrial fabrication and only favorable for low volume, laboratory scale production. It is highly desirable to develop a roll-to-roll compatible bottom-up technology for large-scale production of multifunctional macroporous coatings with unique self-cleaning, optical, and size-exclusive separation functionalities.

### **1.7 Particle Separations and Bacteria Filtrations**

Membrane filtrations are widely utilized in a large variety of separation applications, such as water treatment, <sup>159-160</sup> pollution removal, <sup>161</sup> filtration of aqueous solution (such as cell culture media, serum, enzyme and water), <sup>162-165</sup> removal of bacteria and debris, <sup>166-167</sup> filtration of organic solution, <sup>168</sup> and so on. They are also routinely used in chemical, biological, medical, and agriculture laboratories. <sup>169-171</sup> One important parameter that controls the separation efficiency is the pore size and size

distribution of the membrane filters. Filters with nanometer-scale pore size and tight size control, are very useful in biological separation (e.g., removal of virus). Heavy ion track etching is a commercial technology for producing membrane filters (Figure 1-7) with well-defined pore size, shape, and density.<sup>172-175</sup> However, heavy ion accelerators are required to create such filters and the fabrication cost is high. Therefore, a much economic and scalable nanomanufacturing technology for creating large-area filtration membranes with well-defined pore sizes (in the nanometer-scale) and size distribution is highly desired.

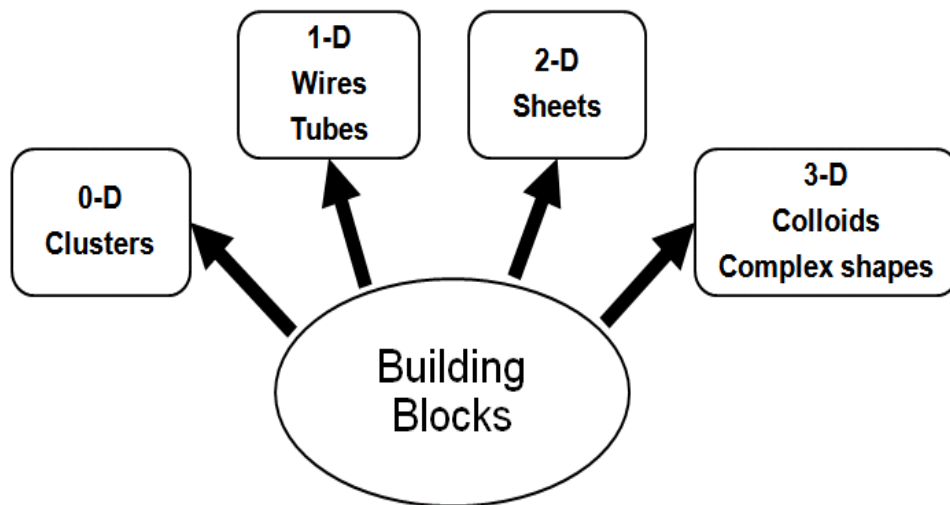


Figure 1-1. A flowchart describes the self-assembly approach.<sup>1</sup>

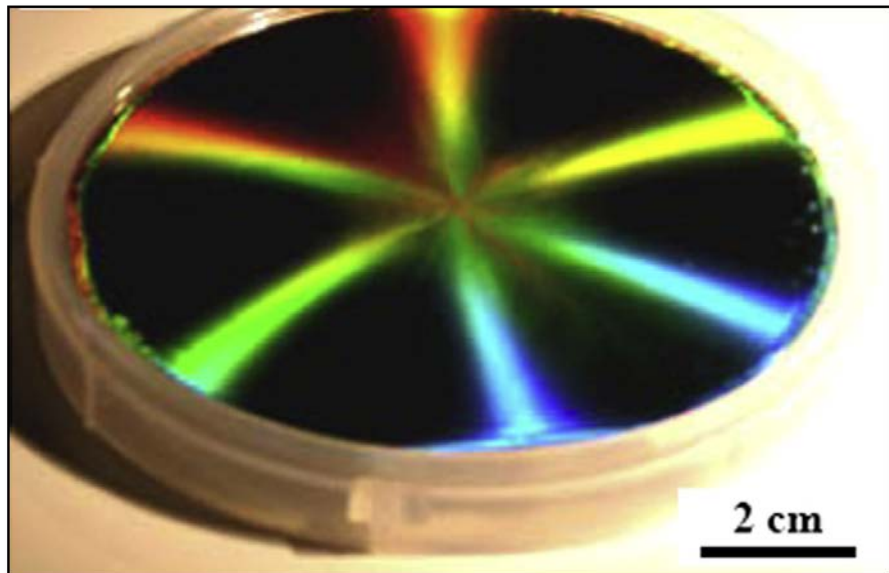


Figure 1-2. Photograph of a spin-coated silica/polymer composite illuminated with white light.<sup>33</sup>

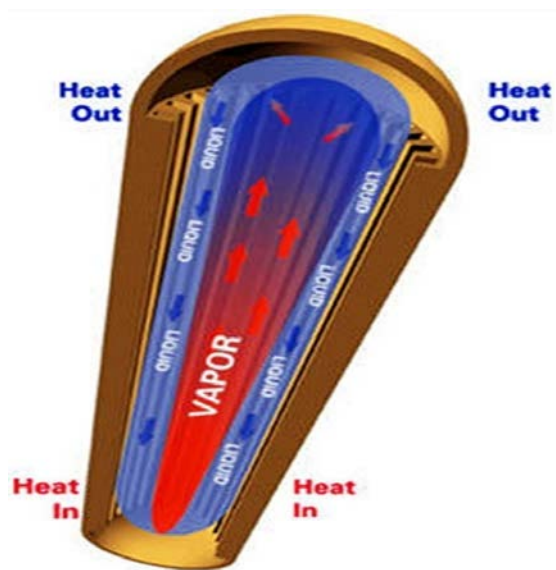


Figure 1-3. Scheme of heat pipe mechanism.<sup>44</sup>



Figure 1-4. Photograph of a blue morpho butterfly.<sup>54</sup>

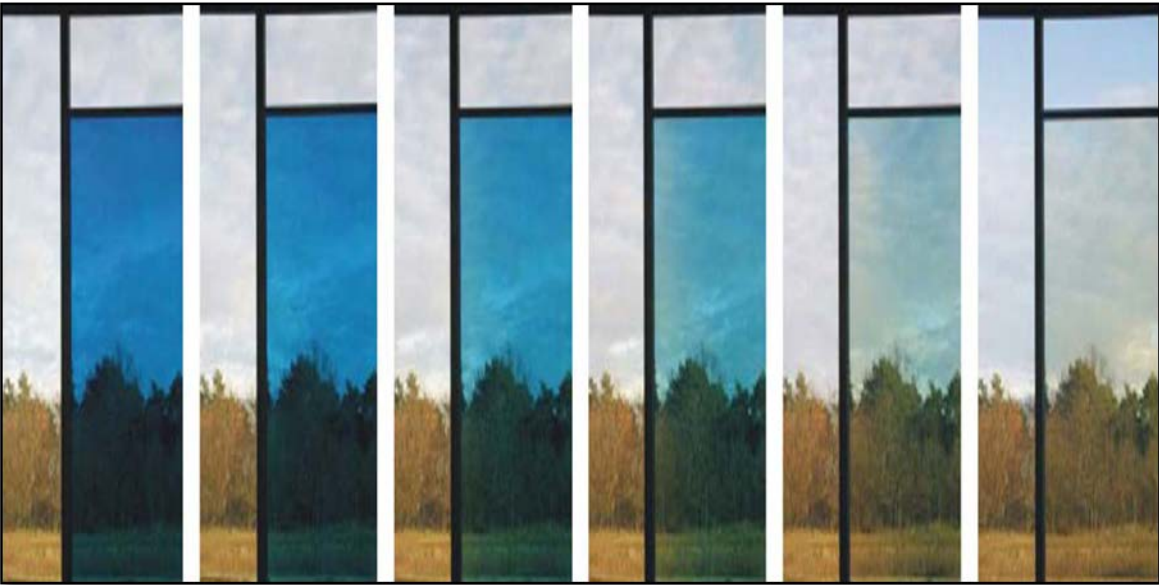


Figure 1-5. Switching sequence of an electrochromic laminated glass.<sup>70</sup>



Figure 1-6. Photograph of lotus leaves.<sup>92</sup>

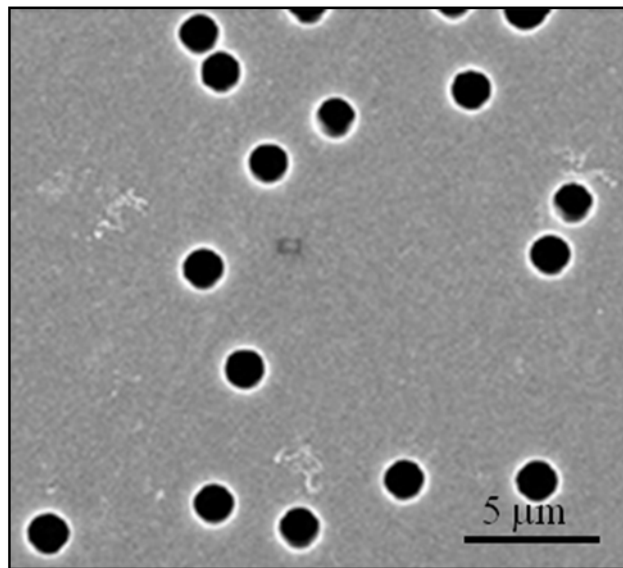


Figure 1-7. SEM image of a filtration membrane prepared by heavy ion track etching technology.<sup>170</sup>

## CHAPTER 2 SELF-ASSEMBLY OF COLLOIDAL CRYSTALS BY DOCTOR BLADE COATING

Doctor blade coating (DBC) is widely used in the textile, paper, photographic film, printing, and ceramic industries to create highly uniform flat films over large areas.<sup>176-180</sup> In DBC, an immobilized blade applies a unidirectional shear force to a slurry that passes through a small gap between the blade and the substrate. This process is roll-to-roll compatible and has played a crucial role in ceramic processing to produce thin, flat ceramic tapes for dielectrics, fuel cells, batteries, and functionally graded materials.<sup>176</sup> Velev et al. developed a simplified DBC process,<sup>181</sup> which originated from an evaporative colloidal assembly technology,<sup>182-184</sup> to create colloidal crystals with thickness ranging from a monolayer to a few layers. Capillary force is the major driving force for colloidal crystallization in this process. Inspired by this technology, we here report a roll-to-roll compatible DBC technology for producing highly ordered colloidal crystal polymer composites, colloidal crystals, and macroporous polymer membranes. The resulting three-dimensional ordered structures exhibit uniform diffractive colors. It is also demonstrated that the template macroporous membranes with interconnected voids and uniform interconnecting nanopores can be directly used as filtration membranes to achieve the size-exclusive separation of particles.

### **2.1 Experimental Procedure**

A The synthesis of monodisperse silica microspheres with less than 5% diameter variation is performed by following the well established Stober method.<sup>185</sup> The purified silica microspheres (by multiple centrifugation/redispersion cycles in 200 proof ethanol) are redispersed in Ethoxylated trimethylolpropane triacrylate (ETPTA) monomer using a Thermolyne vortex mixer. Darocur 1173 (2 wt %) is added as the photoinitiator. The

final particle volume fraction of colloidal suspensions is adjusted from 20 to 50%. After filtration through a 5  $\mu\text{m}$  syringe filter (Whatman<sup>®</sup>) to remove any large particles, the transparent viscous solution is stored in an open vial in the dark overnight to allow any residual ethanol to evaporate.

An immobilized 90<sup>°</sup>-beveled razor blade (Fisher<sup>®</sup>, 4 cm wide) is gently placed on a substrate. One milliliter of the above silica-ETPTA suspension is dispensed along one sidewall of the blade onto the substrate. The substrate is dragged by a syringe pump at a controlled speed. The blade can then spread the colloidal suspension uniformly on the substrate. After DBC, the sample is transferred to a pulsed UV curing system and ETPTA monomer is rapidly polymerized by exposure to UV radiation for 4 seconds. The polymer matrix can be removed by using a reactive ion etcher operating at 40 mTorr oxygen pressure, a 40 sccm flow rate, and 100 W for 10 min. To prepare macroporous polymers, the silica/ETPTA composites are immersed in a 2 vol % hydrofluoric acid aqueous solution for 30 min, then rinsed with DI water, and finally dried in a stream of nitrogen.

Experiments are performed using 50-mm-diameter parallel-plate geometry to characterize the rheological properties of the colloidal suspensions under shear. The gap between plates is set to 500  $\mu\text{m}$  in all experiments. To ensure that each test began from a similar initial state, the suspensions are presheared at a rate of 100  $\text{s}^{-1}$  for 300 seconds, which is sufficient to enable the suspension to reach a steady state. The temperature is maintained at 25  $^{\circ}\text{C}$ , and the temperature fluctuation is less than 0.05  $^{\circ}\text{C}$  during a typical test.

An Ocean Optics<sup>®</sup> spectrometer with a reflection probe is used for reflectance measurements. A calibrated halogen light source is used to illuminate the sample. The beam spot size is about 3 mm on the sample surface. Measurements are performed at normal incidence, and the cone angle of collection is less than 5°. Absolute reflectivity is obtained as a ratio of the sample spectrum to the reference spectrum. The reference spectrum is the optical density obtained from an aluminum-sputtered (1000 nm thick) silicon wafer. The final value of the absolute reflectivity is the average of several measurements obtained from different spots on the sample surface.

## **2.2 Results and Discussion**

The schematic illustration of the DBC process for fabricating three-dimensional highly ordered colloidal crystal/polymer composites is shown in Figure 2-1. Monodisperse silica microspheres synthesized by the Stober method are first dispersed in a nonvolatile monomer, ethoxylated trimethylolpropane triacrylate (ETPTA, M.W. 428, viscosity 60 cps), with 2 wt % Darocur 1173 as the photoinitiator. The particle volume fraction is adjusted from 20 to 50%. The resulting colloidal suspensions are transparent because of refractive index (RI) matching between silica microspheres (RI ~ 1.42) and ETPTA monomer (RI ~1.46). The electrostatic repulsion between silica microspheres (zeta potential of ca. -45 mV in ETPTA)<sup>186</sup> stabilizes the suspensions for at least a few weeks. The suspensions are then dispensed along a sidewall of an immobilized, vertically beveled razor blade that gently touches a substrate. A large variety of substrates, including glass microslides, silicon wafers, and plastic plates, can be used. The substrate is then dragged by a syringe pump at a controlled speed ranging from ~0.1  $\mu\text{m/s}$  to >1 mm/s. The razor blade offers a uniform shear force for aligning the

suspended silica colloidal microspheres. The ETPTA monomer is finally photopolymerized by exposure to ultraviolet radiation to form three-dimensional highly ordered colloidal crystal/polymer composites.

Figure 2-2A shows a photograph of a multilayer silica colloidal crystal-ETPTA composite consisting of 290 nm silica microspheres on a glass substrate illuminated with white light. The sample is prepared by doctor blade coating a 50 vol % suspension at 0.1  $\mu\text{m/s}$ . It exhibits a uniform red color caused by Bragg diffraction of visible light from the crystalline lattice. The long range ordering of silica microspheres is clearly evident from the typical top-view SEM image as shown in Figure 2-2B. The hexagonally arranged sharp peaks in the Fourier transform of a low magnification SEM image (inset of Figure 2-2B) further confirm the long-range hexagonal order. Common defects, such as point vacancies and misaligned lines that are caused mostly by dust particles and silica microspheres with extreme sizes, are also apparent in the SEM image. The polymer matrix surrounding the silica microspheres is clearly seen from the magnified top-view SEM image in Figure 2-2C. The interparticle distance of the colloidal crystal is calculated by the pair correlation function (PCF, Figure 2D),  $g(r)$ , which is obtained from a low-magnification image such as that in Figure 2-2B as

$$g(r) = \frac{1}{\langle \rho \rangle} \frac{dn(r, r+dr)}{da(r, r+dr)}$$

where  $\langle \rho \rangle$  is the average particle number density and  $r$  is the particle radius. Figure 2-2D shows that the positions of the oscillating PCF peaks agree well with those obtained from a perfect hexagonal close-packed lattice.

DBC technology can be utilized to align uniform silica microspheres with diameters ranging from ~200 to ~700 nm, which can be easily synthesized by the Stober method.<sup>185,187</sup> Figure 2-2E shows a top-view SEM image of a composite consisting of 330 nm silica microspheres. The protrusion depth of 330 nm microspheres from the polymer matrix is apparently shallower than that of 290 nm spheres. This leads to the non-close-packed appearance of the microspheres as shown in Figure 2-2E. Indeed, extensive PCF calculations reveal that the doctor blade coated colloidal crystals are close-packed. To evaluate the minimal particle size that still allows the formation of highly ordered composites using DBC, we tested 70 nm silica spheres synthesized by microemulsion technology.<sup>188-189</sup> However, only disordered arrays resulted. As demonstrated in our previous spin-coating technology, a nearly 1 order of magnitude higher shear rate is required to align 70 nm silica spheres compared to that required to align 300 nm particles.<sup>186</sup> Besides ETPTA, a large variety of nonvolatile monomers and monomer mixtures can also be used to form highly ordered colloidal crystal-polymer composites by DBC, provided the concentrated silica-monomer suspensions are stable. Figure 2-2F shows a top-view SEM image of a composite consisting of 290 nm silica spheres and a hydrophilic poly(ethylene glycol) (600) diacrylate (PEGDA, SR 610, Sartomer) matrix. The long-range ordering of the silica microspheres is similar to that of colloidal crystals prepared in other polymer matrixes.

Crystalline thickness is another important parameter in determining the quality and application of self-assembled crystals. We therefore conducted systematic investigations on the effect of coating speed, particle size, and particle volume fraction on the resulting composite thickness. The results are summarized in Figure 2-3 for silica

microspheres of 290, 330, and 560 nm diameter. To obtain the average thickness and standard deviation, at least 3 samples were prepared under each condition and the crystal thicknesses at more than 10 random locations on each sample were measured by cross-sectional SEM. The crystalline quality of the sample was also monitored by SEM, and the data points in Figure 2-3 indicated only the conditions under which highly ordered composites were obtained. By analyzing the results in Figure 2-3, we found that (1) the composite becomes thicker when the coating speed increases; (2) the more dilute colloidal suspensions lead to thicker composites when the particle size and the coating speed remain the same; (3) larger particles lead to thicker samples when the particle volume fraction and the coating speed are the same; and (4) the operating window for obtaining highly ordered composites is narrower for the more dilute colloidal suspensions.

The above observations can be qualitatively explained by adapting the mechanisms developed for traditional DBC.<sup>177-180</sup> In traditional DBC, both pressure-driven flow and shear-driven flow play a crucial role in determining the properties of the resulting coatings. Pressure-driven flow is caused by the pressure exerted by the colloidal suspension head,  $\Delta P = \rho_{suspension} g \Delta h$ , where  $\Delta h$  is the height difference between the suspension reservoir and the doctor blade coated film (Figure 2-4).<sup>180</sup> A higher pressure head leads to a greater flow rate across the blade. Shear-driven flow is attributed to the movement of the substrate, and the corresponding shear stress  $\tau$  can be evaluated by using Newton's law of viscosity (for Newtonian fluids)

$$\tau = -\mu \frac{dv_x}{dy}$$

where  $\mu$  is the viscosity of colloidal suspension and  $v_x$  is the substrate velocity along the  $x$  direction.<sup>190</sup> As demonstrated in our previous work, the concentrated silica-ETPTA suspension is Newtonian over four decades of shear rate.<sup>186</sup> In a Newtonian fluid, the flow rates originating from the pressure head and the shear drag force are additive.

We attribute the observed colloidal crystallization in the above DBC procedures to shear-induced ordering.<sup>191</sup> Highly ordered colloidal arrays form when the shear rate is sufficiently high. To evaluate the critical shear rate needed to align colloidal particles, we measured the relative viscosity (normalized by the viscosity of the monomer,  $\sim 60$  cps for ETPTA) of silica-monomer suspensions with different particle volume fractions at various shear rates (Figure 2-5). The obvious shear-thinning behavior is caused by the shear-induced crystallization of colloidal particles and the reduced resistance when layers of ordered spheres glide over one another.<sup>191-192</sup> From Figure 2-5, it is apparent that a critical shear rate of  $\sim 10 \text{ s}^{-1}$  is needed to achieve the relative viscosity plateau. In our DBC procedures, the shear rate caused by the substrate drag alone is only  $\sim 0.1 \text{ s}^{-1}$  by using a typical substrate velocity ( $\sim 1 \text{ }\mu\text{m/s}$ ) and film thickness ( $\sim 10 \text{ }\mu\text{m}$ ). Therefore, we deduce that the pressure-driven flow plays a more important role in determining the properties of the resulting films.

In our DBC setup (Figure 2-4), the pressure head drives the flow of the colloidal suspensions across the small gap ( $<1\text{ }\mu\text{m}$ ) between the blade and the substrate. The resulting film thickness is determined by this pressure and the suspension viscosity. A higher pressure and a lower viscosity lead to thicker films. From extensive experiments, we found that the suspension reservoir height was controlled by the coating speed: a

faster substrate velocity led to a more rapid accumulation of colloidal suspensions. This results in a higher pressure head and thus a thicker film, agreeing with observation 1 above. For a given particle size and coating speed, our experimental results in Figure 5 show that the viscosities of the relatively dilute suspensions (35 and 20 vol %) are less than that of the 50 vol % suspension. Therefore, it is not surprising to observe the formation of thicker films for the more dilute colloidal suspensions (observation 2). Observation 3 above is also related to the viscosity of colloidal suspensions. Our previous results show that suspensions consisting of large silica particles exhibit a lower viscosity than do suspensions of smaller particles with the same particle volume fraction.<sup>186</sup> To explain observation 4, both suspension viscosity and shear rate effects need to be considered. From Newton's law of viscosity, the shear stress is proportional to the suspension viscosity and the shear rate. For a more dilute suspension, the lower suspension viscosity and the thicker final films (i.e., a smaller shear rate) contribute synergistically to a smaller shear stress. Thus, it is reasonable to observe the narrower operating window for obtaining highly ordered composites for the more dilute suspensions. A detailed rheological study and an analytical fluid flow model are being developed and the results will be reported in our future publications.

The polymer matrix of the shear-aligned composites can be selectively removed by oxygen plasma etching to release the embedded silica colloidal crystals. Figure 2-6 shows a cross-sectional SEM image of a colloidal crystal prepared by etching a composite sample at 40 mTorr oxygen pressure, a 40 sccm flow rate, and 100W for 10min. The long-range hexagonal ordering of the original composite is mostly retained in the final silica colloidal crystal, though some structural collapse during the polymer

removal process is also noticed. This collapse makes the determination of the crystalline ordering and structure perpendicular to the substrate surface difficult. We therefore selectively etched out silica particles in the composites by a brief hydrofluoric acid (2 vol %) wash to create macroporous polymers. The structure does not collapse during the etching process, and the resulting film is easy to break to reveal the cross-section of the crystal. Figure 2-7A shows a photograph of a free-standing macroporous ETPTA membrane templated from 290 nm silica spheres. The film exhibits a striking green color caused by the Bragg diffraction of visible light from the crystalline lattice of air cavities in the polymer. The typical SEM image of the top surface of a macroporous film and the Fourier transform of a lower magnification image as shown in Figure 2-7B reveals that the long-range hexagonal ordering of the shear-aligned composite is well retained during the wet-etching process. A magnified SEM image in Figure 2-7C also shows that the large voids templated from silica microspheres are interconnected through smaller pores that originate from the touching sites of silica particles in the composites.<sup>193</sup> Extensive SEM characterizations confirm that the bottom side of the macroporous film has the same structure as the top surface. The crystalline ordering perpendicular to the (111) plane is clearly seen from the cross-sectional SEM image in Figure 2-7D. However, a detailed SEM analysis shows that no relationship between neighboring layers (e.g., ABCABC for a face-centered cubic crystal or ABABAB for a hexagonal close-packed crystal) can be obtained. This suggests that the hexagonal close-packed layers are randomly stacked. Indeed, random stacking has been commonly observed in self-assembled colloidal crystals prepared by gravitational sedimentation and shear alignment.<sup>194</sup>

To evaluate the optical properties and the crystalline structure of the doctor blade coated crystals further, we measured the optical reflection at normal incidence using an Ocean Optics<sup>®</sup> visible-near-IR spectrometer with a reflection probe. Figure 2-8A shows the reflection spectra obtained from a composite consisting of 290 nm silica spheres and an ETPTA matrix and the corresponding silica colloidal crystal and macroporous ETPTA film. The samples are prepared by DBC at a speed of 0.1  $\mu\text{m/s}$ , and the film thickness is measured to be 12 monolayers by SEM. All three spectra show distinct peaks caused by the Bragg diffraction of visible and near-IR light from the three-dimensional ordered structures. The low refractive index contrast of the composite and the partially collapsed structure of the silica colloidal crystal lead to the low reflection amplitudes of the corresponding spectra. The position of the diffraction peak can be correlated to the sphere size and the effective refractive index of the medium ( $n_{\text{eff}}$ ) using Bragg's law:  $\lambda_{\text{peak}} = 2n_{\text{eff}}d \sin \theta$ , where  $d$  is the interlayer spacing and  $\sin \theta = 1$  at normal incidence. The effective refractive index of the medium is calculated using  $n_{\text{eff}} = n_1 f_1 + n_2 f_2$ , where  $n_1$  and  $n_2$  are the refractive indices of the components and  $f_1$  and  $f_2$  are their corresponding volume fractions. Figure 2-8A shows that the predicted peak positions as indicated by the arrows agree well with the experimental results. We have also conducted a more rigorous full-spectrum calculation using a scalar wave approximation (SWA) model.<sup>195</sup> The calculated reflection spectrum from a macroporous ETPTA membrane with close-packed 290 nm voids and 12 monolayers is compared with the experimental spectrum in Figure 2-8B. The remarkable agreement between theory and experiment further confirms the highly crystalline quality of the shear-aligned crystals and the faithful replication of the original composite during HF treatment.

We have demonstrated above that the single-blade coating process can be utilized to create high-quality composites, colloidal crystals, and self-standing macroporous polymer membranes. Limited by the size of the commonly used doctor blades and the simple experimental setup, we have fabricated only centimeter-sized samples as proof-of-concept examples in this work. Similar DBC procedures using larger blades (up to a few meters long) and commercial doctor blade coaters have been widely employed to create highly uniform coatings over large areas in continuous roll-to-roll processing (similar to printing newspapers). Because stable colloidal silica-monomer suspensions are easily available in large quantities, we believe that much larger colloidal arrays can be mass produced by using mature DBC technology. However, to reach the full potential of the roll-to-roll compatible DBC process in the large-scale fabrication of highly ordered composites, the coating speed that is limited to  $\sim 5 \mu\text{m/s}$  by a single-blade setup (Figure 2-3) needs to be significantly improved. The rapid accumulation of excess colloidal suspensions that leads to a higher pressure and a thicker film reduces the achievable shear rate and the resulting crystalline quality in a fast coating system. To eliminate excess suspensions, we developed a dual-blade setup as shown by the scheme in Figure 2-9A. The first blade removes excess colloidal suspensions and creates a uniform thin film. The second blade, which is composed of three separate sub-blades, then shear aligns the colloidal microspheres underneath them. Figure 2-9B shows a photograph of a sample coated at 1 mm/s by using the dual-blade setup. The sample does not show iridescent colors after passing the first blade, indicating no long-range ordering in the sample. After crossing the second blade, three iridescent stripes underneath the sub-blades are clearly evident whereas no diffractive colors are

observed in between. This indicates that the shear stress provided by the sub-blades is sufficiently high to align the particles at a high coating speed. These striped colloidal arrays could find potential applications in diffractive optical devices and are available by other self-assembly technologies.<sup>196</sup> If we use a normal doctor blade instead of a blade with three sub-blades as the second blade in the dual-blade setup (Figure 2-9A), then the stripe patterns shown in Figure 2-9B can be prevented.

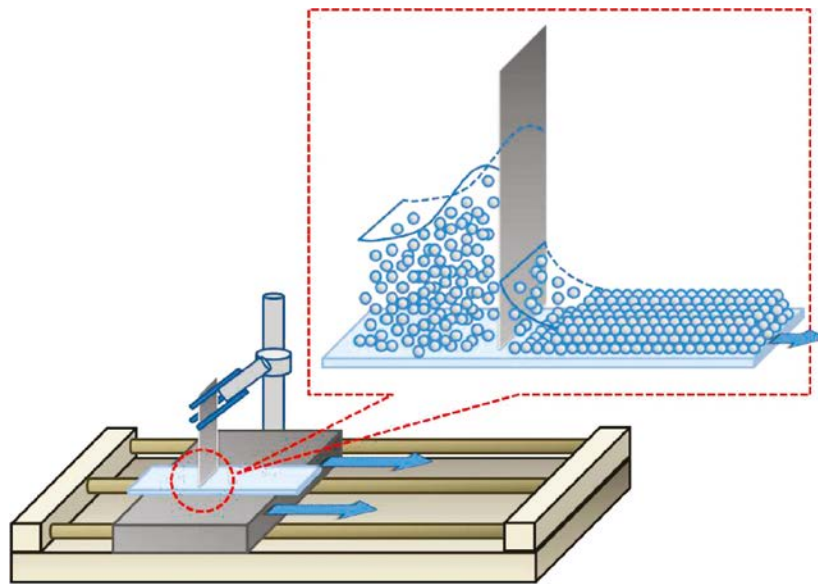


Figure 2-1. Schematic illustration of the experimental setup for assembling large-area colloidal crystal/polymer composites by using a simple doctor blade coating technique.

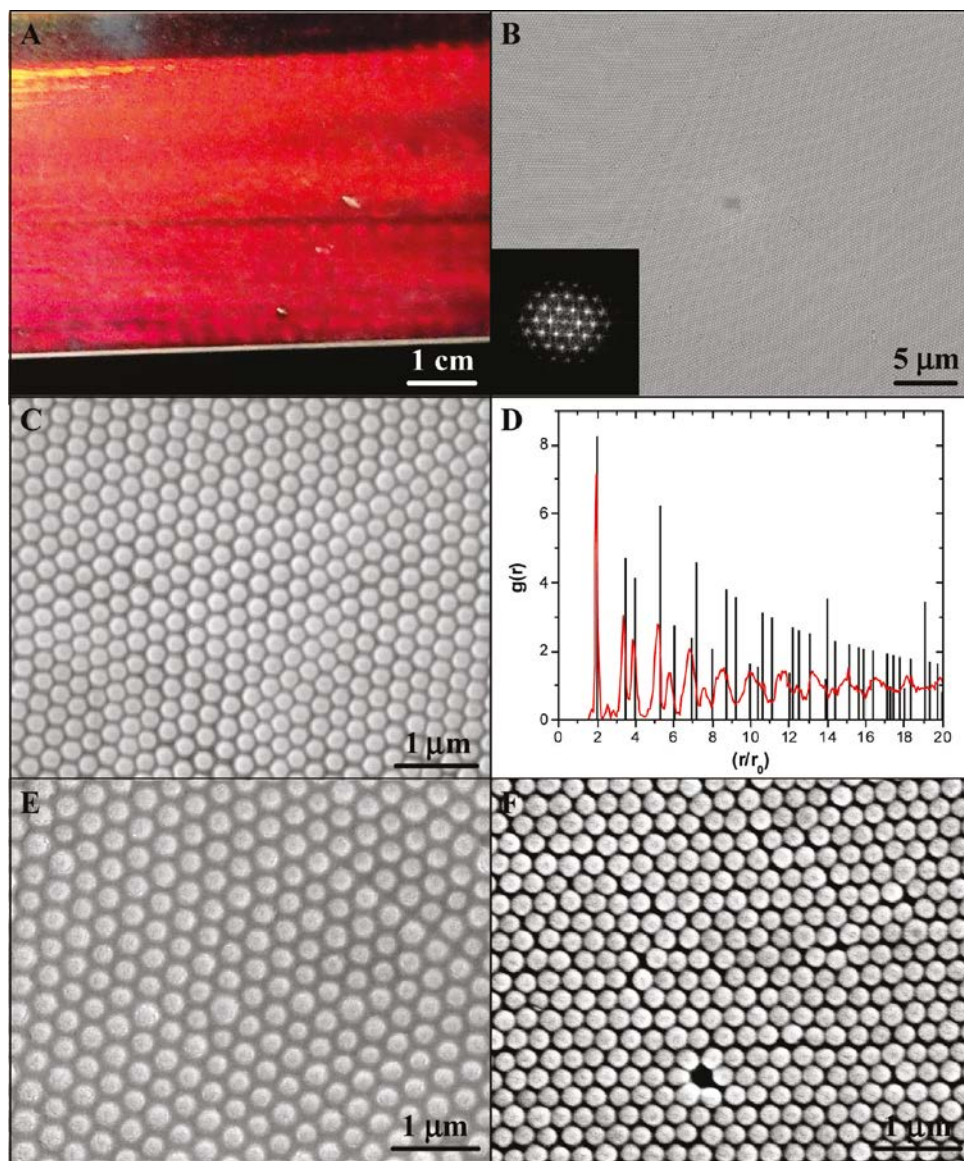


Figure 2-2. Colloidal crystal/polymer composites fabricated by the doctor blade coating technique. A) Photograph of a multilayer composite consisting of 290 nm silica spheres embedded in an ETPTA matrix coated onto a glass substrate. B) Top-view SEM image of the sample in A. Inset showing a Fourier transform of a  $40\ \mu\text{m} \times 40\ \mu\text{m}$  region. C) Magnified SEM image of B. D) Pair correlation function (PCF) calculated from the SEM image in B. For comparison, the PCF for an ideal lattice with hexagonal close-packed structure is also shown (black lines). E) Top-view SEM image of a sample consisting of 330 nm silica spheres embedded in an ETPTA matrix. F) Top-view SEM image of a composite consisting of 290 nm silica spheres embedded in a PEGDA matrix. All samples are prepared by doctor blade coating 50 vol % colloidal suspensions at a speed of  $0.1\ \mu\text{m/s}$ .

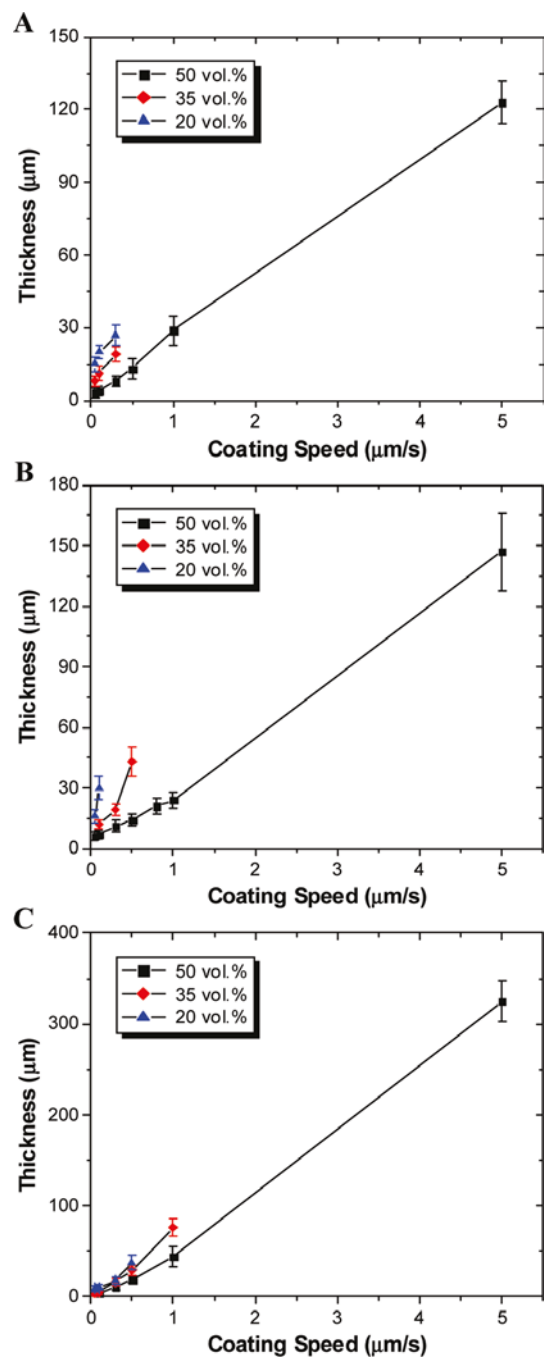


Figure 2-3. Thickness dependence of the doctor blade coated colloidal crystal/ETPTA composites on the coating speed and particle volume fraction for A) 290, B) 330, and C) 560 nm silica spheres.

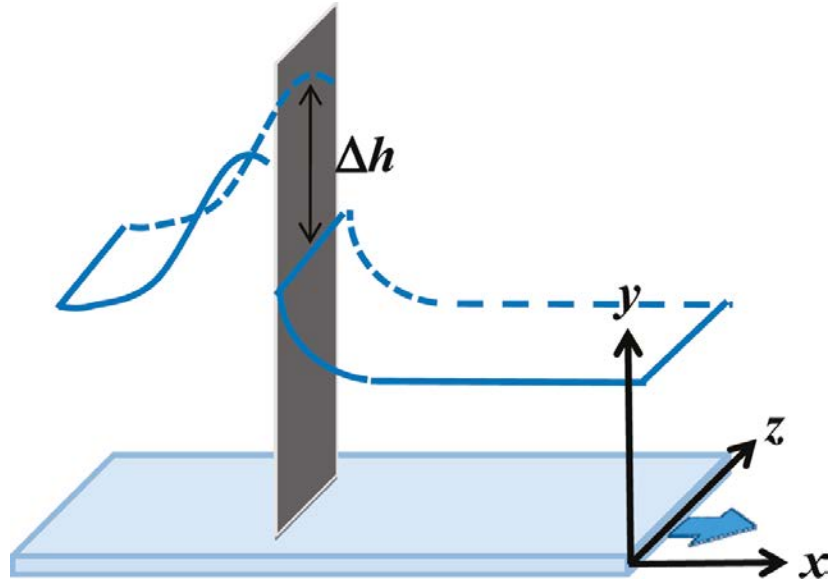


Figure 2-4. Schematic illustration of the velocity profile and the pressure head ( $\Delta h$ ) in the doctor blade coating process.

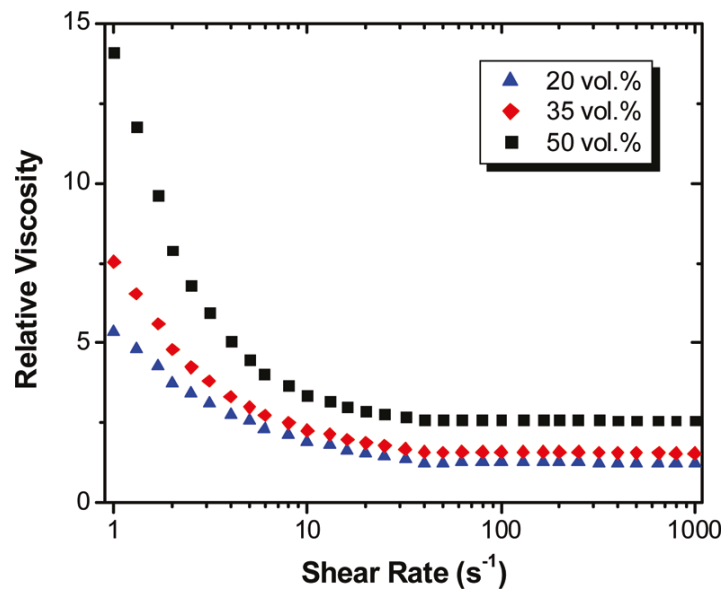


Figure 2-5. Relative viscosity of 330 nm silica spheres/ETPTA suspensions with different particle volume fractions at various shear rates.

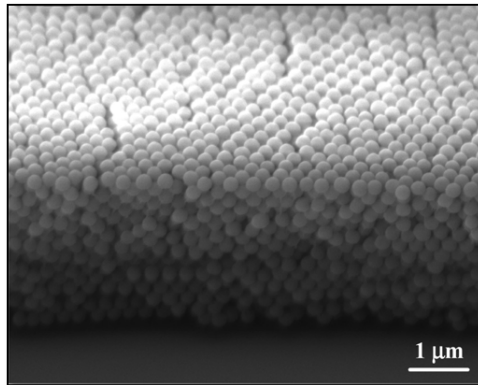


Figure 2-6. Cross-sectional SEM image of a silica colloidal crystal after removing the ETPTA matrix by 10 min of oxygen plasma etching.

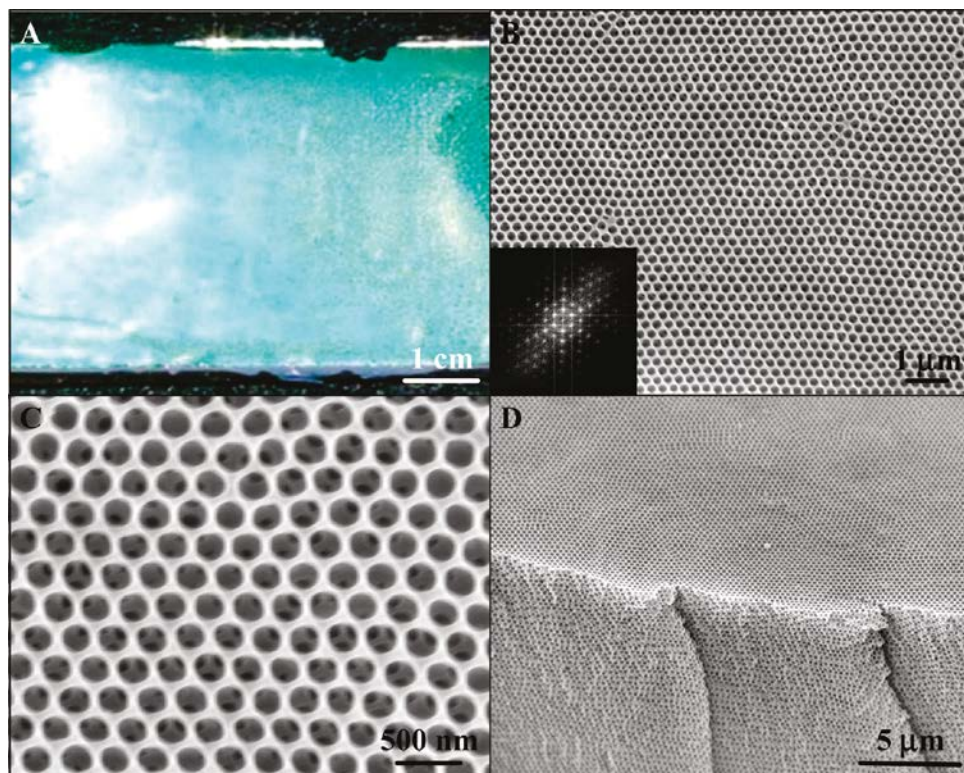


Figure 2-7. Macroporous polymer membrane after the selective removal of templating silica spheres. A) Photograph of a free-standing, macroporous ETPTA film templated from 290 nm silica spheres. B) Top-view SEM image of the sample in A). C) Magnified SEM image of B). D) Cross-sectional SEM image of the sample in A). The sample was coated at a speed of 5  $\mu\text{m/s}$ .

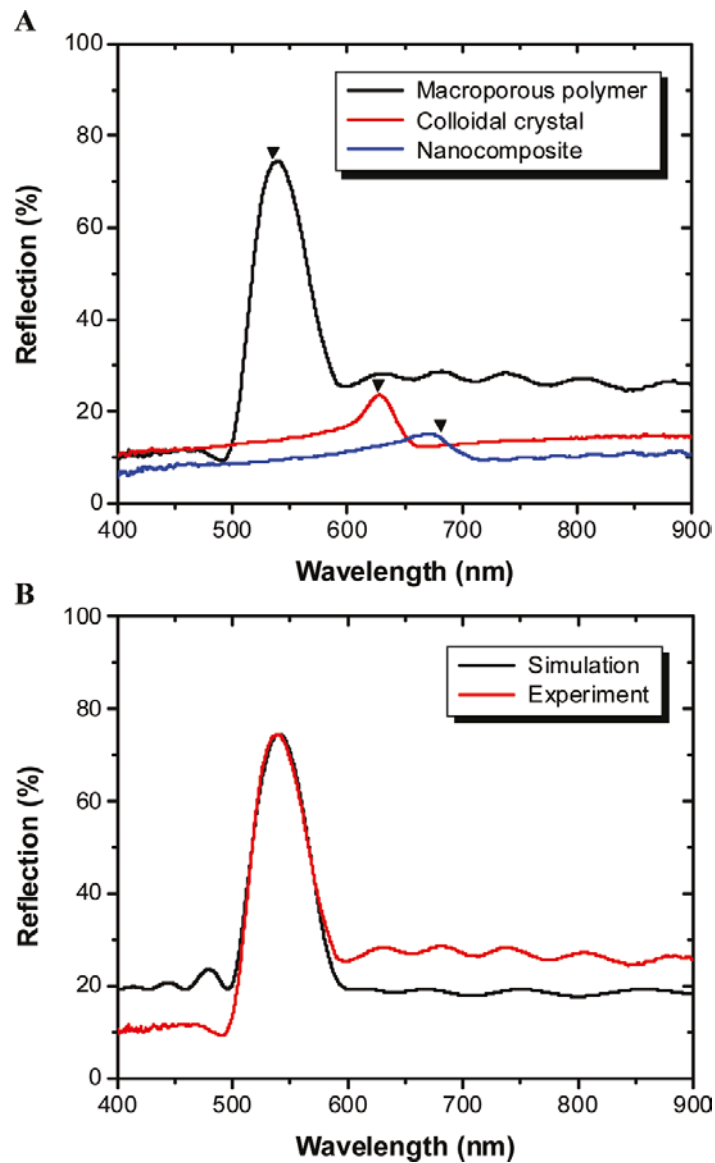


Figure 2-8. A) Normal incidence optical reflection spectra of an ETPTA/silica colloidal crystal composite, a corresponding macroporous ETPTA film, and a released silica colloidal crystal with 290 nm spheres and 12 colloidal layers. The arrows indicate the expected positions of the peaks for each sample, calculated using Bragg's law at normal incidence. B) Comparison of the experimental and SWA-simulated optical reflection spectra at normal incidence from a macroporous ETPTA film template from 290 nm silica spheres.

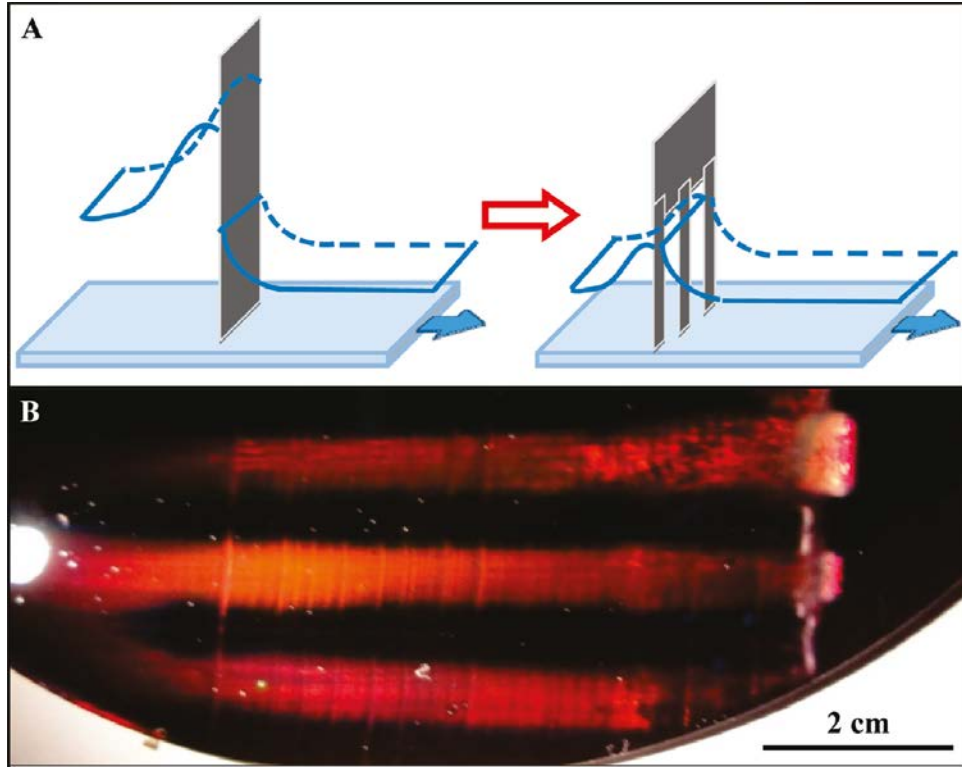


Figure 2-9. A) Schematic illustration of the dual-blade setup. B) Photograph of a multilayer composite consisting of 290 nm silica spheres embedded in an ETPTA matrix aligned by a dual-blade system at a coating speed of 1 mm/s.

## CHAPTER 3 HEAT PIPE-INSPIRED COLOR REFLECTIVE DISPLAYS

There is a big market for the low-end color displays, such as those widely used in supermarkets, signs, roadside advertisement etc. The companies like Wal-Mart Stores, Inc. and Hewlett-Packard Company express interests in low-cost color displays. These displays are not competing with high-end products, such as flat-panel displays. They do not need very fast response time and the resolution requirement is also relatively low. However, they need to be fabricated in very large area (meters-scale) and in a low cost.

Some approaches have been explored to developed next-generation low-end color displays. Organic light-emitting diodes (OLEDs) based displays have been proposed for low-end products. However, the cost and manufacturing process are still expensive. Hewlett-Packard Company is developing novel reflective color displays based on colorful metal nanoparticles using the so-called surface-plasmon effect. Unfortunately, the low-cost fabrication over large areas is questionable.

Therefore, a new methodology in creating reflective color displays by using macroporous polymers which can be created by a simple, inexpensive, and roll-to-roll compatible fabrication technology is highly desired. A methodology is inspired by the heat pipe technology which has been extensively used in dissipating heat for computer chips, solar cells, space shuttles, and Tran-Alaska Pipeline System. A heat pipe is a heat transfer mechanism that combines the principles of both thermal conductivity and phase transition to efficiently manage the transfer of heat between two solid interfaces. At the hot interface within a heat pipe, a liquid in contact with a thermally conductive solid surface turns into a vapor by absorbing the heat of that surface. The vapor condenses back into a liquid at the cold interface, releasing the latent heat. The liquid

then returns to the hot interface through either capillary action or gravity action where it evaporates once more and repeats the cycle.

### 3.1 Experimental Procedure

An immobilized 90°-beveled razor blade (Fisher<sup>®</sup>, 4 cm wide) is gently placed on a substrate. One milliliter of silica/ETPTA suspension is dispensed along one sidewall of the blade onto the substrate. The substrate is dragged by a syringe pump at 1 μm/s. After DBC, the sample is transferred to a pulsed UV curing system and ETPTA monomer is rapidly polymerized by exposure to UV radiation for 4 seconds. To prepare macroporous polymers, the silica/ETPTA composites are immersed in a 2 vol % hydrofluoric acid aqueous solution for 30 min, then rinsed with DI water, and finally dried in a stream of nitrogen.

As shown in Figure 3-1, ethanol is added to a PDMS cell, and the prepared macroporous polymer film is placed on top of the cell. The whole cell is then placed on a hot plate, followed by connecting the ITO-coated glass part to a potentiostat. Optical properties of the macroporous polymers are evaluated by measuring their reflection spectra at normal incidence, using a Cary 5 UV-VIS-NIR spectrometer.

An Ocean Optics<sup>®</sup> spectrometer with a reflection probe is used for reflectance measurements. A calibrated halogen light source is used to illuminate the sample. The beam spot size is about 3mm on the sample surface. Measurements are performed at normal incidence, and the cone angle of collection is less than 5°. Absolute reflectivity is obtained as a ratio of the sample spectrum to the reference spectrum. The reference spectrum is the optical density obtained from an aluminum-sputtered (1000 nm thick) silicon wafer. The final value of the absolute reflectivity is the average of several measurements obtained from different spots on the sample surface.

### 3.2 Results and Discussion

The self-standing macroporous polymer films exhibit brilliant colors which originate from the Bragg diffraction of visible light from the three-dimensional highly ordered air cavities (Figure 2-7). The colors can be easily changed by tuning the size of the air cavities to cover the whole visible spectrum. This indicates that all-color displays are possible. When the air cavities are filled with a solvent which has the same refractive index as that of the polymer, the macroporous polymer films become completely transparent due to the index matching. Figure 3-2A shows a green-color macroporous polymer sample. When the air cavities are filled with ethanol (refractive index of ethanol is close to that of the polymer), the sample changes color to red and becomes transparent (the letters "UF" underneath the sample is visible) (Figure 3-2B). When ethanol is evaporated by in-situ heating, the sample color changes back to green. This process is highly reversible and reproducible for thousands of cycles. Figure 3-2C and Figure 3-2D show the optical reflection spectra during the color change process. Moreover, proof-of-concept experiments as shown in Figure 3-3A and Figure 3-3B indicate that patterned macroporous polymers could also be applied to fabricate patterned reflective color displays. Figure 3-3C and Figure 3-3D show the optical reflection spectra during the color change process. This color change process is also reproducible for thousands of cycles.

It is demonstrated that two-color displays are feasible by a macroporous polymer film. The macroporous polymer film is with 330 nm sized pores on the top side layer and 280 nm sized pores on the bottom side layer. The two macroporous layers are not connected and with openings on top side and bottom side of the film, respectively. The macroporous polymer film exhibits brilliant orange plus green colors (Figure 3-4A). The

green color originates from the Bragg diffractive of visible light from the highly ordered 280 nm sized air cavities on the bottom layer, and the orange color originates from 330 nm sized air cavities on the top layer. When the air cavities on the bottom side of the film are filled with ethanol, the bottom layer becomes transparent due to the refractive index matching, leading to the sample changes color to orange (Figure 3-4B). Similarly, when the air cavities on the top side of the film are filled with ethanol, the top layer becomes transparent and the sample changes color to green (Figure 3-5B). When ethanol is evaporated by in-situ heating, the sample color changes back to orange plus green (Figure 3-5A). This process is reproducible. Optical reflection spectra show the color change processes when the top side cavities or bottom side cavities of macroporous polymer are gradually replaced by ethanol or air (Figure 3-4C, Figure 3-4D, Figure 3-5C, Figure 3-5D).

We can also fabricate multi-color displays by creating macroporous polymer films with stacked air cavities with different sizes that reflect different colors (e.g., red, green, blue as shown in Figure 3-6). We have demonstrated that DBC can be used to create large-area multi-color macroporous polymer films by consecutive coatings of particles of different sizes.

To achieve in-situ heating and cooling for making real devices, we construct a protocol as shown in Figure 3-7 and Figure 3-8 by using indium tin oxide (ITO) coated glass as heating element. Applying a low voltage (1-2 V) for several seconds is sufficient to achieve  $\sim 70^{\circ}\text{C}$  to evaporate ethanol which is filled in the top macroporous polymer. A thin polydimethylsiloxane (PDMS) space is used in between the top macroporous polymer and the glass substrate. When power is on, ethanol filled in the

cavities of macroporous polymer is rapidly evaporated. The macroporous polymer becomes highly shining. When the voltage is turned off, the air cavities in macroporous polymer are then replaced with ethanol and sample becomes transparent.

In addition, full-color reflective displays are feasible by introducing solvent with higher refractive index. In the proof-of-concept experiment, different solvents with different refractive indices (e.g.,  $RI_{\text{water}} = 1.33$ ,  $RI_{\text{isopropanol}} = 1.40$ ,  $RI_{\text{toluene}} = 1.50$ ) are applied to replace ethanol ( $RI_{\text{ethanol}} = 1.36$ ). When the air cavities of macroporous film (Figure 3-9A) are filled with a solvent which is with higher refractive index, the diffractive medium is with a higher effective refractive index, leading to the Bragg diffraction peak shifts to longer wavelength. As shown in Figure 3-9B, the Bragg diffraction peak locates at 620 nm when toluene is applied as a solvent in the system. Comparing with the Bragg diffraction peak when the cavities are filled with ethanol (560 nm), the peak red-shifts for 60 nm, which indicates reflective color displays could also be fabricated by introducing a solvent with high refractive index.

Besides flat displays, proof-of-concept experiment as shown in Figure 3-10 indicates that reflective color displays could also be fabricated on curved surface. Figure 3-10A shows a green-color macroporous polymer sample on curved surface. When the air cavities are filled with ethanol, the sample changes color to red and becomes transparent (Figure 3-10B). This will be of interest for many commercial applications.

In summary, we have invented an inexpensive yet scalable nanomanufacturing technology for producing large-area reflective color displays that target low-end display market. The cost of the reflective color displays is much cheaper than any existing color displays. Besides display application, the macroporous polymer membranes could also

be used as ultra-thin heat pipes for efficient heat management that are of interest in many important technological areas, such as high-speed computing, space shuttles and pipe-lines.

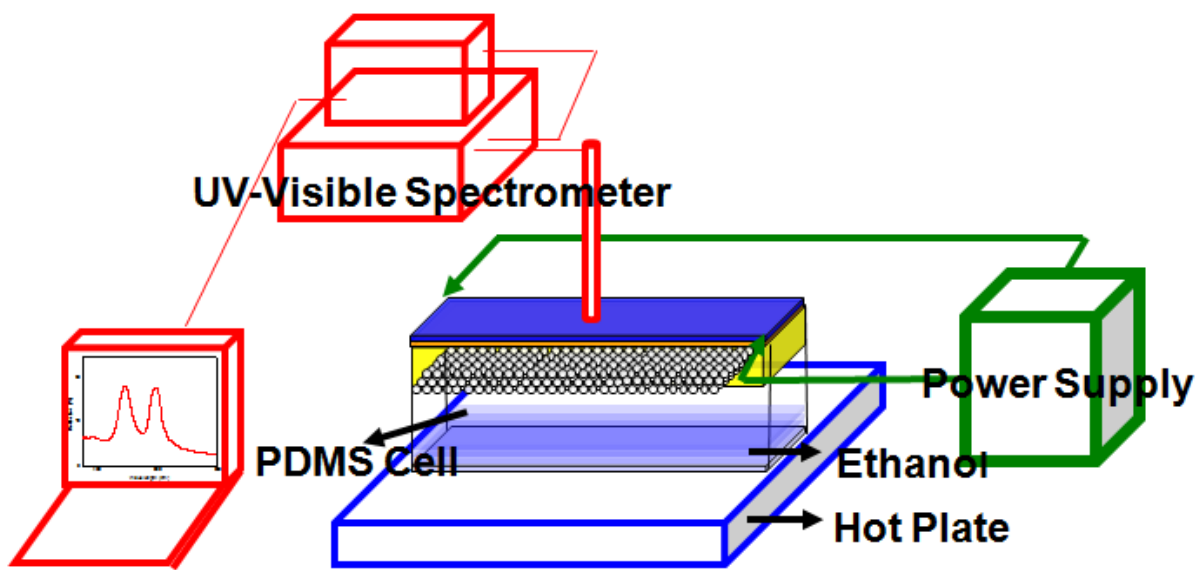


Figure 3-1. Schematic illustration of the experimental setup for heat pipe-inspired color reflective displays.

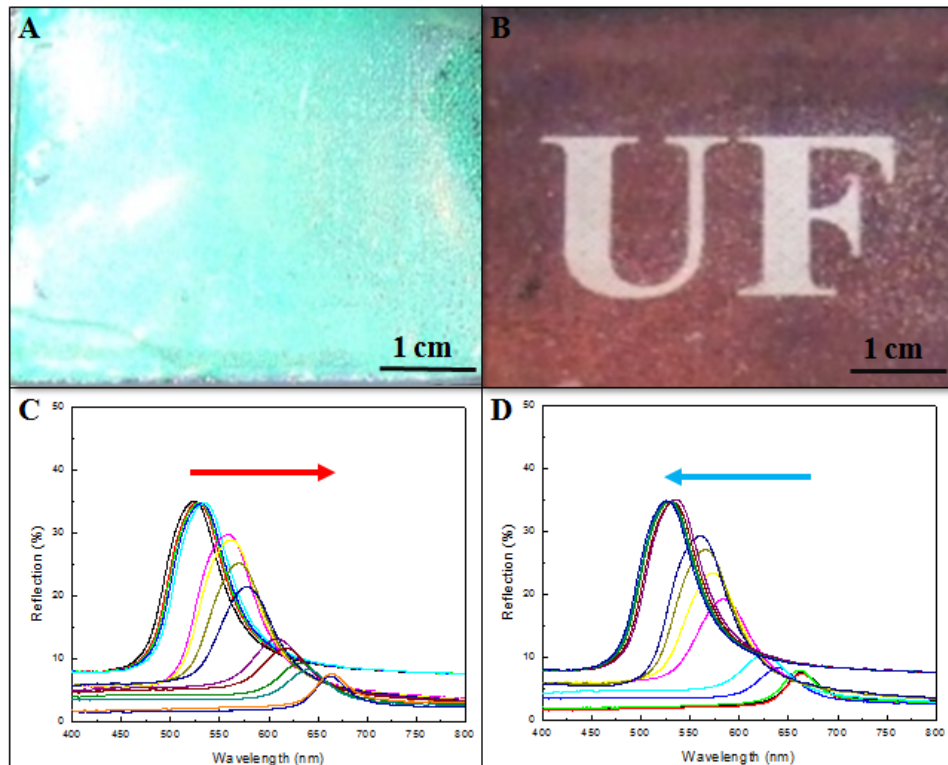


Figure 3-2. Working principle of macroporous polymer reflective color displays. A) A macroporous polymer film exhibits shining green color. B) When the air cavities of macroporous polymer are filled with ethanol. C) Optical reflection spectra showing the color change process when the cavities of macroporous polymer are gradually replaced by ethanol. D) Optical reflection spectra showing the color change process when the cavities of macroporous polymer are gradually replaced by air. The arrows indicate the peak shift direction in the process.

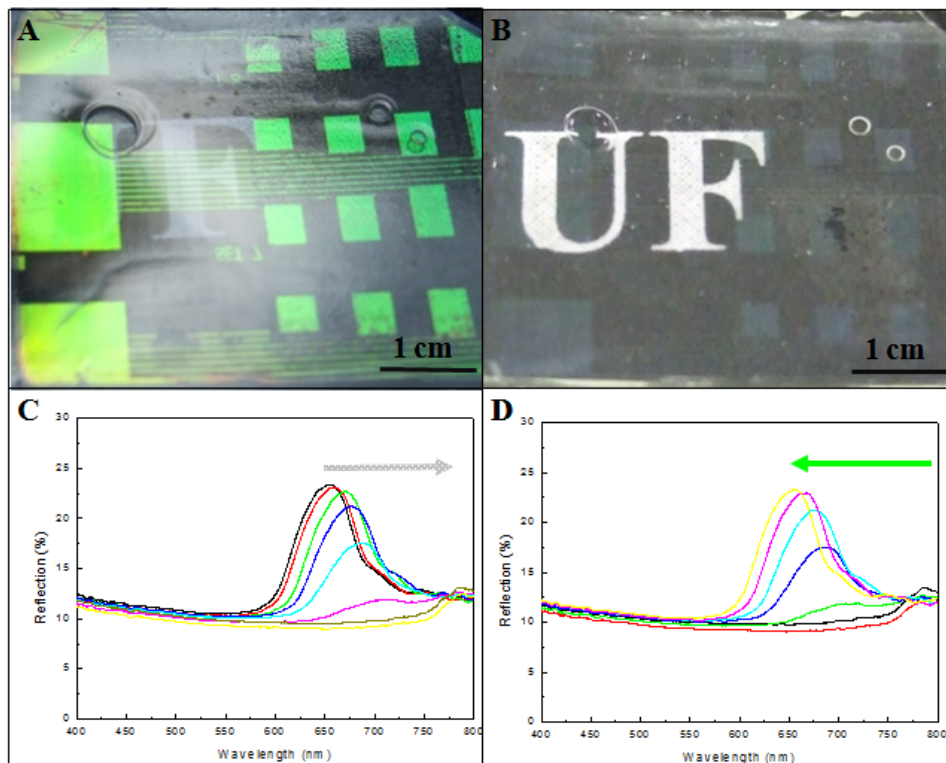


Figure 3-3. Patterned macroporous polymer reflective color displays. A) A patterned macroporous polymer film exhibits shining green color. B) When the air cavities of patterned macroporous polymer are filled with ethanol. C) Optical reflection spectra showing the color change process when the cavities of macroporous polymer are gradually replaced by ethanol. D) Optical reflection spectra showing the color change process when the cavities of macroporous polymer are gradually replaced by air. The arrows indicate the peak shift direction in the process.

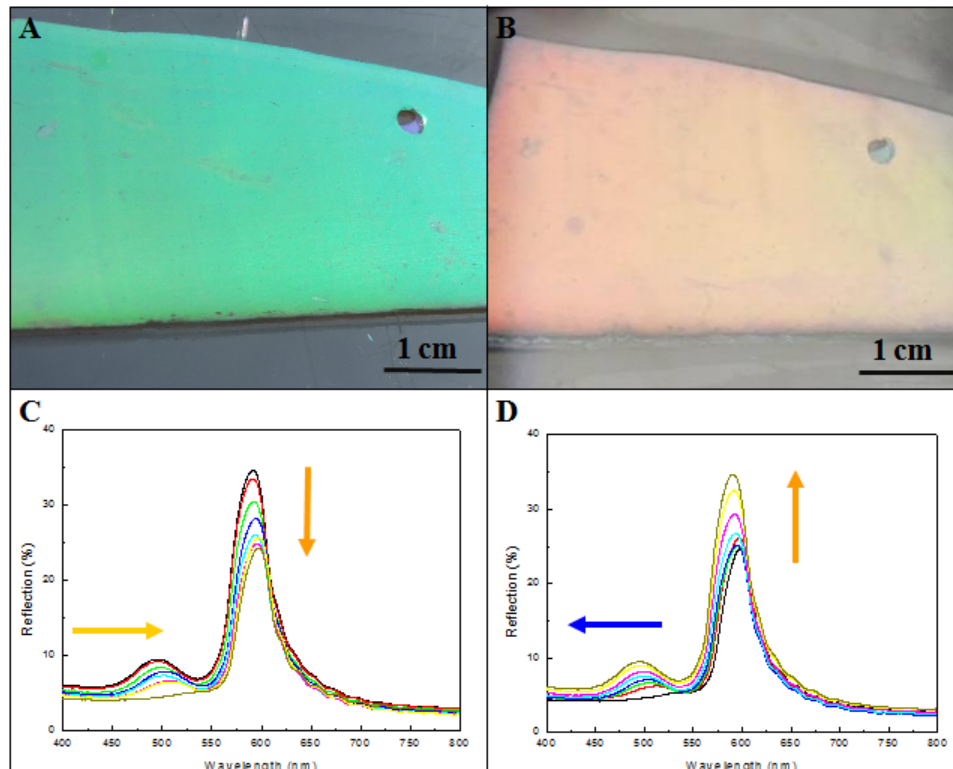


Figure 3-4. Two-color displays are feasible by a macroporous polymer membrane. The macroporous polymer membrane is with 330 nm sized pores on the top side layer and 280 nm sized pores on the bottom side layer. The two macroporous layers are not connected and with openings on top side and bottom side of the membrane, respectively. A) Photograph of a free-standing, macroporous ETPTA film. B) Photograph of the macroporous ETPTA film. The bottom side cavities are filled with ethanol. C) Optical reflection spectra showing the color change process when the cavities of macroporous polymer are gradually replaced by ethanol. D) Optical reflection spectra showing the color change process when the cavities of macroporous polymer are gradually replaced by air. The arrows indicate the peak shift direction in the process.

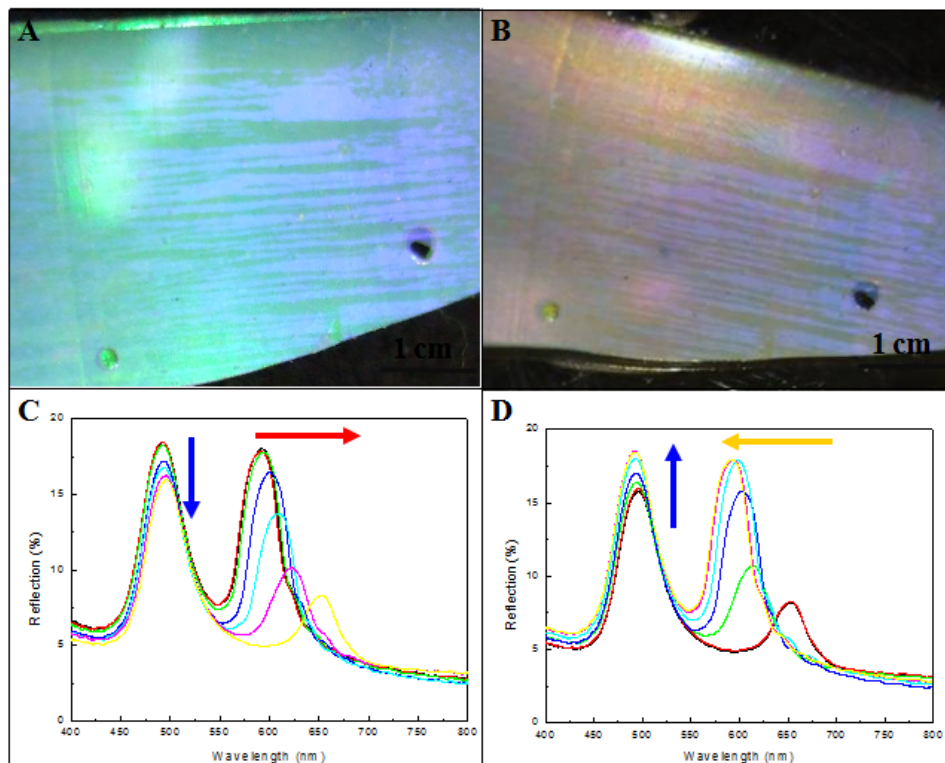


Figure 3-5. Two-color displays are feasible by a macroporous polymer membrane. The macroporous polymer membrane is with 280 nm sized pores on the top side layer and 330 nm sized pores on the bottom side layer. The two macroporous layers are not connected and with openings on top side and bottom side of the membrane, respectively. A) Photograph of a free-standing, macroporous ETPTA film. B) Photograph of the macroporous ETPTA film. The bottom side cavities are filled with ethanol. C) Optical reflection spectra showing the color change process when the cavities of macroporous polymer are gradually replaced by ethanol. D) Optical reflection spectra showing the color change process when the cavities of macroporous polymer are gradually replaced by air. The arrows indicate the peak shift direction in the process.

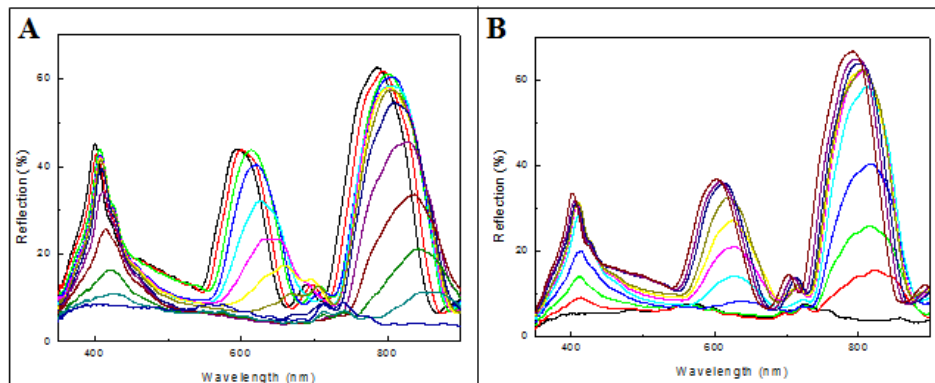


Figure 3-6. Multi-color displays are feasible by fabricating macroporous polymer films with stacked air cavities of different sizes. Macroporous polymer films are with 180 nm sized pores, 300 nm sized pores, and 400 nm sized pores from bottom to top. The three macroporous layers are connected and with opening on bottom side. Optical reflection spectra showing the color change process when the cavities of macroporous polymer are gradually replaced by A) ethanol and B) air. The arrows indicate the peak shift direction in the process.

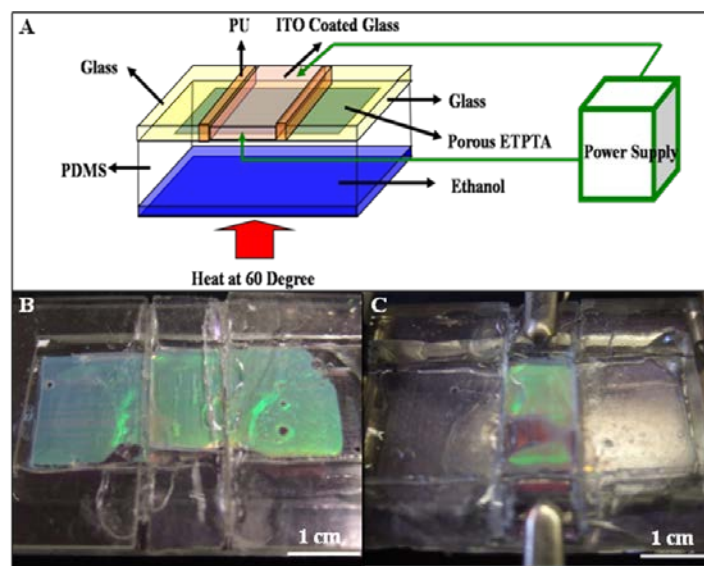


Figure 3-7. Protocol of an electrically driven reflective color display. The macroporous polymer is with 280 nm sized pores. A) Schematic illustration of the experimental setup. B) Photograph of display part setup. The whole setup is kept at 25 °C. C) Photograph of display part setup. Ethanol in the PDMS cell is kept at 60 °C, and the specific part of ITO-coated glass is heated until 70 °C by a potentiostat.

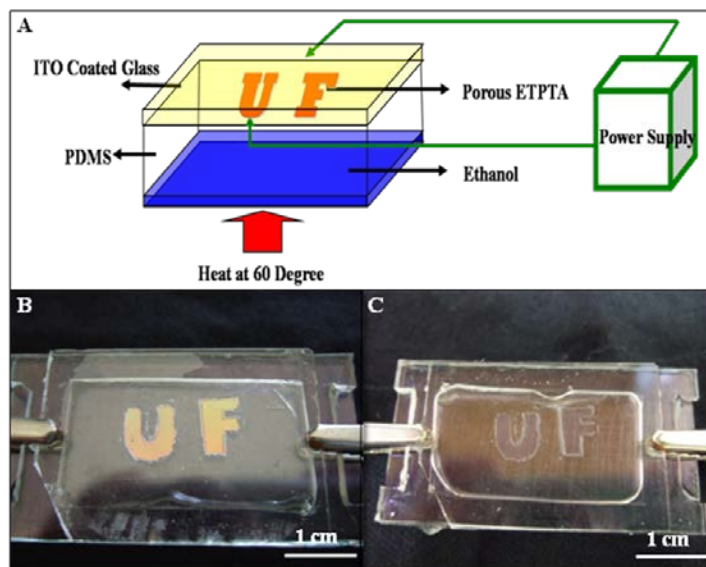


Figure 3-8. Protocol of an electrically driven reflective color display. The patterned macroporous polymer is with 330 nm sized pores. A) Schematic illustration of the experimental setup. B) Photograph of display part setup. Ethanol in the PDMS cell is kept at 60 °C, and the ITO-coated glass is heated until 70 °C by a potentiostat. C) Photograph of display part setup. Ethanol in the PDMS cell is kept at 60 °C, and the ITO-coated glass is cooled down to 55 °C.

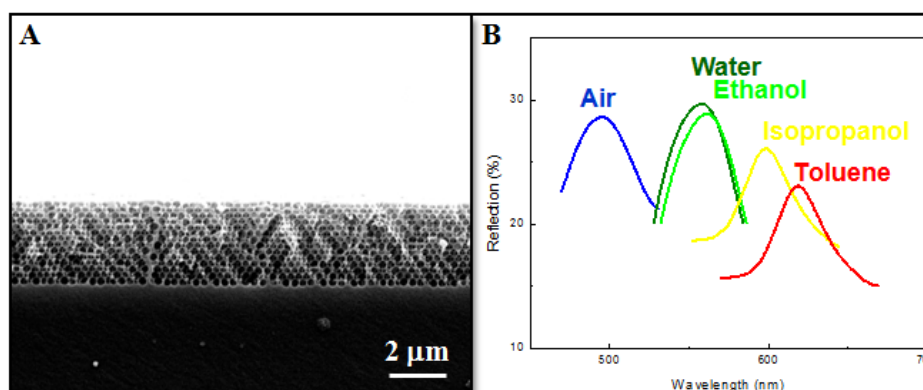


Figure 3-9. Full-color reflective displays are feasible by introducing solvent with higher refractive index. A) Side-view SEM image of the macroporous polymer membrane after the selective removal of templating 280 nm silica spheres. B) Optical reflection spectra showing the color change process when the bottom side cavities of macroporous polymer are replaced with different solvents.

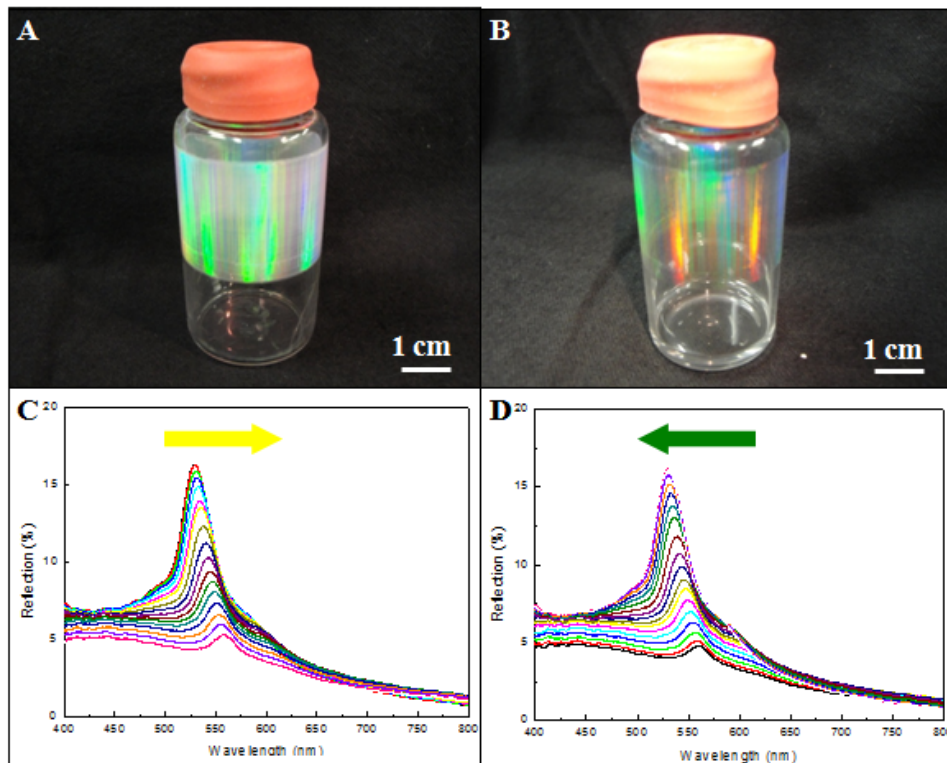


Figure 3-10. Proof-of-concept experiment demonstrates the feasibility of constructing reflective color displays on curve surface. A) Photograph of silica opal on glass vial wall. B) Photograph of ethanol filled silica opal on glass vial wall. C) Normal-incidence optical reflection spectra of curve silica opal in ethanol filling process. The arrow indicates the peak shift direction in the process. D) Normal-incidence optical reflection spectra of curve silica opal in ethanol releasing process.

## CHAPTER 4 MACROPOROUS PHOTONIC CRYSTAL-BASED VAPOR DETECTORS

Tropical Morpho butterflies are famous for their brilliant iridescent colors, which arise from ordered arrays of scales on their wings. The iridescent scales of the Morpho butterfly give a different optical response to different individual vapors, and that this optical response dramatically outperforms that of existing photonic sensors.<sup>61</sup> The reflectance spectra of the scales provide information about the nature and concentration of the vapors, allowing to identify a range of closely related vapors—water, methanol, ethanol and isomers of dichloroethylene when they are analyzed individually.

Although nanotechnology attempts to mimic the partial photonic band-gap structure and the iridescent features of the Morpho butterfly scale in materials with new visual effects and functionality, the exact combination of its three-dimensional structure and cuticle complex refractive index is still beyond nanofabrication capabilities. Nanofabrication has been successful in creating photonic structures for chemical and biological detection. Mechanisms of color generation in existing nanofabricated photonic-sensing materials include localized plasmon resonance, Bragg diffraction, and Fabry–Perot interferometry. An advantage of these photonic structures over organic dyes is the elimination of photobleaching problems. Unfortunately, the main limitations of existing nanofabricated photonic-sensing materials are their high cost, small-scale productivity, and low response selectivity to different analyses. There is only a limited commonality between known biological and engineering solutions to challenging problems, which suggests that the biological world still has a lot to teach us.

## 4.1 Experimental Procedure

Macroporous polymer photonic crystals with three-dimensional crystalline arrays of voids are fabricated by the scalable doctor blade coating (DBC) technology. In this methodology, monodispersed silica microspheres are dispersed in a nonvolatile monomer ethoxylated trimethylolpropane triacrylate (ETPTA), to make colloidal suspensions with particle volume fraction of ca. 50%. An immobilized and vertically beveled razor blade which gently touches with a substrate applies a uniform shear force to align silica microspheres when the substrate is moved at a controlled speed. The monomer is finally photopolymerized to form colloidal crystal-polymer composites. The embedded silica microspheres can then be completely removed by etching in a 2 vol % hydrofluoric acid aqueous solution. After drying, the resulting self-standing macroporous polymer films exhibit uniform and shining colors.

The templated macroporous polymer film is placed in a home-made environmental chamber as shown in Figure 4-1. The chamber is evacuated and then back-filled with a vapor with a specific pressure. Dry nitrogen is used to control the total pressure of the chamber to be 1 atm. An Ocean Optics<sup>®</sup> visible-near-IR spectrometer with a reflection probe is used for specular reflectance measurements. A calibrated halogen light source is used to illuminate the sample. The beam spot size is about 3 mm on the sample surface. Measurements are performed at normal incidence and the cone angle of collection is less than 5°. Absolute reflectivity is obtained as ratio of the sample spectrum and the reference spectrum. The reference spectrum is the optical density obtained from an aluminum-sputtered (1000 nm thickness) silicon wafer. Final value of the absolute reflectivity is the average of several measurements obtained from different spots on the sample surface.

## 4.2 Results and Discussion

Figure 4-2A and Figure 4-2B show typical top-view SEM images of a doctor blade coated composite consisting of 320 nm silica microspheres. The long-range hexagonal ordering of the colloidal crystal is clearly evident. After removing silica particles, the resulting self-standing macroporous polymer films exhibit uniform and shining colors caused by Bragg diffraction of visible light from three-dimensional highly ordered air cavities (Figure 4-2C and Figure 4-2D). Importantly, the large air cavities are interconnected through smaller windows (inset of Figure 4-2C) which are originated from the touching sites of the close-packed silica microspheres in the shear-aligned composite.

Figure 4-3A shows the normal-incidence specular reflectance spectra obtained from a macroporous ETPTA film with 320 nm air cavities exposed to ethanol vapors with different partial pressures (from 0  $P_0$  to 1.0  $P_0$ ) at  $55 \pm 1^\circ\text{C}$ .  $P_0$  is the saturation vapor pressure of ethanol at this temperature (280 mmHg).<sup>197</sup> All spectra display distinct Bragg diffraction peaks with well-defined Fabry-Perot fringes, indicating high crystalline quality of the self-assembled macroporous photonic crystal. When the partial pressure of ethanol vapor is increased, ethanol condensates in the air cavities of the macroporous film, leading to a higher effective refractive index of the diffractive medium and a smaller dielectric contrast between the polymer and the enclosed materials. This explains the observed red-shift of the Bragg diffraction peaks and the reduction of the amplitude of the optical stop bands as shown in Figure 4-3A. Figure 4-3B indicates that the shift of the diffraction peaks (compared to the sample exposed to pure nitrogen gas) is nearly linear with respect to the ethanol partial pressure. The optical properties of the macroporous polymer films are fully recovered when the condensed ethanol is

evaporated. The photonic crystal films can thus be reused many times for reproducible vapor detection.

We further evaluate the speed of response of photonic crystal vapor detectors. Figure 4-4A shows the time dependence of the specular reflectance spectra obtained from a macroporous polymer film exposed to ethanol vapor with a partial pressure of  $0.5 P_0$  at  $55^\circ\text{C}$ . The corresponding spectral peak positions at different exposure times are compared in Figure 4-4B. It is apparent that the equilibrium is reached in less than 1 min. For other operating conditions (i.e., different vapor partial pressures and temperatures), similar speed of response is obtained.

To gain a better understanding of vapor condensation in templated macroporous films, we calculate the amount of condensed ethanol at different vapor partial pressures by using the Bragg diffraction equation:  $\lambda_{max} = 2 \times n_{eff} \times d \times \sin\theta$ , where  $n_{eff}$  is the effective refractive index of the diffractive medium,  $d$  is the inter-plane distance, and  $\theta$  is  $\pi/2$  for normal incidence. By assuming the templated air cavities are close-packed and the volume fraction ( $VF$ ) of air in a dry macroporous polymer film is 0.74, the effective refractive index of the medium can be calculated as:  $n_{eff} = n_{ETPTA} \times 0.26 + n_{air} \times VF_{air} + n_{ethanol} \times (0.74 - VF_{air})$ , where  $n_{ETPTA}$ ,  $n_{air}$ , and  $n_{ethanol}$  are 1.46, 1.0, and 1.36, respectively. The calculated volume fractions of the remaining air ( $VF_{air}$ ) in the macroporous film at different ethanol partial pressures are shown in Figure 4-5A.

If we assume the condensed ethanol forms a uniform thin liquid layer on the walls of the polymer voids, the thickness of this ethanol layer can be calculated by using the volume fraction of the condensed ethanol ( $0.74 - VF_{air}$ ). The results in Figure 4-5A show that a 22.4 nm liquid layer can be formed on the walls of 320 nm voids when the

macroporous film is exposed to a saturated ethanol vapor. The calculated ethanol layer thickness is then incorporated in the scalar wave approximation (SWA) model developed for periodic dielectric structures to quantitatively simulate the specular reflectance spectra at different vapor partial pressures.<sup>198-199</sup> Although the simulated spectra (Figure 4-5B) exhibit higher reflectance than the experimental results (Figure 4-3A), the shape, position, red-shift, and amplitude reduction of the diffractive peaks associated with the condensation of ethanol in the voids of the macroporous photonic crystal agree well with the experiments.

We attribute the condensation of ethanol vapor in the macroporous photonic crystals to capillary condensation. The Kelvin equation,  $\ln P/P_0 = -2 V_l \gamma/rRT$ , where  $P$  and  $P_0$  are actual and saturation vapor pressure,  $\gamma$  is the liquid/vapor surface tension,  $V_l$  is the liquid molar volume,  $r$  is the radius of curvature, can be used to describe the phenomenon of capillary condensation due to the presence of a curved meniscus. In macroporous films, the radius of curvature of the condensed liquid film equals to the radius of the air cavity minus the liquid film thickness. Thus a higher vapor partial pressure leads to a smaller  $r$  (i.e., a thicker liquid layer). In addition, as  $\gamma$ ,  $V_l$ ,  $R$  and  $T$  are all constants at a fixed temperature,  $\ln P/P_0$  is inversely proportional to  $r$ . Figure 4-6 shows that this prediction agrees well with experimental results when the liquid layer is relatively thick. A thinner liquid layer formed at a low vapor partial pressure might not be continuous and this could explain the large deviation of the two data points in Figure 4-6.

The macroporous photonic crystal-based vapor detection can be easily extended to a large variety of vapors, such as toluene and water. Figure 4-7 shows that the

response of water detection is quite familiar with that of ethanol detection. It is noteworthy to mention that a bulk liquid water droplet cannot penetrate into the voids of a template macroporous ETPTA film due to a large water contact angle of  $78 \pm 3^\circ$ .

In summary, we have demonstrated that macroporous photonic crystals created by a continuous and scalable doctor blade coating process can be used directly for vapor detection. The capillary-condensed vapor forms a liquid layer covering the surface of the submicrometer-scale macropores.

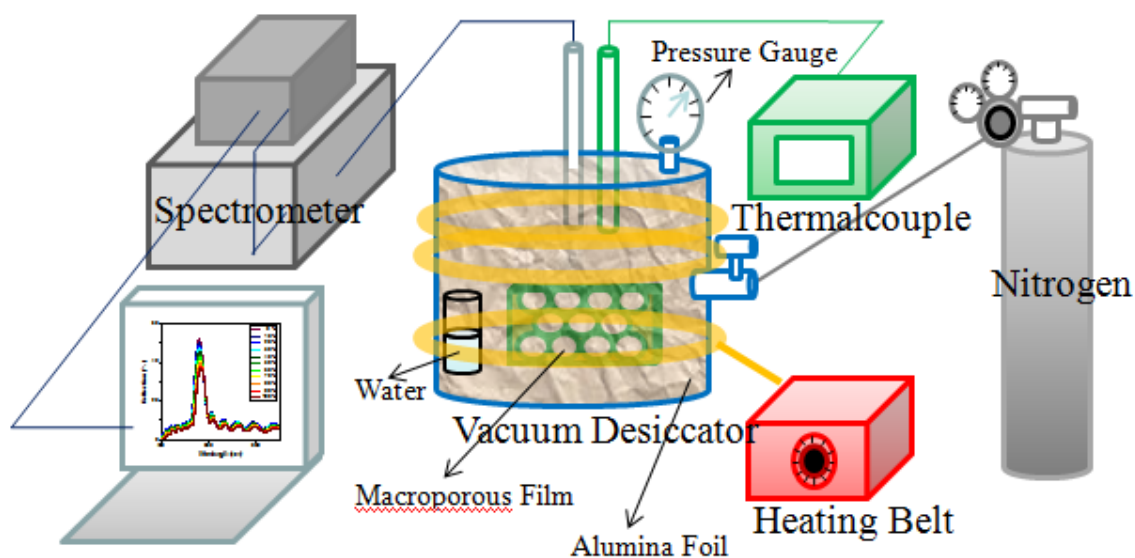


Figure 4-1. Schematic illustration of the experimental setup for vapor detection.

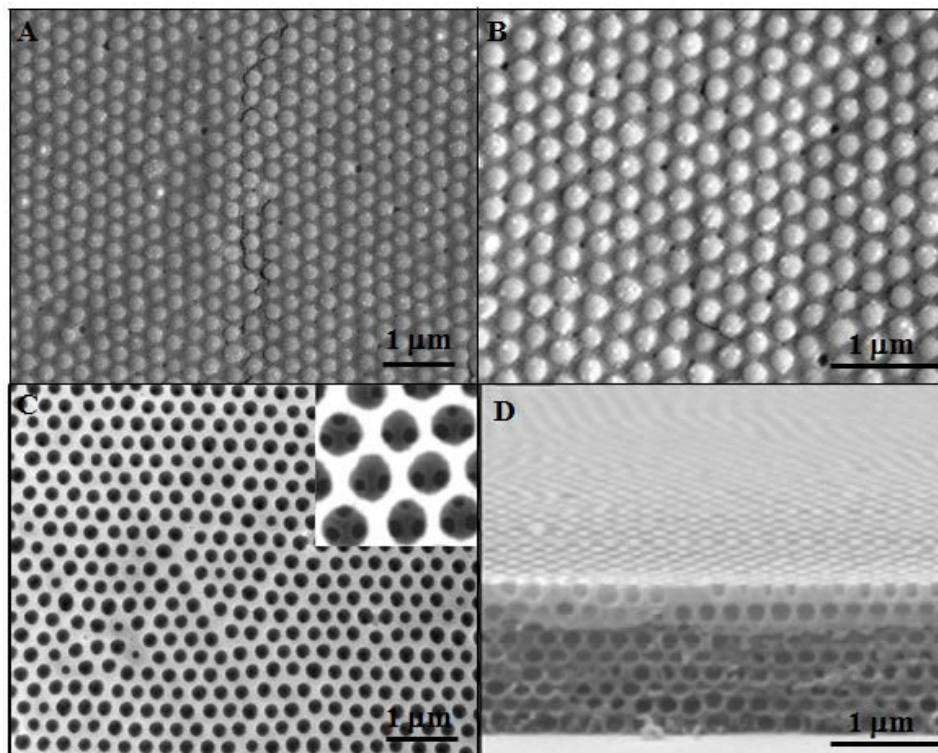


Figure 4-2. A) Top-view SEM image of a doctor blade coated silica colloidal crystal-polymer composite consisting of 320 nm silica spheres. B) Magnified image of A). C) Top-view SEM image of a templated macroporous polymer film. Inset showing a magnified portion of the film. D) Cross-sectional SEM image of the same sample as in C).

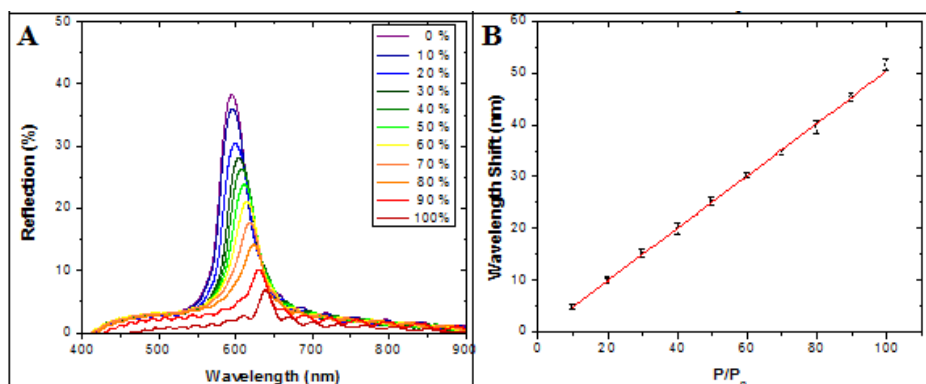


Figure 4-3. A) Normal-incidence specular reflection spectra obtained from a macroporous polymer film consisting of 320 nm air cavities exposed to ethanol vapors with different partial pressures. B) Dependence of the wavelength shift of the Bragg diffraction peak vs. ethanol partial pressure.

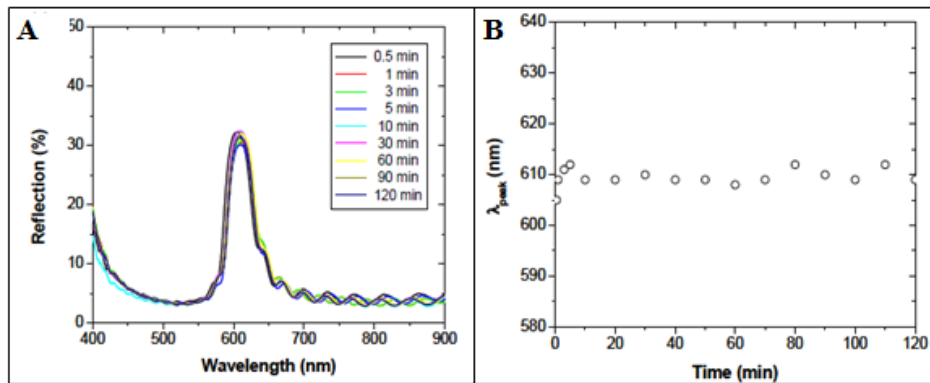


Figure 4-4. A) Time dependence of specular reflection spectra obtained from a macroporous polymer film exposed to ethanol vapor with a partial pressure of  $0.5 P_0$ . B) Variation of the wavelength of Bragg diffraction peak vs. ethanol vapor exposure time.

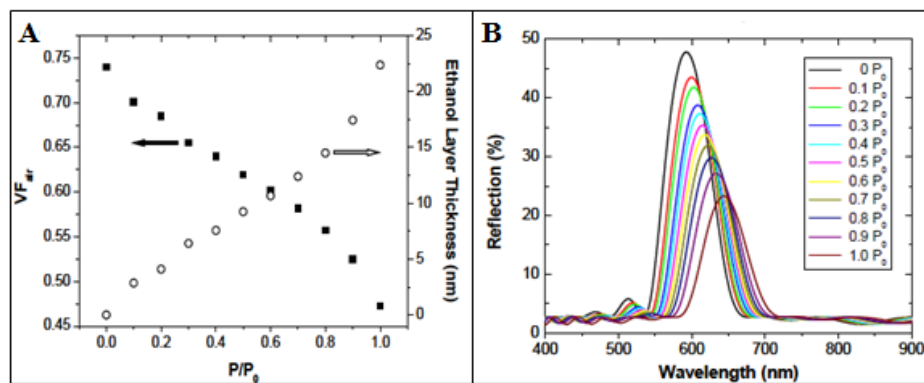


Figure 4-5. A) Calculated volume fractions of air and the corresponding adsorbed ethanol layer thickness at different ethanol partial pressures. B) Simulated specular reflection spectra obtained from a macroporous polymer film consisting of 320 nm cavities exposed to ethanol vapors with different partial pressures.

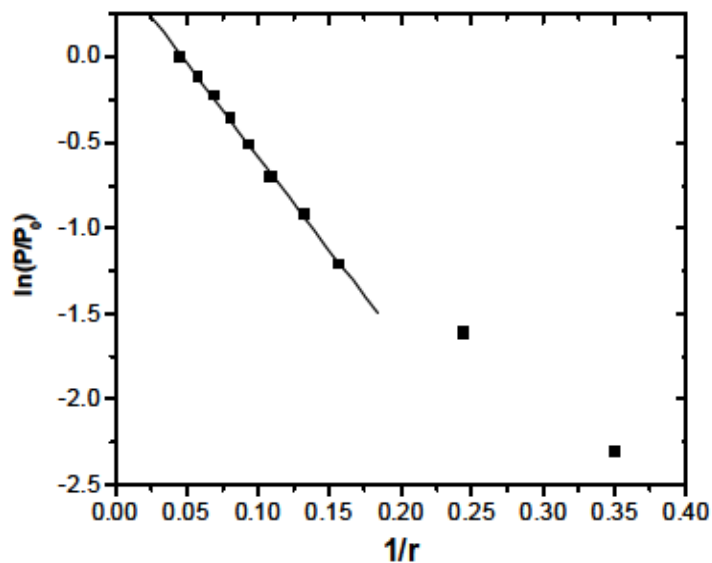


Figure 4-6. Dependence of  $\ln P/P_0$  vs. the reciprocal of the radius of curvature of the condensed liquid films.

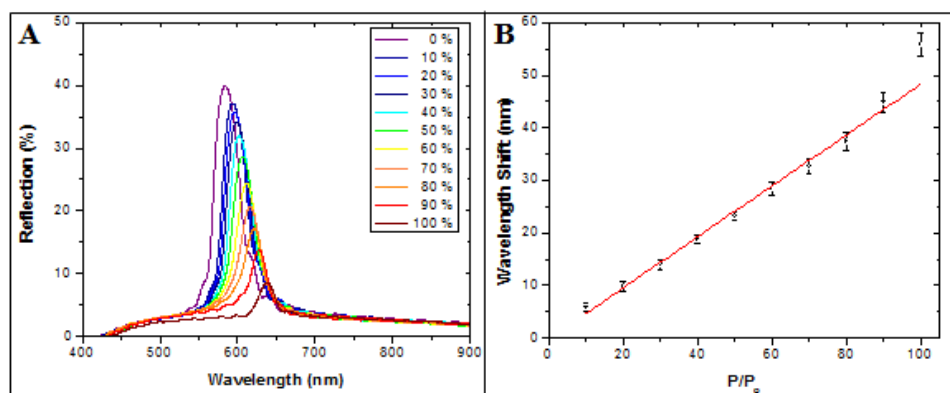


Figure 4-7. A) Normal-incidence specular reflection spectra obtained from a macroporous polymer film consisting of 320 nm air cavities exposed to water vapors with different partial pressures. B) Dependence of the wavelength shift of the Bragg diffraction peak vs. water partial pressure.

## CHAPTER 5 SELF-ADJUSTING SMART WINDOWS

Smart windows are used in building and automotive applications in order to control the incident daylight and glare, according to occupant comfort. The control of sun light can be achieved by electrically switchable chromogenic materials, which are able to electrically change either their color or transmittance. They are, respectively, based on electrochromic systems, which change their color as a consequence of oxidation-reduction reactions, and liquid crystal systems that allow controlling their transmittance by the electrical-driven director reorientation. However, the devices require continuous power resulting in a power consumption of 5 up to 20 W/m<sup>2</sup>, while also long-term UV stability and high cost remain issues.

Thermochromic materials are capable of displaying different colors at different temperatures. The most widely studied thermochromic material, and the best candidate for large area thermochromic smart window applications is VO<sub>2</sub> and various doped forms of VO<sub>2</sub>.<sup>200</sup> However, the visible transmittance is relatively low at both high temperature and low temperature. Therefore, the major challenges for development of large area smart windows, which are useful for energy control in buildings is the development of materials or devices that have a high visible transmittance, require low energy to transite states, and with a transition temperature close to room temperature.

### **5.1 Experimental Procedure**

Macroporous polymer photonic crystals with three-dimensional crystalline arrays of voids are fabricated by the scalable doctor blade coating technology. In this methodology, monodispersed silica microspheres are dispersed in a nonvolatile monomer ethoxylated trimethylolpropane triacrylate, to make colloidal suspensions with

particle volume fraction of ca. 50%. An immobilized and vertically beveled razor blade which gently touches with a substrate applies a uniform shear force to align silica microspheres when the substrate is moved at a controlled speed. The monomer is finally photopolymerized to form colloidal crystal-polymer composites. The embedded silica microspheres can then be completely removed by etching in a 2 vol % hydrofluoric acid aqueous solution. After drying, the resulting self-standing macroporous polymer films exhibit uniform and shining colors.

## **5.2 Results and Discussion**

The self-standing macroporous polymer films exhibit brilliant colors which originate from the Bragg diffractive of visible light from the three-dimensional highly ordered air cavities. The colors can be easily changed by tuning the size of the air. Figure 5-1 shows the methodology for self-adjusting smart windows. When the temperature is higher outside of the glazed buildings (ex. in summer), ethanol is evaporated by in-situ heating, resulting in the macroporous polymer films exhibit brilliant greenish color. Certain range wavelength of solar radiation can be reflected, the solar radiation penetrate through the film is then reduced. When the temperature is lower outside of the glazed buildings (ex. in winter), the air cavities are filled with a solvent which has the same refractive index as that of the polymer, the macroporous polymer films becomes completely transparent due to the index matching. All of the solar radiation can then penetrate through the sample. Therefore, the building's energy consumption can be reduced. This process is highly reversible and reproducible for thousands of cycles. The blocked solar radiation wavelength range also can be adjusted by introducing different size of silica particles in the doctor blade coating process.

The ordering of silica microspheres is clearly evident from the typical top-view SEM image as shown in Figure 5-2A. The polymer matrix surrounding the silica microspheres is clearly seen. Figure 5-2B shows a photograph of wafer-scale multilayer silica colloidal crystal/ETPTA composite consisting of 260 nm silica microspheres illuminated with white light. The sample is prepared by doctor blade coating a 50 vol % suspension at 0.1  $\mu\text{m/s}$ . It exhibits a uniform red color caused by Bragg diffraction of visible light from the crystalline lattice.

We therefore selectively etched out silica particles in the composites by a brief hydrofluoric acid (2 vol %) wash to create macroporous polymers. The structure does not collapse during the etching process, and the resulting film is easy to break to reveal the cross-section of the crystal. The typical SEM image of the top surface of a macroporous film as shown in Figure 5-2C reveals that the hexagonal ordering of the shear-aligned composite is well retained during the wet-etching process. The large voids templated from silica microspheres are interconnected through smaller pores that originate from the touching sites of silica particles in the composites. Figure 5-2D shows a photograph of a free-standing macroporous ETPTA membrane templated from 260 nm silica spheres. The film exhibits a striking green color caused by the Bragg diffraction of visible light from the crystalline lattice of air cavities in the polymer.

Figure 5-3 show the optical reflection spectra during the color change process. When the air cavities are filled with ethanol (refractive index of ethanol is close to that of the polymer), the sample changes color to red and becomes transparent. When ethanol is evaporated by in-situ heating, the sample color changes back to green.

Proof-of-concept experimental set-up for self-adjusting smart windows is shown in Figure 5-4. Three transparent glass boxes are filled in 500 mg ice cubes. The glass boxes are covered with aluminum foil. Transparent glass (A), macroporous polymer membrane coated glass (B), and aluminum foil covered glass (C) are then placed on the openings of the three glass boxes, respectively. The three boxes are then placed under sunshine, and the temperatures in the boxes are measured and recorded by a digital thermal couple every 10 minutes. The recorded temperatures for these three boxes are shown in Figure 5-5. The temperature of the ice cube in the aluminum foil covered glass covered box is the lowest one at the same exposure time indicates all of the solar radiation is blocked by the aluminum foil. The temperature of the ice cube in the macroporous membrane coated glass covered box is lower than the one in the pure glass covered box at same exposure time. Besides, when the macroporous membrane is filled with refractive index match liquid, the temperature in the liquid filled macroporous membrane coated glass covered box is similar to the one in the pure glass covered box at same exposure time. That indicates the set-up can be potentially used for smart window applications.

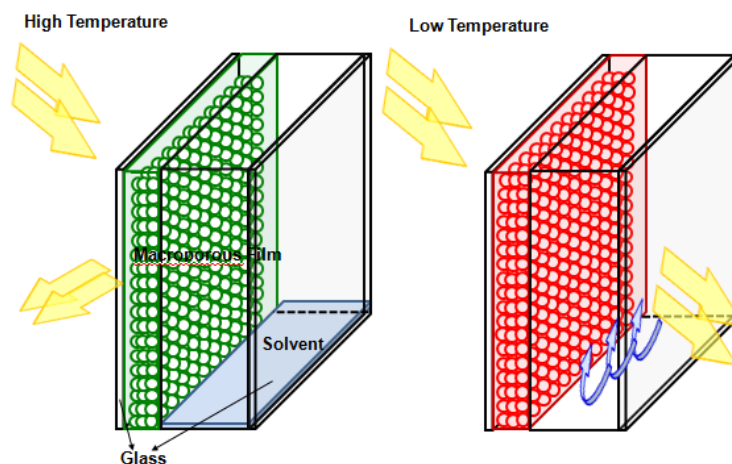


Figure 5-1. Schematic illustration of the methodology for self-adjusting smart windows.

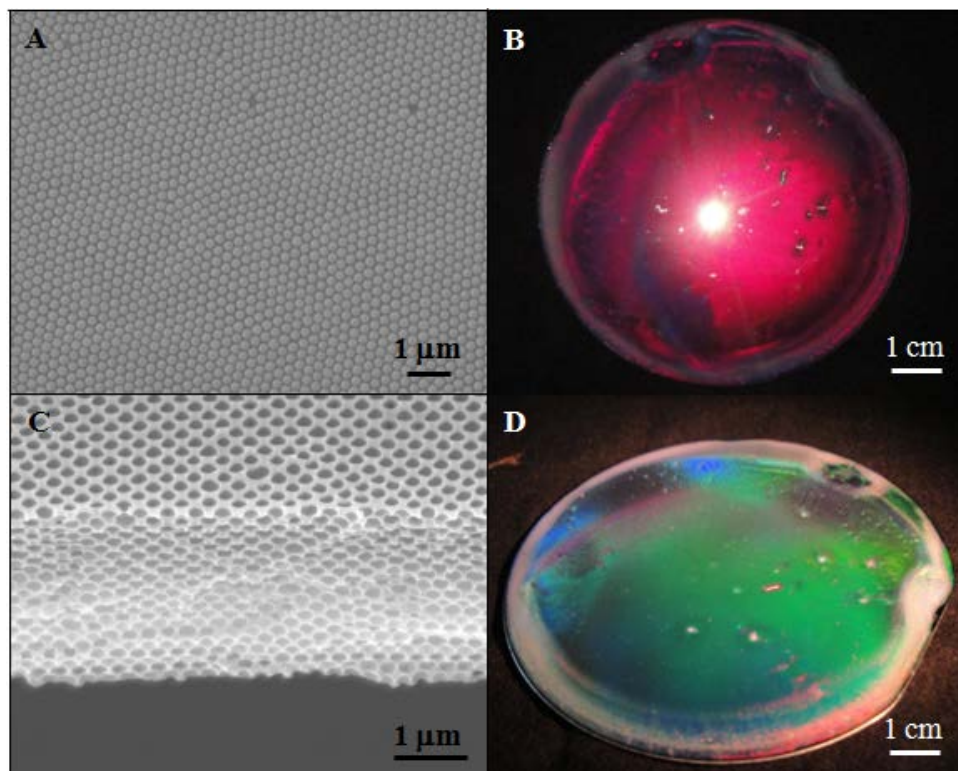


Figure 5-2. A) Top-view SEM image of a doctor blade coated silica colloidal crystal-polymer composite consisting of 260 nm silica spheres. B) Photograph of doctor blade coated silica colloidal crystal-polymer composite. C) Cross-sectional SEM image of a templated macroporous polymer film. D) Photograph of a template macroporous film.

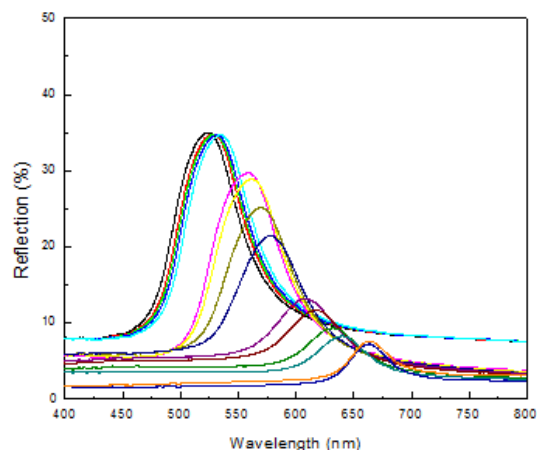


Figure 5-3. Optical reflection spectra showing the color change process when the air cavities of macroporous polymer are gradually replaced by ethanol.

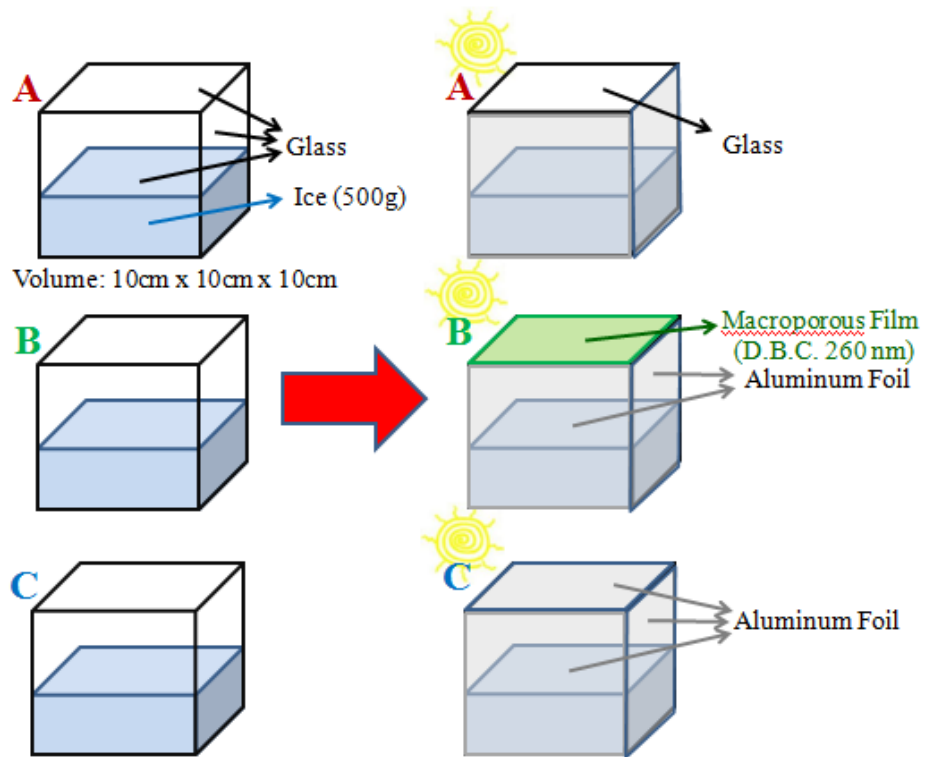


Figure 5-4. Schematic illustration of the prove-of-concept experimental setup for self-adjusting smart windows.

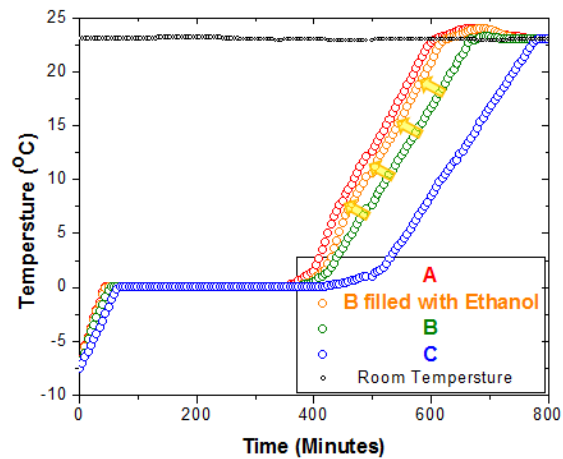


Figure 5-5. Ice cubic temperatures under different windows vs. exposure time.

## CHAPTER 6 SELF-CLEANING DIFFRACTIVE MACROPOROUS FILMS

It is well-known that both the chemical composition and the geometric structure are crucial in determining the surface wettability. The combination of hierarchical micro- and nano-scale structures with low surface energy materials, which is the origin of the water repelling properties of lotus leaves, has been demonstrated as an efficient approach to create superhydrophobic coatings with low contact angle hysteresis.

Among the various methodologies in creating superhydrophobic coatings with hierarchical structures, bottom-up colloidal self-assembly is a simple, fast, and inexpensive technique. The structures can be precisely controlled by choosing monodispersed particles with well-defined size. Air, which is the most hydrophobic material, is trapped in the sub-micrometer sized pores to significantly increase contact angles. The hydrophobicity can be further improved by functionalizing the surface of colloidal particles using low surface energy chemicals (e.g., fluorosilanes). However, several drawbacks of current colloidal self-assemblies have impeded the development and implementation of superhydrophobic coatings in practical applications. First, most of the available colloidal self-assembly technologies are only favorable for low volume, laboratory-scale production. Second, technical incompatibility with mature microfabrication is a major issue for large-scale production.

### **6.1 Experimental Procedure**

A commercial doctor blade (Fisher<sup>®</sup>, 4 cm wide) is placed vertically on the surface of a silicon wafer which has been freshly primed by 3-acryloxypropyltrichlorosilane (APTCS). The silica-ETPTA suspension is dispensed along one sidewall of the blade onto the wafer. The wafer is then dragged in a controlled speed by a syringe pump to

move the colloidal suspension across the gap between the doctor blade and the substrate. The ETPTA monomer is finally photopolymerized by exposure to ultraviolet radiation using a pulsed UV curing system for 4 seconds.

An oxygen reactive-ion etcher operated at 40mTorr oxygen pressure, 40 sccm oxygen flow rate, and 100 W is used to partially remove ETPTA matrix for releasing the embedded silica particles. The templating silica spheres are selectively removed by dropping a 2 vol % hydrofluoric acid aqueous solution on the silica/ETPTA composite for 10 seconds, followed by washing in ethanol. These procedures are repeated for three times until the ETPTA film becomes transparent in ethanol.

The hydrophobicity of macroporous ETPTA films can be improved by surface functionalization using fluorosilanes with low surface energy. The as-prepared macroporous ETPTA films are placed in a sealed vessel with a beaker containing a small amount of (tridecafluoro-1,1,2,2-tetrahydrooctyl)trichlorosilane. The vessel is then pumped to evaporate the fluorosilane to react with the moisture and the hydroxyl groups on the surface of macroporous ETPTA films.

The apparent water contact angle is measured using a goniometer (NRL C.A. goniometer, Rame-Hart Inc.) with autopipetting and imaging systems. Using the autopipetting system and DROPimage advanced software, a 13  $\mu$ L water droplet is dispensed onto the sample surface. Apparent water contact angle is determined by using ImageJ v1.37 with the drop analysis plugin. Some manual adjustment of the 7-knot snake is required before the curve can be snaked accurately. Analysis of each image yields a left and right contact angle. This process is repeated eight times for each

sample, yielding 16 angle measurements per sample. The average of these 16 values is the apparent contact angle reported.

The self-cleaning properties of the template macroporous polymer films are evaluated by measuring the bacterial contamination after the samples are exposed to *Escherichia coli*-ampicillin solution. During the experiment, samples with different wettability are cut into 2 x 2 cm<sup>2</sup> specimens and placed on a sterilized plastic substrate. 0.05mL of *Escherichia coli*-ampicillin solution with 5 x 10<sup>4</sup> colony forming units (CFU) per milliliter is uniformly sprayed on the surface of the specimens. The specimens are then offered an inclining angle of 5° for 5 seconds right after the *Escherichia coli*-ampicillin solution is sprayed. The specimens are finally submerged in Luria-Bertani (LB) broth medium and cultured at 37°C for 24 hours before measuring the equivalent CFU. All experiments are performed in dark.

An Ocean Optics<sup>®</sup> spectrometer with a reflection probe is used for reflectance measurements. A calibrated halogen light source is used to illuminate the sample. The beam spot size is about 3 mm on the sample surface. Measurements are performed at normal incidence and the cone angle of collection is less than 5°. Absolute reflectivity is obtained as ratio of the sample spectrum and the reference spectrum. The reference spectrum is the optical density obtained from an aluminum-sputtered (1000 nm thickness) silicon wafer. Final value of absolute reflectivity is the average of several measurements obtained from different spots on the sample surface.

## **6.2 Results and Discussion**

Figure 6-1 shows the schematic illustration of the experimental procedures for preparing multifunctional macroporous polymer films. We start to fabricate three-dimensional highly ordered silica colloidal crystal-polymer composites by using a simple

and scalable doctor blade coating technology. In a typical DBC process, monodispersed silica microspheres with diameter ranging from 200 to 700 nm are dispersed in a nonvolatile monomer, ethoxylated trimethylolpropane triacrylate (ETPTA), to make colloidal suspensions with particle volume fraction of ca. 50%. An immobilized and vertically beveled razor blade which gently touches with a substrate applies a uniform shear force to align silica microspheres when the substrate is moved at a controlled speed. The monomer is finally photopolymerized to form colloidal crystal-polymer composites. The shear-aligned particles are close-packed and embedded in an ETPTA matrix. The protrusion depth of the top-layer silica spheres can be controlled by briefly applying oxygen reactive-ion etching (RIE) for various durations. The templating silica spheres can then be completely removed by etching in a 2 vol % hydrofluoric acid aqueous solution. The resulting macroporous polymer film is finally surface modified by exposing to a vapor of (tridecafluoro-1,1,2,2-tetrahydrooctyl) trichlorosilane with low surface energy. This silane coupling agent can be readily hydrolyzed with the surface moisture on the macroporous polymer to form reactive silanolic hydroxyl groups that can condense with the hydroxyl groups on the surface of macroporous polymer created by oxygen RIE treatment.<sup>201</sup> Similar surface modification of polymers (e.g., PMMA) with fluorosilanes has been widely used in creating releasing promoter layers for nanoimprint lithography.<sup>202</sup>

Figure 6-2 shows top-view SEM images of macroporous ETPTA films templated from 260 nm silica spheres. These films are prepared by plasma etching a doctor blade coated composite at 40 mTorr oxygen pressure, 40 sccm oxygen flow rate, and 100 W for 5, 10, 20, 25, 30, and 40 seconds, followed by selective removal of the templating

silica spheres. The size of the top-layer voids is measured by averaging over 100 cavities, and the results are summarized in Figure 6-3. From Figures 6-2 and 6-3, it is evident that the void size increases with the oxygen RIE time at the beginning. When the etching time reaches ~ 30 seconds, the top hemispheres of silica particles are exposed, resulting in the maximum void size ( $239 \pm 13$  nm) which is close to the diameter of templating silica spheres. After that, smaller voids are obtained as only the bottom parts of the silica spheres are templated. Another interesting feature of these macroporous polymer films is the small nanopores that interconnect the large voids defined by the silica spheres. These nanopores are originated from the touching sites between neighboring particles in the original colloidal crystal-polymer composites.<sup>203</sup> We have previously demonstrated that these uniform nanopores enable the size exclusive separation of particles with different sizes.

The apparent water contact angles (CA) of the fluorosilane-modified macroporous ETPTA films are measured by a dynamic contact angle analyzer. Figure 6-4A–C shows the water drop profiles used to determine the apparent water CAs on macroporous ETPTA films after 0, 30, and 40 seconds oxygen RIE treatments. Figure 6-4D compares averaged apparent water CAs of macroporous ETPTA films etched at different RIE durations. It is apparent that the water CAs follow the same trend as the size of the voids with different etching durations as shown in Figure 6-3. A maximum water CA of  $155 \pm 1^\circ$  is achieved at 30 seconds oxygen RIE time. This demonstrates that superhydrophobic surfaces can be obtained on the surface-modified macroporous polymer films, although the apparent water CAs of a flat ETPTA film (without oxygen

RIE) and a fluorosilane-modified flat ETPTA film are only  $78 \pm 3^\circ$  and  $115 \pm 1^\circ$ , respectively.

The above static water CA alone is insufficient for the complete evaluation of the dewetting properties of the template macroporous polymer films.<sup>204</sup> We therefore measure the advancing and receding contact angles associated with the increase and decrease of droplet volumes using the above dynamic contact angle analyzer. Panels A and B in Figure 6-5 show the water drop profiles used to measure the advancing and receding CAs on the superhydrophobic macroporous ETPTA film after 30 seconds oxygen RIE treatment. The corresponding advancing and receding CAs are  $156^\circ$  and  $152^\circ$ . The measured dynamic CAs and sliding angles for macroporous ETPTA films etched at different oxygen RIE durations are summarized in Figure 6-5C,D. Once again, we find a clear trend of the sliding angle with the size of the templated voids. The sliding angle becomes smaller when the void size increases. By comparing Figures 6-5D and 6-4D, it is evident that a larger apparent water CA is associated with a smaller sliding angle.

The experimental results on the wettability of macroporous polymer films can be quantitatively explained by adapting the traditional dewetting models.<sup>205-206</sup> In Wenzel's model, complete wetting of all surface features (interconnecting voids in this case) leads to eq 1:

$$\cos \theta' = r \cos \theta$$

where  $\theta'$  is the apparent CA on a rough surface,  $\theta$  is the intrinsic CA on a flat surface, and  $r$  is the surface roughness factor defined by the ratio of the total area in contact with the liquid to the projected area. If Wenzel's wetting occurs, the filling of air cavities by

water will lead to a higher efficient refractive index and a smaller refractive index contrast. This will cause a red shift of the Bragg diffraction peak and reduced reflection amplitude. However, the templated macroporous films retain the shining green color even after complete immersion in water. We therefore adapted Cassie's model to explain our experimental observations. In Cassie wetting, the liquid droplet wets a composite surface consisting of both solid (polymer in this case) and entrapped air. This incomplete wetting can be described by the Cassie equation (eq 2)

$$\cos \theta' = f \cos \theta - (1-f)$$

where  $f$  is the fraction of the area of the polymer in direct contact with the liquid droplet.

We can estimate the area fraction of the polymer/water interface,  $f$ , by using a simple trigonometric calculation (eq 3) as

$$f = 1 - \frac{\pi R_v^2}{2\sqrt{3}R_s^2}$$

where  $R_v$  is the radius of voids measured by the top-view SEM images as shown in Figure 6-2 and  $R_s$  is the radius of the templating silica spheres. The calculated water CAs using the Cassie's model are compared with the experimental data in Figure 6-6. The slopes of the experimental and theoretical results are comparable, though the experimental CAs are slightly larger than the theoretical predictions. This is reasonable as we assume the water droplet forms a flat surface on the macroporous film to derive eq 3. In reality, the water droplet will slightly penetrate into the top-layer voids. This will increase the contact area of water and entrapped air and thus leads to a larger effective  $(1-f)$ , in other words, a smaller effective  $f$ . This will move the experimental data closer to the theoretically predicted curve. Further experiments show that macroporous ETPTA

membranes templated from larger silica spheres (560 and 700 nm) exhibit similar dewetting behavior as depicted in Figure 6-6, indicating the Cassie's model is still valid for these large-pores films.

We have shown above that superhydrophobic surface with large CA ( $>150^\circ$ ) and small sliding angle ( $<5^\circ$ ) can be obtained on fluorosilane-modified macroporous polymer films. This unique combination is highly favorable for developing self-cleaning coatings. We further evaluate the self-cleaning properties of the macroporous films by measuring the bacterial contamination after the samples are exposed to *Escherichia coli*-ampicillin solution. After spraying 0.05 ml of *Escherichia coli*-ampicillin solution with  $5 \times 10^4$  CFU/ml on the surface of the samples, the specimens are inclined at an angle of  $5^\circ$  for 5 seconds. The specimens are finally submerged in Luria-Bertani broth medium and cultured at  $37^\circ\text{C}$  for 24 h before measuring the equivalent CFU. Figure 6-7 displays the photographs of bacterial cultures of *Escherichia coli*-ampicillin on a flat ETPTA film, a surface-modified flat ETPTA film, a surface-modified macroporous ETPTA film without oxygen RIE treatment, and a surface-modified macroporous ETPTA film with 30 seconds oxygen RIE. The counted colony forming units for these four samples are shown in Figure 6-8. Compared with a flat ETPTA specimen with a water CA of  $78 \pm 3^\circ$ , ~86% of bacteria are left on the surface-modified flat ETPTA specimen (water CA of  $115 \pm 1^\circ$ ), nearly 8% of bacteria are left on the surface-modified macroporous ETPTA specimen without RIE treatment (water CA of  $136 \pm 1^\circ$ ), and less than 1% of bacteria are left on the surface-modified macroporous ETPTA specimen with the maximum water CA ( $155 \pm 1^\circ$ ). The significant lowering of the bacterial contamination on the macroporous ETPTA specimen with small sliding angle is due to the fact that most of

the bacterial solution rolls off from the superhydrophobic surface when an inclining angle of  $5^\circ$  is applied.

Besides the self-cleaning functionality facilitated by the superhydrophobic surface layer, the three-dimensional highly ordered structure of the bulk macroporous polymer films could enable other important technological applications in diffractive optics (e.g., filters, optical switches, and low-threshold lasers).<sup>207-209</sup> We evaluate the optical properties and the crystalline quality of macroporous polymer films by measuring their optical reflectance at normal incidence using an Ocean Optics<sup>®</sup> visible-near-IR spectrometer with a reflection probe. The experimental reflectance spectrum in Figure 6-9A (dark line) shows distinctive peaks caused by Bragg diffraction of visible light from the three-dimensional ordered structure. The optical measurements are complimented by theoretical calculation using a scalar-wave approximation (SWA) model. The calculated spectrum in Figure 6-9A (red line) from a macroporous ETPTA film with close-packed 260 nm voids and 12 monolayers agree reasonably well with the experimental spectrum. This further confirms the high crystalline quality of the templated macroporous polymers.

As the hydrophobicity of the macroporous films is mostly originated from the porous top layer, while the optical diffraction is mainly contributed by the stacked multi-layers, we speculate that the brief oxygen RIE process which is used to control the size of the top-layer voids will have small effect on the final optical properties of the macroporous films. Figure 6-9B shows the optical reflectance measurements on 11 samples created by oxygen RIE of a macroporous ETPTA film templated from 260 nm silica spheres for different durations. Although the amplitude of the zero<sup>th</sup>-order

diffraction peak located at 482 nm reduces slightly with longer etching time, the shift of the peak position is less than 1 nm for all samples. As the diffraction amplitude is sensitive to the crystalline thickness, the effect of oxygen etching on the final reflectance can be significantly reduced by using thicker films.

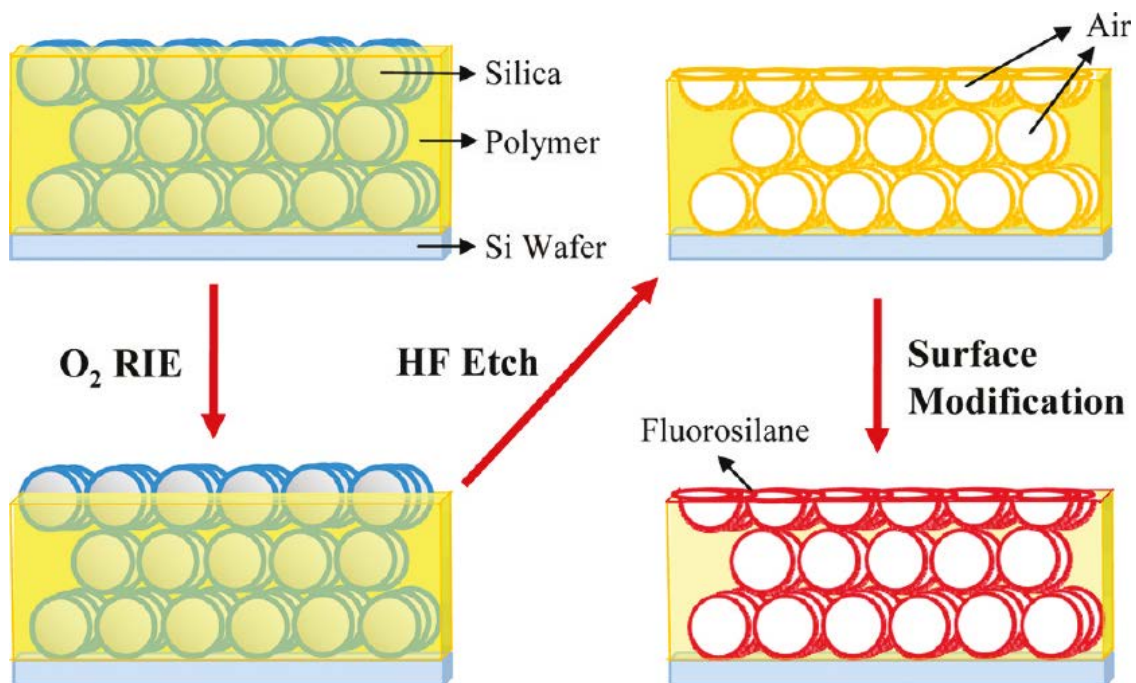


Figure 6-1. Schematic illustration of the experimental procedures for preparing superhydrophobic macroporous polymer films.

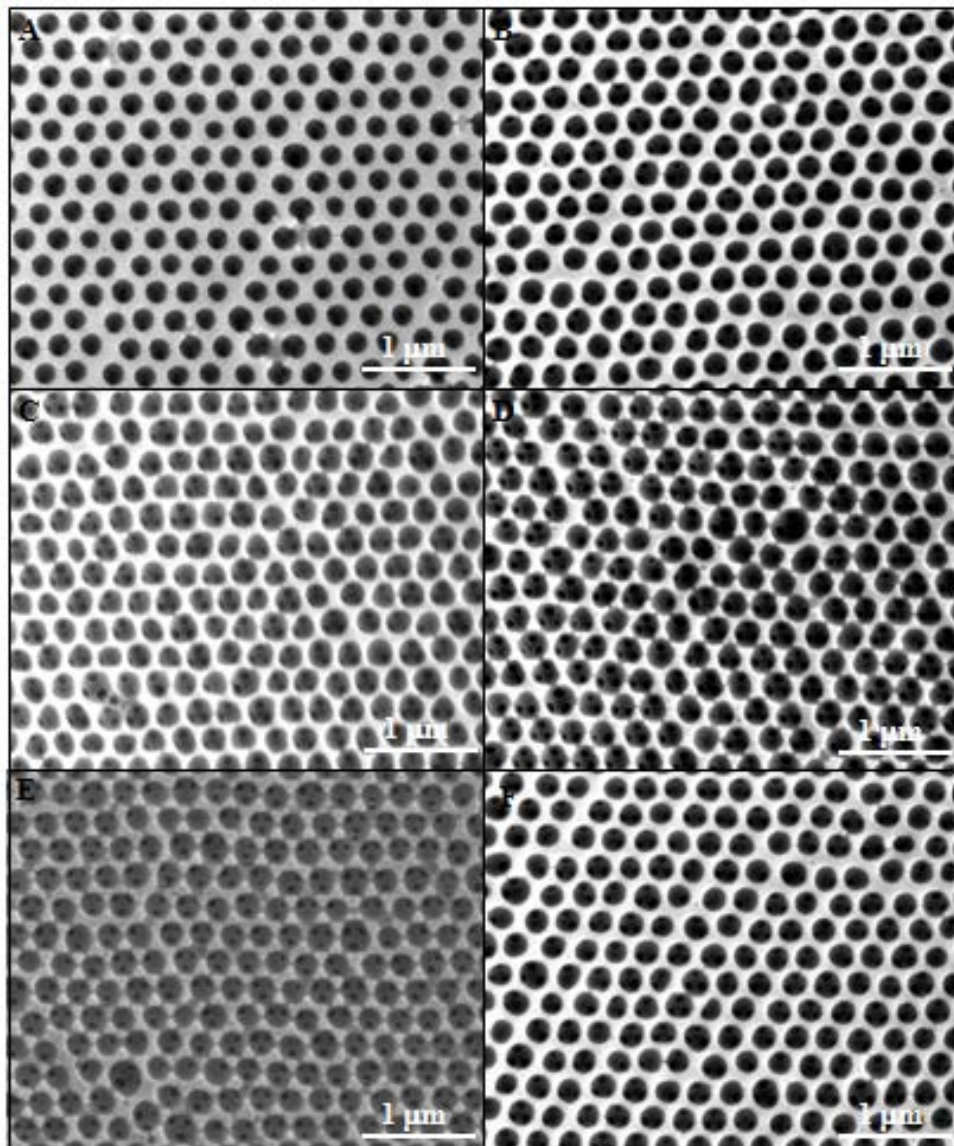


Figure 6-2. Top-view SEM images of macroporous ETPTA films templated from 260 nm silica spheres. These films were prepared by plasma etching a doctor blade coated composite at 40 mTorr oxygen pressure, 40 sccm oxygen flow rate, and 100W for (A) 5, (B) 10, (C) 20, (D) 25, (E) 30, and (F) 40 seconds, followed by selective removal of the templating silica spheres.

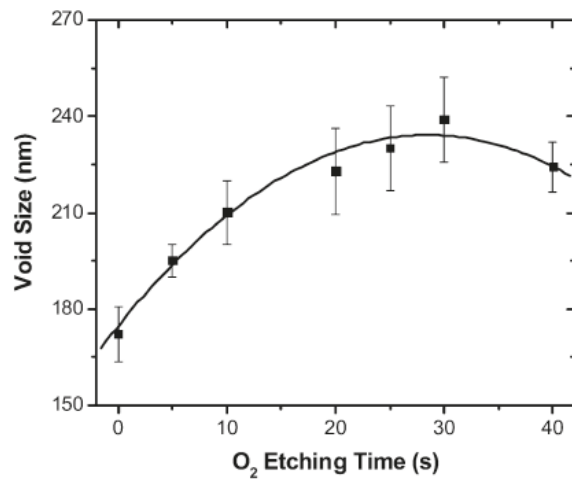


Figure 6-3. Dependence of the void size of macroporous ETPTA films templated from 260 nm silica spheres vs oxygen RIE etching time.

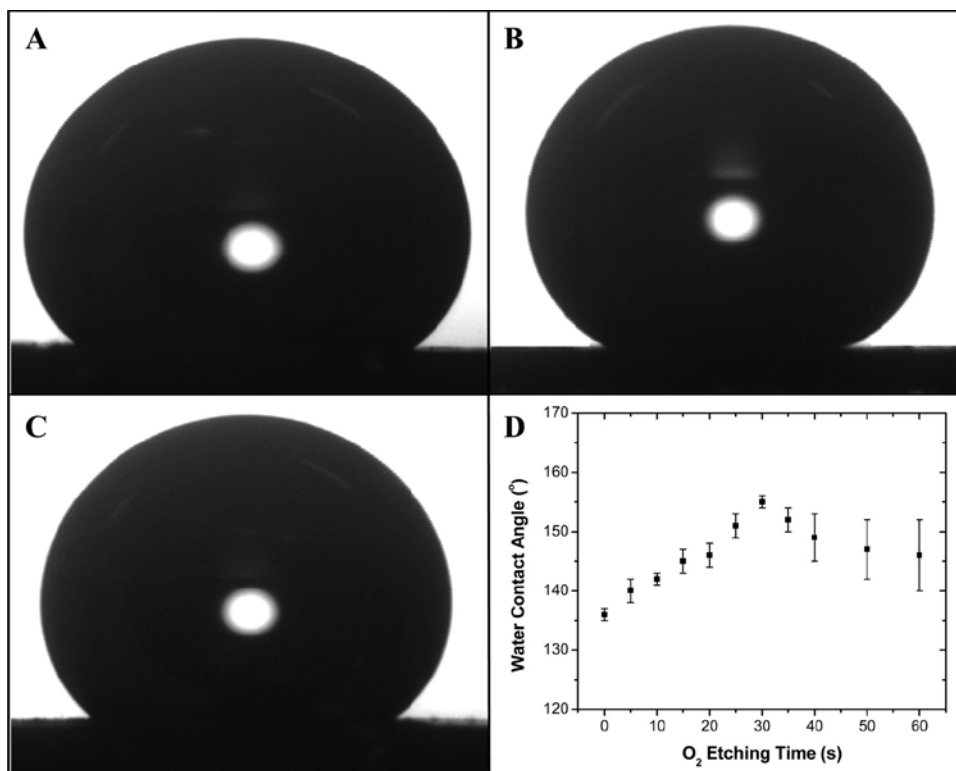


Figure 6-4. (A-C) Water drop profiles on fluorosilane-modified macroporous ETPTA films after 0, 30, and 40 seconds oxygen plasma etching. (D) Apparent water contact angles of fluorosilane-modified macroporous ETPTA films etched at different RIE durations.

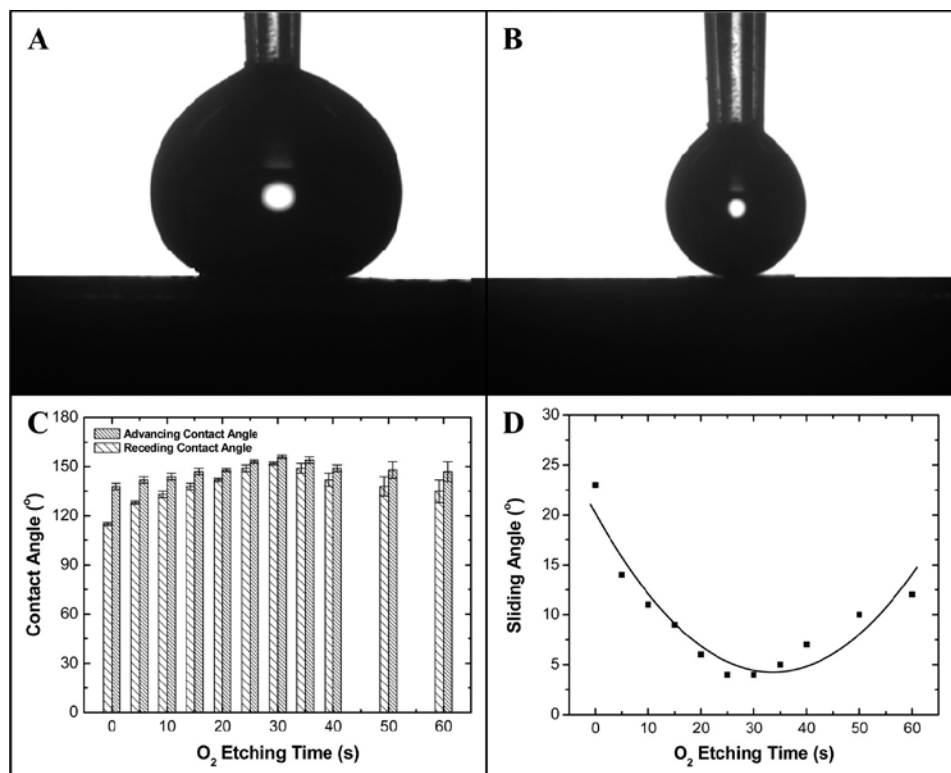


Figure 6-5. (A, B) Water drop profiles used to determine the advancing and receding water contact angles on a fluorosilane-modified macroporous ETPTA film after 30 seconds oxygen RIE. (C) Advancing and receding water contact angles of fluorosilane-modified macroporous ETPTA film etched at different RIE durations. (D) Sliding angles of fluorosilane-modified macroporous ETPTA film etched at different RIE durations.

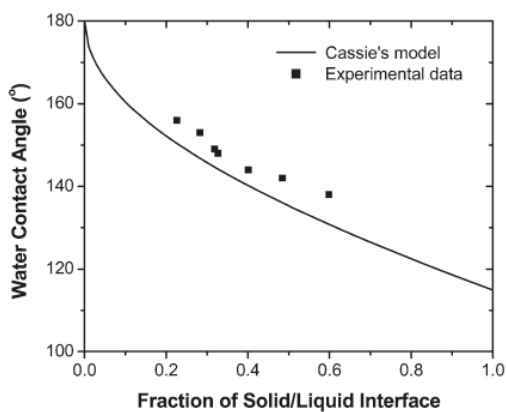


Figure 6-6. Dependence of the apparent water contact angle vs the fraction of solid/liquid interface,  $f$ . The solid line is calculated using Cassie's equation.

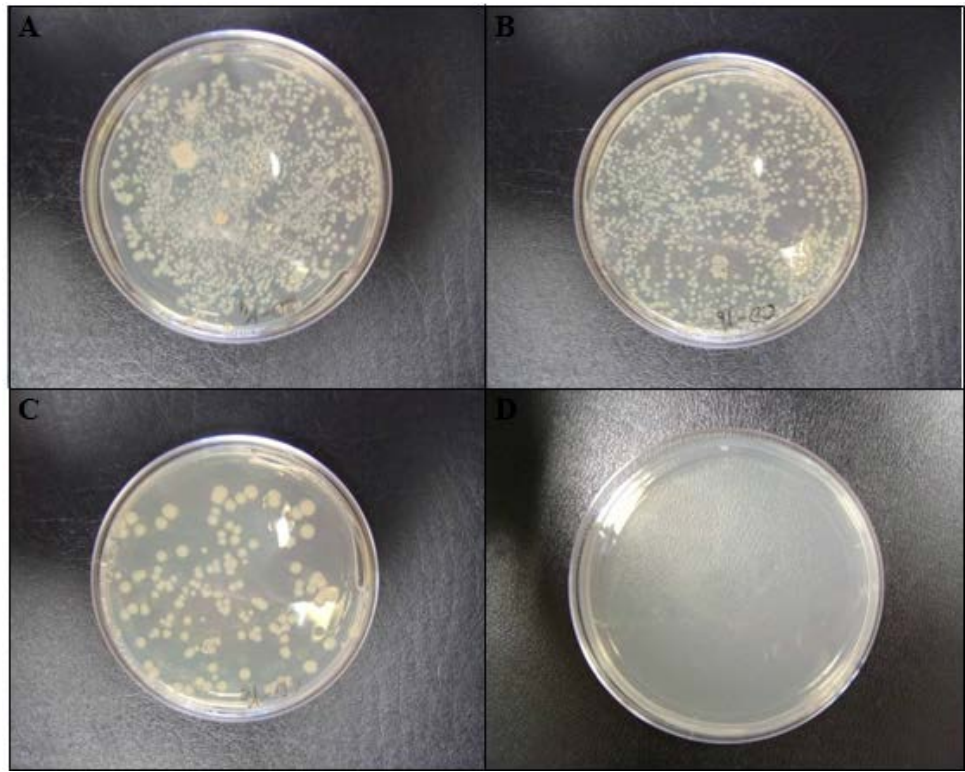


Figure 6-7. Bacterial cultures on four specimens after applying an inclining angle of 5° for 5 seconds: (A) flat ETPTA film; (B) fluorosilane-modified flat ETPTA film; (C) fluorosilane-modified macroporous ETPTA film without oxygen RIE; (D) fluorosilane-modified macroporous ETPTA film after 30 seconds oxygen RIE.

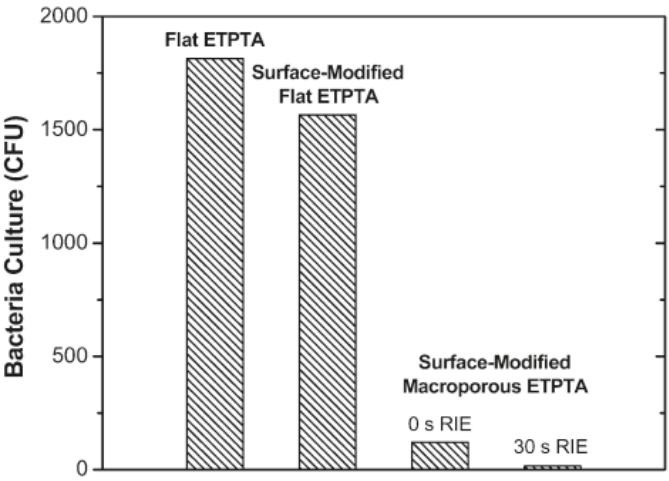


Figure 6-8. Counts of the colony forming units for the samples in Figure 7.

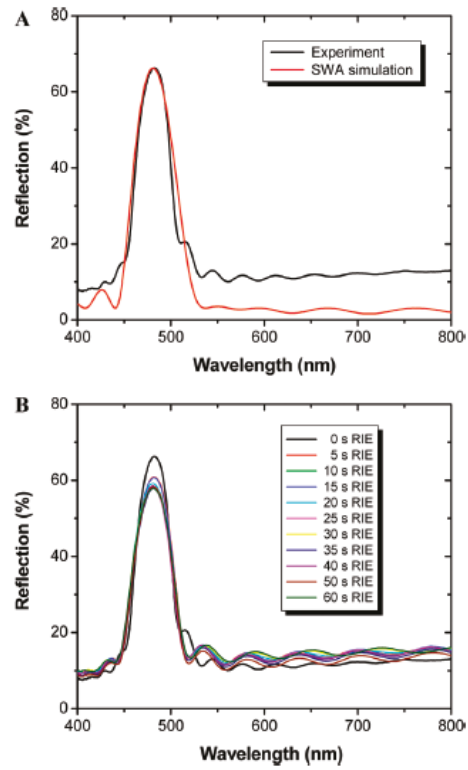


Figure 6-9. (A) Experimental (black line) and SWA-simulated (red line) optical reflection spectra at normal incidence from a macroporous ETPTA film with 260 nm air cavities and 12 layers. (B) Comparison of normal-incidence optical reflection spectra from macroporous ETPTA films etched at different RIE durations.

## CHAPTER 7 PARTICLE SEPARATIONS AND BACTERIA FILTRATIONS BY MACROPOROUS MEMBRANES

Membrane filtration is a technique which is used to separate particles from a liquid for the purpose of purifying it. This filtration method has a number of applications, ranging from treating wastewater to filtering milk used for cheese production. In membrane filtration, a solvent is passed through a semi-permeable membrane. The membrane's permeability is determined by the size of the pores in the membrane, and it will act as a barrier to particles which are larger than the pores, while the rest of the solvent can pass freely through the membrane. The result is a cleaned and filtered fluid on one side of the membrane, with the removed solute on the other side. One of the big advantages to such a system is that it does not require the use of chemicals or additives, which cuts down on operating costs. Additionally, membrane filtration requires minimal energy, and it can in fact be designed to run on almost no energy, with a pressurized system which takes advantage of gravity and forces the solvent through the membrane at a steady rate.

However, filtration membranes with uniform pore size, low cost, scalable capabilities are not developed yet. In this study, we disclose a much economic and scalable nanomanufacturing technology for creating large-area filtration membranes with well-defined pore sizes and size distribution. The particle separation and bacteria filtration by the as-prepared macroporous membranes are investigated.

### **7.1 Experimental Procedure**

A commercial doctor blade is placed vertically on the surface of a silicon wafer. Silica particles are mixed with different ratios of ETPTA and poly(ethylene glycol) acrylate (PEGA) to prepare silica-monomer suspension. The silica-monomer

suspensions are dispensed along one sidewall of the blade onto the wafer. The wafer is then dragged in a controlled speed by a syringe pump to move the colloidal suspension across the gap between the doctor blade and the substrate. The monomers are then finally photopolymerized by exposure to ultraviolet radiation. The templating silica spheres are selectively removed by applying a 2 vol % hydrofluoric acid aqueous solution. The as-prepared free-standing ETPTA/ PEGA composite macroporous membranes are used for particle separation and bacteria filtration.

Gold nanoparticles used for particle separation are produced by reduction of chloroauric acid. After dissolving chloroauric acid, the solution is rapidly stirred while a 1% solution of trisodium citrate dihydrate is added. This causes gold(III) to be reduced to neutral gold atoms. As more and more of these gold atoms form, the solution becomes supersaturated, and gold gradually starts to precipitate in the form of sub-nanometer particles. The rest of the gold atoms that form stick to the existing particles, and, if the solution is stirred vigorously enough, the particles will be fairly uniform in size. To prevent the particles from aggregating, the as-prepared gold nanoparticles are ultrasonicated before using.

The bacteria-filtration properties of the template macroporous polymer films are evaluated by measuring the bacterial contamination after *Escherichia coli*-ampicillin solution filtrates through the macroporous films. During the experiment, macroporous films with different composite ratios are cut into  $3 \times 3 \text{ cm}^2$  specimens and sandwiched in between filtration set-ups. 1 mL of *Escherichia coli*-ampicillin solution with  $5 \times 10^4$  colony forming units (CFU) per milliliter is dropped on the surface of the macroporous films. The *Escherichia coli*-ampicillin solutions, before and after filtrations, are then cultured at

37 °C for 24 hours before measuring the equivalent CFU. All experiments are performed in dark.

## 7.2 Results and Discussion

An interesting feature of these macroporous polymer films is the small nanopores that interconnect the large voids defined by the silica spheres. These nanopores are originated from the touching sites between neighboring particles in the original colloidal crystal-polymer composites. We have previously demonstrated that these uniform nanopores enable the size exclusive separation of particles with different sizes

The template macroporous membranes with open and interconnected voids can be directly used as size-exclusive filtration membranes for separating particles and other substances. Compared to common filtration membranes, such as track-etched polymer films and fiber-based membranes, the uniform size of the interconnecting nanopores and the high porosity of the templated macroporous polymers could enable more accurate fractionation of particulates and a higher flow rate. To evaluate the separation efficiency of the templated macroporous films, we conducted a simple proof-of-concept experiment using a separation apparatus as shown in Figure 7-1A. A 3-cm-diameter macroporous ETPTA membrane templated from 290 nm silica spheres was used as the filter. The size of the interconnecting pores was estimated to be ~50 nm by SEM. The testing solution was prepared by mixing ~10 nm gold nanoparticles (0.01 vol %) prepared by a chemical reduction method and 330 nm silica microspheres (0.01 vol %) in ethanol. The resulting mixture is turbid (Figure 7-1B) because of random light scattering from 330 nm silica particles. The solution can easily pass through the macroporous polymer membrane even without applying a pressure or a vacuum. The filtrate solution is transparent and shows a red color (Figure 7-1C) caused by the

distinctive surface plasmon resonance absorption of light by Au nanoparticles (Figure 7-2A). The complete removal of large silica microspheres is further confirmed by the TEM images in Figure 7-1D and Figure 7-1E showing the samples prior to and after filtration, respectively.

We further evaluated the retention of small gold nanoparticles by the macroporous separation media. Figure 7-2A compares the extinction spectra of the solutions in Figure 7-1B and Figure 7-1C. Both samples show clear surface plasmon resonance peaks at ca. 510 nm. The peak amplitude of the filtered solution is lower than that of the original mixture because of the loss of gold nanoparticles during the filtration process. We plotted the absorbance of gold nanoparticle solutions with different concentrations at 510 nm (Figure 7-2B) as a calibration curve to determine the gold nanoparticle concentrations prior to and after filtration. The results demonstrated that more than 85% of gold nanoparticles were recovered after filtration. Besides hydrophobic ETPTA, a large variety of polymers ranging from highly hydrophilic PEGDA to highly hydrophobic fluorinated polymers (e.g., perfluoroether acrylates) can be used in DBC to create macroporous filtration membranes.

Figure 7-2 shows the bacteria filtration principle. In bacteria filtration, a bacteria solution is passed through a doctor blade coated membrane. The membrane's permeability is determined by the size of the pores in the membrane, and it will act as a barrier to bacteria which are larger than the pores, while the rest of the solvent can pass freely through the membrane. The result is a cleaned and filtered fluid on one side of the membrane, with the removed bacteria on the other side. The bacteria filtration

process requires minimal energy, and it can in fact be designed to run on almost no energy.

To evaluate the bacteria filtration efficiency of the templated macroporous films by measuring the bacterial contamination before and after the filtration, we conduct a simple proof-of-concept experiment using a filtration apparatus as shown in Figure 7-4A. One milliliter of *Escherichia coli*-ampicillin solution with  $5 \times 10^4$  colony forming units (CFU) per milliliter is dropped on the surface of the macroporous films. Point one milliliter of the original and the filtrated solutions are then dispersed in Luria-Bertani broth medium and cultured at 37 °C for 24 hours before measuring the equivalent CFU. Figure 7-4 displays the photographs of bacterial cultures of *Escherichia coli*-ampicillin in an original bacteria solution (Figure 7-4B), a bacteria solution after filtration through ETPTA membrane (Figure 7-4C), and a bacteria solution after filtration through ETPTA/PEGA membrane (Figure 7-4D). Compared with the CFU of original bacteria solution, there is almost no bacterium left after the bacteria solution is filtrated. The significant lowering of the bacterial contamination after filtration through macroporous ETPTA membrane and ETPTA/PEGA membrane indicates that the doctor blade coated macroporous membranes are capable of using for bacteria filtrations.

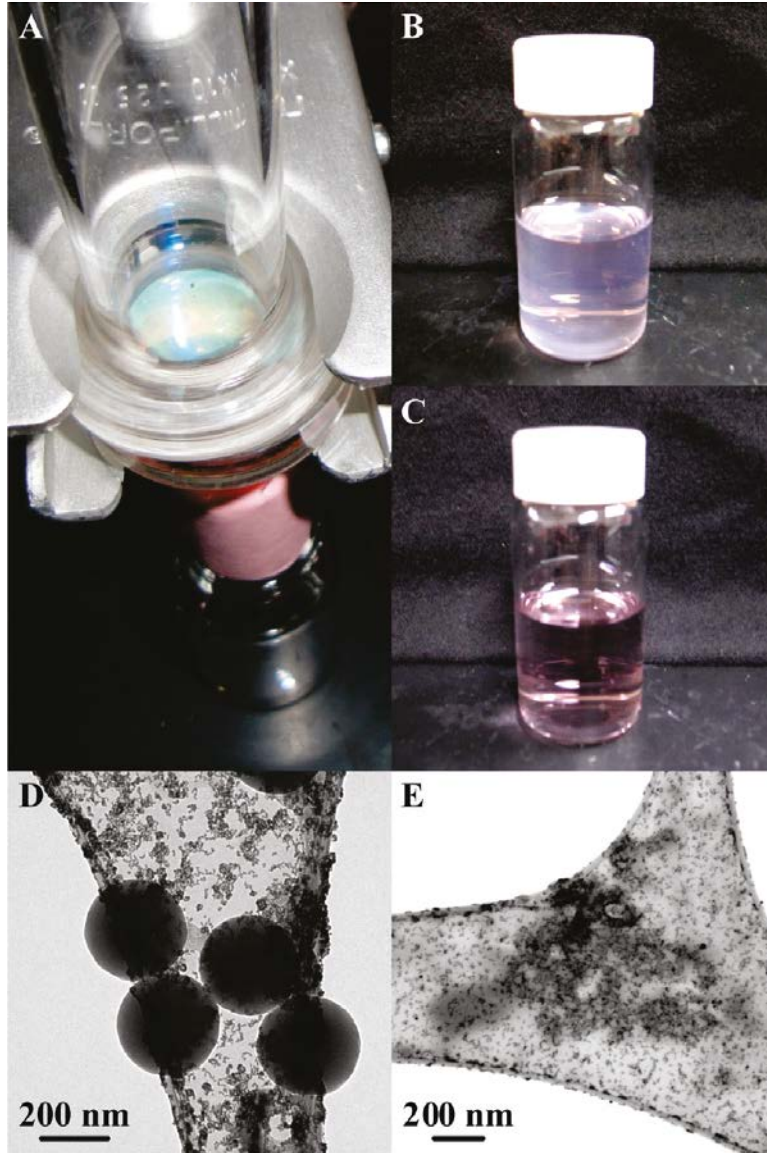


Figure 7-1. Separation of 10 nm gold nanoparticles from 330 nm silica spheres by using a free-standing, macroporous ETPTA membrane filter. (A) Experimental setup. (B) Photograph of the gold nanoparticle/silica sphere solution prior to filtration. (C) Photograph of the solution after filtration. (D) TEM image of the solution in B. (E) TEM image of the solution in C.

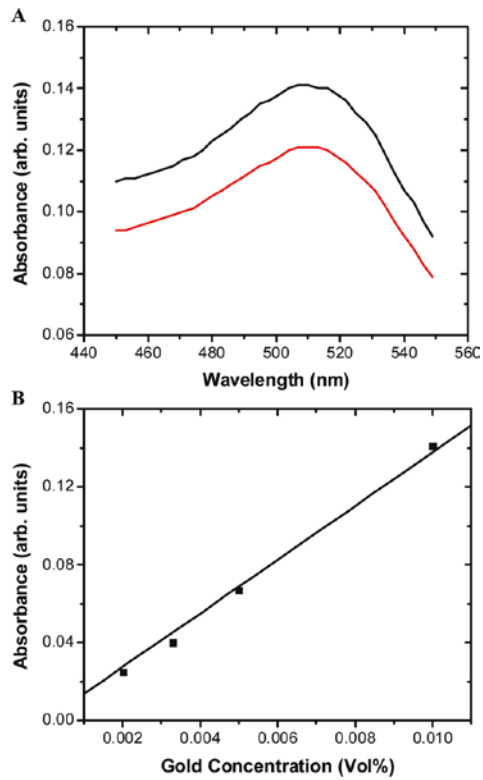


Figure 7-2. (A) Comparison of the extinction spectra of the solutions in Figure 7-1B and Figure 7-1 C. (B) Calibration curve for calculating the concentration of gold nanoparticles in filtrate solutions.

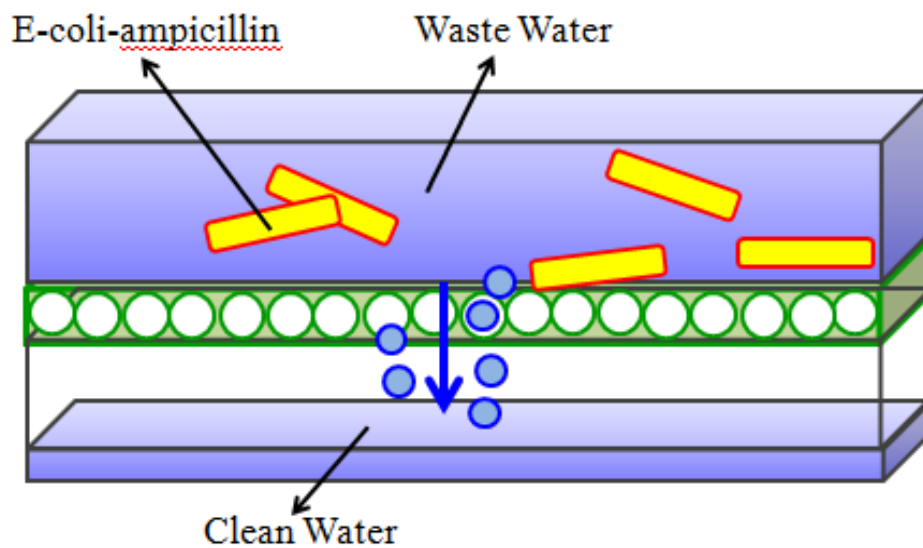


Figure 7-3. Schematic illustration of the bacteria filtration process.

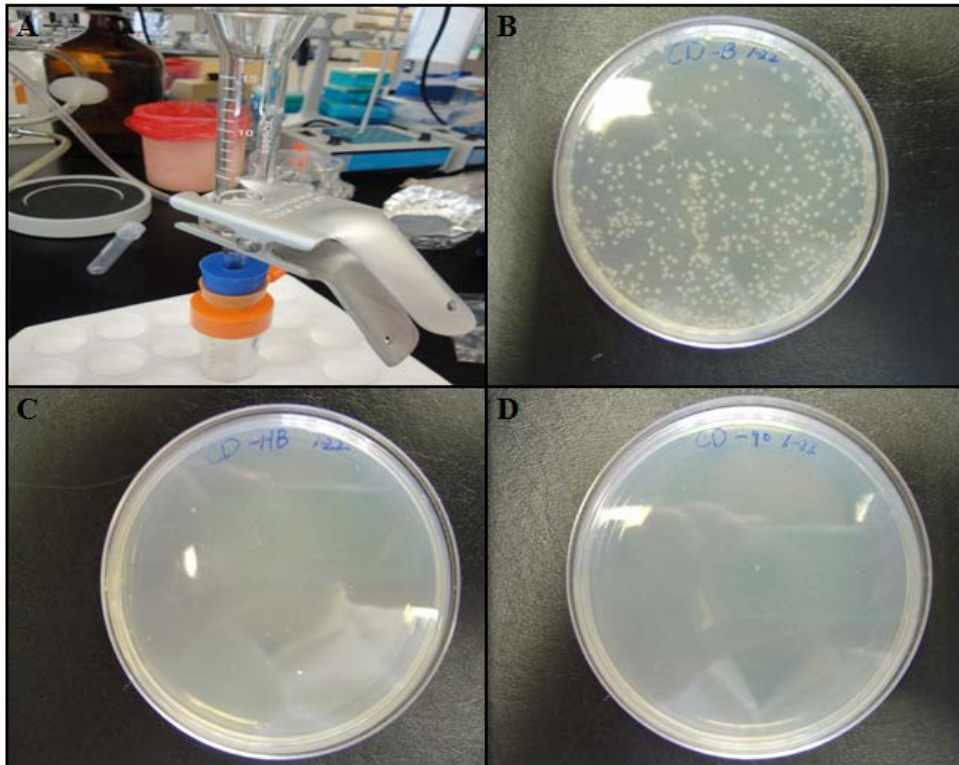


Figure 7-4. Bacterial cultures on three specimens before and after bacteria filtration: (A) Experimental setup; (B) Before Filtration; (C) After filtration through ETPTA membrane; (D) After filtration through ETPTA/ PEGA composite membrane.

## CHAPTER 8 CONCLUSIONS AND RECOMMENDATIONS

This dissertation covers five research topics which demonstrate the important applications of macroporous polymer films by doctor blade coating technology. The conclusions associated with the heat-pipe inspired color reflective displays presented in Section 8.1. The conclusions associated with the vapor detections are presented in Section 8.2. The conclusion associated smart windows are presented in Section 8.3. The conclusions associated with the superhydrophobic and self-cleaning coatings are presented in Section 8.4. The conclusion associated particle separations and bacteria filtrations are presented in Section 8.5. The recommendations for further study are presented in Section 8.6.

### **8.1 Heat-Pipe Inspired Color Reflective Displays**

A new methodology inspired by the heat pipe technology in creating reflective color displays by using doctor blade coated macroporous polymers which can be created by a simple, inexpensive, and roll-to-roll compatible fabrication technology is developed. In the technology, we use macroporous polymer with three-dimensional highly ordered air cavities as display elements. The macroporous polymer films exhibit brilliant colors. When the air cavities are filled with a solvent which has the same refractive index as that of the polymer, the macroporous polymer films becomes completely transparent due to the refractive index matching. The colors can be easily changed by tuning the size of the air cavities to cover the whole visible spectrum.

### **8.2 Vapor Detections**

It is demonstrated that a rapid and reversible vapor detection by using three-dimensional macroporous photonic crystals created by a continuous and scalable

doctor blade coating technology. Capillary condensation of a condensable vapor in the interconnected macropores leads to the increase of the effective refractive index of the diffractive medium, resulting in the red-shift of the optical stop bands. The wavelength shift is linearly proportional to the vapor partial pressure for a spectrum of vapors. Optical simulation and theoretical prediction based on Kelvin equation suggest that a liquid film is formed on the walls of the macropores during vapor condensation.

### **8.3 Smart Windows**

A rough proof-of-concept demonstration shows that the template macroporous polymer membrane can block part of solar radiation when the cavities of macroporous membrane are occupied with air. Besides, when the macroporous membrane is filled with refractive index match liquid, the membrane becomes transparent and allow solar radiation penetrate through. That indicates the set-up can be potentially used for smart window applications.

### **8.4 Superhydrophobic and Self-Cleaning Coatings**

A scalable templating technology for fabricating flexible macroporous polymer films with excellent water-repelling and optical diffractive properties is developed. All procedures involved in the fabrication of superhydrophobic macroporous films, including doctor blade coating, oxygen plasma etching, hydrofluoric acid washing, and surface functionalization, can be made compatible with roll-to-roll processing for large-scale production of flexible self-cleaning diffractive optical devices.

### **8.5 Particle Separations and Bacteria Filtrations**

We have demonstrated the separation efficiency of the template macroporous membrane filters by separating 20 nm gold nanoparticles from 330 nm silica particles. This proof-of-concept demonstration shows that almost all large silica particles have

been filtered out and the collection efficiency of gold nanoparticles is higher than 85%. Besides particle separation applications, it shows the template macroporous membrane can be applied to filtrate bacteria in water-based solutions, which potentially can be used in waste water treatment industry.

### **8.6 Recommendations**

Future work should focus on the colloidal assembly mechanism by shear aligning force. This cost effective doctor blade coating technology is beneficial to both academic and industry because it can quickly assemble 3 dimensional colloidal crystals in large scale and is compatible with current microfabrication technology. A better understanding of the formation mechanism could lead to tuning the colloidal structures which could further extend its applications.

## LIST OF REFERENCES

- (1) Betzig, E.; Trautman, J. K. *Science* **1992**, *257*, 189.
- (2) Liu, Z. W.; Wei, Q. H.; Zhang, X. *Nano Letters* **2005**, *5*, 957.
- (3) Blanco, A.; Chomski, E.; Grabtchak, S.; Ibisate, M.; John, S.; Leonard, S. W.; Lopez, C.; Meseguer, F.; Miguez, H.; Mondia, J. P.; Ozin, G. A.; Toader, O.; van Driel, H. M. *Nature* **2000**, *405*, 437.
- (4) Mayoral, R.; Requena, J.; Moya, J. S.; Lopez, C.; Cintas, A.; Miguez, H.; Meseguer, F.; Vazquez, L.; Holgado, M.; Blanco, A. *Advanced Materials* **1997**, *9*, 257.
- (5) vanBlaaderen, A.; Ruel, R.; Wiltzius, P. *Nature* **1997**, *385*, 321.
- (6) Yin, Y. D.; Lu, Y.; Gates, B.; Xia, Y. N. *Journal of the American Chemical Society* **2001**, *123*, 8718.
- (7) Ozin, G. A.; Yang, S. M. *Advanced Functional Materials* **2001**, *11*, 95.
- (8) Pieranski, P. *Contemporary Physics* **1983**, *24*, 25.
- (9) Weissman, J. M.; Sunkara, H. B.; Tse, A. S.; Asher, S. A. *Science* **1996**, *274*, 959.
- (10) Jethmalani, J. M.; Ford, W. T.; Beaucage, G. *Langmuir* **1997**, *13*, 3338.
- (11) Hayward, R. C.; Saville, D. A.; Aksay, I. A. *Nature* **2000**, *404*, 56.
- (12) Lumsdon, S. O.; Kaler, E. W.; Williams, J. P.; Velez, O. D. *Applied Physics Letter* **2003**, *82*, 949.
- (13) Garcia-Santamaria, F.; Miyazaki, H. T.; Urquia, A.; Ibisate, M.; Belmonte, M.; Shinya, N.; Meseguer, F.; Lopez, C. *Advanced Materials* **2002**, *14*, 1144.
- (14) Reculosa, S.; Ravaine, S. *Chemistry of Materials* **2003**, *15*, 598.
- (15) Vlasov, Y. A.; Bo, X. Z.; Sturm, J. C.; Norris, D. J. *Nature* **2001**, *414*, 289.
- (16) Wong, S.; Kitaev, V.; Ozin, G. A. *Journal of the American Chemical Society* **2003**, *125*, 15589.
- (17) Mihi, A.; Ocana, M.; Miguez, H. *Advanced Materials* **2006**, *18*, 2244.
- (18) John, S. *Physical Review Letters* **1987**, *58*, 2486.
- (19) Yablonovitch, E. *Physical Review Letters* **1987**, *58*, 2059.

- (20) Joannopoulos, J. D.; Villeneuve, P. R.; Fan, S. H. *Nature* **1997**, 386, 143.
- (21) Perpall, M. W.; Perera, K. P. U.; DiMaio, J.; Ballato, J.; Foulger, S. H.; Smith, D. W. *Langmuir* **2003**, 19, 7153.
- (22) Scott, R. W. J.; Yang, S. M.; Chabanis, G.; Coombs, N.; Williams, D. E.; Ozin, G. A. *Advanced Materials* **2001**, 13, 1468.
- (23) Cassagneau, T.; Caruso, F. *Advanced Materials* **2002**, 14, 1837.
- (24) Chen, H. H.; Suzuki, H.; Sato, O.; Gu, Z. Z. *Applied Physics a-Materials Science & Processing* **2005**, 81, 1127.
- (25) Kamp, U.; Kitaev, V.; von Freymann, G.; Ozin, G. A.; Mabury, S. A. *Advanced Materials* **2005**, 17, 438.
- (26) Colombelli, R.; Srinivasan, K.; Troccoli, M.; Painter, O.; Gmachl, C. F.; Tennant, D. M.; Sergent, A. M.; Sivco, D. L.; Cho, A. Y.; Capasso, F. *Science* **2003**, 302, 1374.
- (27) Arsenault, A. C.; Puzzo, D. P.; Manners, I.; Ozin, G. A. *Nature Photonics* **2007**, 1, 468.
- (28) Ozin, G. A.; Arsenault, A. C. *Nanochemistry: A Chemical Approach to Nanomaterials*; RSC, Cambridge **2005**.
- (29) Sun, Z. Q.; Yang, B. *Nanoscale Research Letters* **2006**, 1, 46.
- (30) Li, Y.; Cai, W.; Duan, G. *Chemistry of Materials* **2008**, 20, 615.
- (31) Yan, F.; Goedel, W. A. *Nano Letters* **2004**, 4, 1193.
- (32) Wang, X. D.; Lao, C. S.; Graugnard, E.; Summers, C. J.; Wang, Z. L. *Nano Letters* **2005**, 5, 1784.
- (33) Madou, M. J. *Fundamentals of Microfabrication: The science of Miniaturization*; CRC, Boca Raton, FL, **2002**.
- (34) Hulteen, J. C.; Vanduyne, R. P. *Journal of Vacuum Science & Technology a-Vacuum Surfaces and Films* **1995**, 13, 1553.
- (35) Kosiorek, A.; Kandulski, W.; Chudzinski, P.; Kempa, K.; Giersig, M. *Nano Letters* **2004**, 4, 1359.
- (36) Jiang, P.; Mcfarland, M. J. *Journal of the American Chemical Society* **2004**, 126, 13778.
- (37) Jiang, P.; Mcfarland, M. J. *Journal of the American Chemical Society* **2005**, 127, 3710.

- (38) Jiang, P.; Hwang, K. S.; Mittleman, D. M.; Bertone, J. F.; Colvin, V. L. *Journal of the American Chemical Society* **1999**, *121*, 11630.
- (39) Schroden, R. C.; Al-Daous, M.; Blanford, C. F.; Stein, A. *Chemistry of Materials* **2002**, *14*, 3305.
- (40) Vlasov, Y. A.; Bo, X. Z.; Sturm, J. C.; Norris, D. J. *Nature* **2001**, *414*, 289.
- (41) Jiang, P.; Bertone, J. F.; Hwang, K. S.; Colvin, V. L. *Chemistry of Materials* **1999**, *11*, 2132.
- (42) Wong, S.; Kitaev, V.; Ozin, G. A. *Journal of the American Chemical Society* **2003**, *125*, 1559.
- (43) Garcia-Santamaria, F.; Lopez, C.; Lopez-Tejeira, F.; Sanchez-Dehesa, J.; Miyazaki, H. T.. *Applied Physics Letters* **2001**, *79*, 2309.
- (44) Lee, W. M.; Pruzinsky, S. A.; Braun, P. V. *Advanced Materials* **2002**, *14*, 271.
- (45) Lopez, C. *Advanced Materials* **2003**, *15*, 1679.
- (46) Arsenault, A. *Journal of Materials Chemistry* **2004**, *14*, 781.
- (47) De Stefano, L.; Moretti, L.; Lamberti, O.; Rozzhia, M.; Rossi, A. M.; Arcari, P.; Rendina, I. *IEEE Transactions on Nanotechnology* **2004**, *3*, 49.
- (48) Endo, T.; Yanagida, Y.; Hatsuzawa, T. *Sensors and Actuators B* **2007**, *125*, 589.
- (49) Fang, X. Y.; Hsiao, V. K. S.; Chodavarpu, V. P.; Titus, A. H.; Cartwright, A. N. *IEEE Sensors Journal* **2006**, *6*, 661.
- (50) Hidalgo, N.; Calvo, M. E.; Colodrero, S. Miguez, H. *IEEE Sensors Journal* **2010**, *10*, 1206.
- (51) Hutter, T.; Ruschin, S. *IEEE Sensors Journal* **2010**, *10*, 97.
- (52) Karacali, T.; Alanyalioglu, M.; Efeoglu, H. *IEEE Sensors Journal* **2009**, *9*, 1667.
- (53) King, B. H.; Ruminski, A. M.; Snyder, J. L.; Sailor, M. J. *Advanced Materials* **2007**, *19*, 4530.
- (54) King, B. H.; Gramada, A.; Link, J. R.; Sailor, M. J. *Advanced Materials* **2007**, *19*, 4044.
- (55) Kobler, J.; Lotsch, B. V.; Ozin, G. A.; Bein, T. *ACS Nano* **2009**, *3*, 1669.
- (56) Levitsky, I. A.; Euler, W. B.; Tokranova, N.; Rose, A. *Applied Physics Letters* **2007**, *90*, 41904.

- (57) Lin, V. S. Y.; Motesharei, K. Dancil, K. P. S.; Salor, M. J.; Ghadiri, M. R. *Science* **1997**, 278, 840.
- (58) Ruminski, A. M.; Moore, M. M.; Sailor, M. J. *Advanced Functional Materials* **2008**, 18, 3418.
- (59) Saha, H.; Pramanik, C. *Materials and Manufacturing Processes* **2006**, 21, 239.
- (60) Salem, M. S.; Salior, M. J.; Harraz, F. A.; Sakka, T.; Ogata, Y. H. *Applied Physics Letters* **2006**, 100, 83520.
- (61) Potyrailo, R. A.; Ghiradella, H.; Vertiatchikh, A. Dovidenko, K.; Cournoyer, J. R.; Olson, E. *Nature Photonics* **2007**, 1, 123.
- (62) Gregg, S. J.; Sing, K. S. W. *Adsorption, Surface Area and Porosity, 2nd education* **1982**.
- (63) Coasne, B.; Grosman, A.; Ortega, C.; Simon, M. *Physical Review Letters* **2002**, 88, 256102.
- (64) Fisher, L. R.; Gamble, R. A.; Middlehurst, J. *Nature* **1981**, 290, 575.
- (65) Gemici, Z.; Schwachulla, P. I.; Williamson, E. H.; Rubner, M. F.; Cohen, R. E. *Nano Letters* **2009**, 1064, 2099.
- (66) Agnihotry, S. A.; Singh, P.; Joshi, A. G.; Singh, D. P.; Sood, K. N.; Shivaprasad, K. N. *Electrochimica Acta* **2006**, 51, 4291.
- (67) Anders, A.; Slack, J. I.; Richardson, T. J. *Thin Solid Films* **2008**, 517, 1021.
- (68) Avendano, E.; Azen, A.; Niklasson, G. A.; Graqvist, C. G. *Solar Energy Materials and Solar Cells* **2004**, 84, 337.
- (69) Avendano, E.; Berggren, L.; Niklasson, G. A.; Graqvist, C. G.; Azens, A. *Thin Solid Films* **2006**, 496, 30.
- (70) Avendano, E.; Azen, A.; Niklasson, G. A.; Graqvist, C. G. *Materials Science and Engineering B* **2007**, 138, 112.
- (71) Azens, A.; Kullman, L.; Vaivars, G.; Nordberg, H.; Granqvist, C. G.. *Solid State Ionics* **1998**, 113, 449.
- (72) Backholm, J.; Azens, A.; Niklasson, G. A. *Solar Energy Materials and Solar Cells* **2006**, 90, 414.
- (73) Backholm, J.; Avendano, E.; Azens, A.; de M Azevedo, G.; Coronel, E.; Niklasson, G. A.; Graqvist, C. G. *Solar Energy Materials and Solar Cells* **2008**, 92, 91.

- (74) Backholm, J.; Niklasson, G. A. *Solar Energy Materials and Solar Cells* **2008**, *92*, 1388.
- (75) Bange, K. *Solar Energy Materials and Solar Cells* **1999**, *58*, 1.
- (76) Bao, S.; Yamada, Y.; Okada, M.; Yoshimura, K. *Applied Surface Science* **2007**, *253*, 6268.
- (77) Bao, S.; Tajima, K.; Yamada, Y.; Okada, M.; Yoshimura, K. *Applied Physics A* **2007**, *87*, 621.
- (78) Bao, S.; Tajima, K.; Yamada, Y.; Okada, M.; Yoshimura, K. *Solar Energy Materials and Solar Cells* **2008**, *92*, 216.
- (79) Bao, S.; Tajima, K.; Yamada, Y.; Okada, M.; Yoshimura, K. *Solar Energy Materials and Solar Cells* **2008**, *92*, 224.
- (80) Bechinger, C.; Gregg, B. A. *Solar Energy Materials and Solar Cells* **1988**, *54*, 405.
- (81) Bullock, J. N.; Bechinger, C.; Benson, D. K.; Branz, H. M. *Journal of Non-Crystalline Solids* **1996**, *198*, 1163.
- (82) Cupelli, D.; Nicoletta, F. P.; Manfredi, S.; De Filpo, G.; Chidichimo, G. *Solar Energy Materials and Solar Cells* **2009**, *93*, 329.
- (83) Chen, K. C.; Chen, F. R.; Kai, J.-J. *Electrochimica Acta* **2007**, *52*, 3330.
- (84) Deb, S. K.; Lee, S.-H.; Tracy, C. E.; Pitts, J. R.; Gregg, B. A.; Branz, H. M. *Electrochimica Acta* **2001**, *46*, 2125.
- (85) Deb, S. K. *Solar Energy Materials and Solar Cells* **2008**, *92*, 245.
- (86) Deepa, M.; Ahmad, S.; Sood, K. N.; Alam, J.; Ahmad, S.; Srivastava, A. K. *Electromic Acta* **2007**, *52*, 7453.
- (87) Gao, W.; Lee, S.-H.; Bullock, J.; Xy, Y.; Benson, D. K.; Morrison, S.; Branz, H. M. *Solar Energy Materials and Solar Cells* **1999**, *59*, 243.
- (88) Gardiner, D. J.; Morris, S. M.; Coles, H. J. *Solar Energy Materials and Solar Cells* **1981**, *290*, 575.
- (89) Gerog, A.; George, A.; Craf, W.; Wittwer, V. *Vacuum* **2008**, *82*, 730.
- (90) Goldner, R. B.; Hass, T. E.; Seward, G.; Wong, K. K.; Norton, P.; Foley, G.; Berera, G.; Wei, G.; Schulz, S.; Chapman, R. *Solid State Ionics* **1998**, *28*, 1715.
- (91) Granqvist, C. G. *Solar Energy Materials and Solar Cells* **2008**, *92*, 203.

- (92) Li, X. M.; Reinhoudt, D.; Crego-Calama, M. *Chemical Society Reviews* **2007**, *36*, 1350.
- (93) Liu, M. J.; Zheng, Y. M.; Zhai, J.; Jiang, L. *Accounts of Chemical Research* **2010**, *43*, 368.
- (94) Ma, M. L.; Hill, R. M. *Current Opinion in Colloid and Interface Science* **2006**, *11*, 193.
- (95) Roach, P.; Shirtcliffe, N. J.; Newton, M. I. *Soft Matter* **2008**, *4*, 224.
- (96) Zhang, X.; Shi, F.; Niu, J.; Jiang, Y. G.; Wang, Z. Q. *Journal of Materials Chemistry* **2008**, *18*, 261.
- (97) Genzer, J.; Efimenko, K. *Biofouling* **2006**, *22*, 239.
- (98) Cebeci, F. C.; Wu, Z. Z.; Zhai, L.; Cohen, R. E.; Rubner, M. F. *Langmuir* **2006**, *22*, 2856.
- (99) Gao, X. F.; Yan, X.; Yao, X.; Xu, L.; Zhang, K.; Zhang, J. H.; Yang, B.; Jiang, L. *Advanced Materials* **2007**, *19*, 2213.
- (100) Tsougeni, K.; Papageorgiou, D.; Tserepi, A.; Gogolides, E. *Lab Chip* **2010**, *10*, 262.
- (101) Boreyko, J. B.; Chen, C. H. *Physical Review Letters* **2009**, *203*, 174502.
- (102) Han, Y. H.; Levkin, P.; Abarientos, I.; Liu, H. W.; Svec, F.; Frechet, J. M. *Journal of Analytical Chemistry* **2010**, *82*, 2520.
- (103) Barkhudarov, P. M.; Shah, P. B.; Watkins, E. B.; Doshi, D. A.; Brinker, C. J.; Majewski, J. *Journal of Corrosion Science and Engineering* **2008**, *50*, 897.
- (104) Xu, Q. F.; Wang, J. N. *New Journal of Chemistry* **2009**, *33*, 734.
- (105) Choi, W.; Tuteja, A.; Mabry, J. M.; Cohen, R. E.; McKinley, G. H. *Journal of Science and Interface Science* **2009**, *339*, 2008.
- (106) Ma, M. L.; Gupta, M.; Li, Z.; Zhai, L.; Gleason, K. K.; Cohen, R. E.; Rubner, M. F.; Rutledge, G. C. *Advanced Materials* **2007**, *19*, 255.
- (107) Zhai, L.; Cebeci, F. C.; Cohen, R. E.; Rubner, M. F. *Nano Letters* **2004**, *4*, 1349.
- (108) Oner, D.; McCarthy, T. J. *Langmuir* **2000**, *16*, 777.
- (109) Krupenkin, T. N.; Taylor, J. A.; Schneider, T. M.; Yang, S. *Langmuir* **2004**, *20*, 3832.
- (110) Furstner, R.; Barthlott, W.; Neinhuis, C.; Walzel, P. *Langmuir* **2005**, *21*, 956.

- (111) Krupenkin, T. N.; Taylor, J. A.; Wang, E. N.; Kolodner, P.; Hodes, M.; Salamon, T. R. *Langmuir* **2007**, *23*, 9128.
- (112) Xie, Q. D.; Fan, G. Q.; Zhao, N.; Guo, X. L.; Xu, J.; Dong, J. Y.; Zhang, L. Y.; Zhang, Y. J.; Han, C. C. *Advanced Materials* **2004**, *16*, 1830.
- (113) Zhao, N.; Xie, Q. D.; Weng, L. H.; Wang, S. Q.; Zhang, X. Y.; Xu, J. *Macromolecules* **2005**, *38*, 8996.
- (114) Han, D. W.; Steckl, A. J. *Langmuir* **2009**, *25*, 9454.
- (115) Wu, H.; Zhang, R.; Sun, Y.; Lin, D. D.; Sun, Z. Q.; Pan, W.; Downs, P. *Soft Matter* **2008**, *4*, 2429.
- (116) Zhan, N. Q.; Li, Y. X.; Zhang, C. Q.; Song, Y.; Wang, H. G.; Sun, L.; Yang, Q. B.; Hong, X. J. *Journal of Colloid and Interface Science* **2010**, *4*, 391.
- (117) Park, S. G.; Moon, H. H.; Lee, S. K.; Shim, J.; Yang, S. M. *Langmuir* **2010**, *26*, 1468.
- (118) Yan, H.; Kurogi, K.; Mayama, H.; Tsujii, K. *Angewandte Chemie International Edition* **2005**, *44*, 3453.
- (119) Zhang, X.; Shi, F.; Yu, X.; Liu, H.; Fu, Y.; Wang, Z. Q.; Jiang, L.; Li, X. Y. *Journal of the American Chemical Society* **2004**, *26*, 3004.
- (120) Yabu, H.; Shimomura, M. *Chemistry of Materials* **2005**, *17*, 5231.
- (121) Yabu, H.; Takebayashi, M.; Tanaka, M.; Shimomura, M. *Langmuir* **2005**, *21*, 3235.
- (122) Levkin, P. A.; Svec, F.; Frechet, J. M. *Advanced Functional Materials* **2009**, *19*, 1993.
- (123) Tung, P. H.; Kuo, S. W.; Jeong, K. U.; Cheng, S. Z. D.; Huang, C. F.; Chang, F. C. *Macromolecular Rapid Communications* **2007**, *28*, 271.
- (124) Tsoi, S. F.; Fok, E.; Sit, J. C.; Veinot, J. G. C. *Chemistry of Materials* **2006**, *18*, 5260.
- (125) Erbil, H. Y.; Demirel, A. L.; Avci, Y.; Mert, O. *Science* **2003**, *299*, 1377.
- (126) Han, J. T.; Lee, D. H.; Ryu, C. Y.; Cho, K. W. *Journal of the American Chemical Society* **2004**, *126*, 4796.
- (127) Bhagat, S. D.; Oh, C. S.; Kim, Y. H.; Ahn, Y. S.; Yeo, J. G. *Microporous Mesoporous Materials* **2007**, *100*, 3050.

- (128) Latthe, S. S.; Imai, H.; Ganesan, V.; Rao, A. V. *Microporous Mesoporous Materials* **2010**, *130*, 115.
- (129) Shirtcliffe, N. J.; McHale, G.; Newton, M. I.; Perry, C. C.; Roach, P. *Materials Chemistry and Physics* **2007**, *103*, 112.
- (130) Aulin, C.; Yun, S. H.; Wagberg, L.; Lindstrom, T. *ACS Applied Materials & Interfaces* **2009**, *1*, 2443.
- (131) Cao, L. L.; Price, T. P.; Weiss, M.; Gao, D. *Langmuir* **2008**, *24*, 1640.
- (132) Lai, Y. K.; Huang, Y. X.; Wang, H.; Huang, J. Y.; Chen, Z.; Lin, C. J. *Colloids and Surfaces B* **2010**, *76*, 117.
- (133) Lee, E. J.; Kim, J. J.; Cho, S. O. *Langmuir* **2010**, *26*, 3024.
- (134) Ran, C. B.; Ding, G. Q.; Liu, W. C.; Deng, Y.; Hou, W. T. *Langmuir* **2008**, *24*, 9552.
- (135) Zhu, S. J.; Li, Y. F.; Zhang, J. H.; Lu, C. L.; Dai, X.; Jia, F.; Gao, H. N.; Yang, B. *Journal of Colloidal and Interface Science* **2010**, *344*, 541.
- (136) Li, Y.; Duan, G. T.; Cai, W. P. *Journal of Colloidal and Interface Science* **2007**, *314*, 615.
- (137) Lee, E. J.; Lee, H. M.; Li, Y.; Hong, L. Y.; Kim, D. P.; Cho, S. O. *Macromolecular Rapid Communications* **2007**, *28*, 246.
- (138) Shiu, J. Y.; Kuo, C. W.; Chen, P. L.; Mou, C. Y. *Chemistry of Materials* **2004**, *16*, 541.
- (139) Zhang, L.; Zhou, Z. L.; Cheng, B.; DeSimone, J. M.; Samulski, E. T. *Langmuir* **2006**, *22*, 8576.
- (140) Wang, J. X.; Hu, J. P.; Wen, Y. Q.; Song, Y. L.; Jiang, L. *Chemistry of Materials* **2006**, *18*, 4984.
- (141) Tsai, H. J.; Lee, Y. L. *Langmuir* **2007**, *23*, 12687.
- (142) Xiu, Y. H.; Zhu, L. B.; Hess, D. W.; Wong, C. P. *Langmuir* **2006**, *22*, 9676.
- (143) Zhao, Y.; Li, M.; Lu, Q. H.; Shi, Z. Y. *Langmuir* **2008**, *24*, 12651.
- (144) Zhang, G.; Wang, D. Y.; Gu, Z. Z.; Mohwald, H. *Langmuir* **2005**, *21*, 9143.
- (145) Ming, W.; Wu, D.; van Benthem, R.; de With, G. *Nano Letters* **2005**, *5*, 2298.
- (146) Brozell, A. M.; Muha, M. A.; Abed-Amoli, A.; Bricarello, D.; Parikh, A. N. *Nano Letters* **2007**, *7*, 3822.

- (147) Wang, J. X.; Wen, Y. Q.; Hu, J. P.; Song, Y. L.; Jiang, L. *Advanced Functional Materials* **2007**, *17*, 219.
- (148) Kim, S. H.; Lee, S. Y.; Yang, S. M. *Angewandte Chemie International Edition* **2010**, *49*, 2535.
- (149) Min, W. L.; Jiang, B.; Jiang, P. *Advanced Materials* **2008**, *20*, 3914.
- (150) Li, J.; Fu, J.; Cong, Y.; Wu, Y.; Xue, L. J.; Han, Y. C. *Applied Surface Science* **2006**, *252*, 2229.
- (151) Gu, Z. Z.; Uetsuka, H.; Takahashi, K.; Nakajima, R.; Onishi, H.; Fujishima, A.; Sato, O. *Angewandte Chemie International Edition* **2003**, *42*, 894.
- (152) Li, H. L.; Wang, J. X.; Yang, L. M.; Song, Y. L. *Advanced Functional Materials* **2008**, *18*, 3258.
- (153) Sato, O.; Kubo, S.; Gu, Z. Z. *Accounts of Chemical Research* **2009**, *42*, 1.
- (154) Blanco, A.; Chomski, E.; Grabtchak, S.; Ibisate, M.; John, S.; Leonard, S. W.; Lopez, C.; Meseguer, F.; Miguez, H.; Mondia, J. P.; Ozin, G. A.; Toader, O.; van Driel, H. M. *Nature* **2000**, *405*, 437.
- (155) Vlasov, Y. A.; Bo, X. Z.; Sturm, J. C.; Norris, D. J. *Nature* **2001**, *414*, 289.
- (156) Liu, L.; Li, P. S.; Asher, S. A. *Nature* **1999**, *397*, 141.
- (157) Nykypanchuk, D.; Strey, H. H.; Hoagland, D. A. *Science* **2002**, *297*, 987.
- (158) Qian, W. P.; Gu, Z. Z.; Fujishima, A.; Sato, O. *Langmuir* **2002**, *18*, 4526.
- (159) Jin, G.; Jeng, H. W.; Bradford, H.; Englande, A. J. *Water Environment Research* **2004**, *76*, 245.
- (160) Payne, M. J.; Campbell, S.; Patchett, R. A.; Kroll, R. G. *Journal of Applied Bacteriology* **1992**, *73*, 41.
- (161) Lin, S.; Guo, Z.; Wu, H.-F.; Liu, Y.; Yang, Z.; Woo, C. H. *Analytical and Bioanalytical Chemistry* **2010**, *397*, 2465.
- (162) Bobbitt, J. A.; Betts, R. P. *Journal of Microbiological Methods* **1992**, *16*, 215.
- (163) Lin, C. C.; Yeh, Y. C.; Yang, C. Y.; Chen, C. L.; Chen, G. F.; Chen, C. C.; Wu, Y. C. *Journal of the American Chemical Society* **2002**, *124*, 3508.
- (164) Gu, H. W.; Xu, K. M.; Xu, C. J.; Xu, B. *Chemical Communications* **2006**, *56*, 941.
- (165) Tartaj, P.; Morales, M. P.; González-Carreño, T.; Veintemillas-Verdaguer, S.; Serna, C. J. *Journal of Magnetism and Magnetic Materials* **2005**, *290*, 28.

- (166) Ho, K. C.; Tsai, P. J.; Lin, Y. S.; Chen, Y. C. *Analytical Chemistry* **2004**, *76*, 7162.
- (167) Shields, P.A., Berenfeid, S.A. and Farrah, S.R. *Applied and Environmental Microbiology* **1985**, *49*, 453.
- (168) Tanny, G.B., Mirelman, D. and Pistole, T. *Applied and Environmental Microbiology* **1980**, *40*, 269.
- (169) Payne, M. J.; Campbell, S.; Patchett, R. A.; Kroll, R. G. *Journal of Applied Bacteriology* **1992**, *73*, 41.
- (170) Ochoa, M. L.; Harrington, P. B. *Analytical Chemistry* **2005**, *77*, 5258.
- (171) Lin, C. C.; Yeh, Y. C.; Yang, C. Y.; Chen, C. L.; Chen, G. F.; Chen, C. C.; Wu, Y. C. *Journal of the American Chemical Society* **2002**, *124*, 3508.
- (172) Liu, J. C.; Chen, W. J.; Li, C. W.; Mong, K. K. T.; Tsai, P. J.; Tsai, T. L.; Lee, Y. C.; Chen, Y. C. *Analyst* **2009**, *134*, 2084.
- (173) Bundy, J.; Fenselau, C. *Analytical Chemistry* **1999**, *71*, 1460.
- (174) Bundy, J.; Fenselau, C. *Analytical Chemistry* **2001**, *73*, 571.
- (175) Afonso, C.; Fenselau, C. *Analytical Chemistry* **2003**, *75*, 694.
- (176) Mistler, R. E.; Twiname, E. R. *Tape Casting: Theory and Practice; American Ceramic Society: Westerville, OH* **2000**.
- (177) Chou, Y. T.; Ko, Y. T.; Yan, M. F. J. *Journal of the American Chemical Society* **1987**, *70*, 280.
- (178) Loest, H.; Lipp, R.; Mitsoulis, E. J. *Journal of the American Chemical Society* **1994**, *77*, 254.
- (179) Pitchumani, R.; Karbhari, V. M. *Journal of the American Chemical Society* **1995**, *78*, 2497.
- (180) Kim, H. J.; Krane, M. J. M.; Trumble, K. P.; Bowman, K. J. *Journal of the American Chemical Society* **2006**, *89*, 2769.
- (181) Prevo, B. G.; Velev, O. D. *Langmuir* **2004**, *20*, 2099.
- (182) Adachi, E.; Nagayama, K. *Langmuir* **1996**, *12*, 1836.
- (183) Dimitrov, A. S.; Nagayama, K. *Langmuir* **1996**, *12*, 1303.
- (184) Matsushita, S.; Miwa, T.; Fujishima, A. *Langmuir* **1997**, *13*, 2585.

- (185) Stober, W.; Fink, A.; Bohn, E. *Journal of Colloidal and Interface Science* **1968**, 26, 62.
- (186) Min, W. L.; Jiang, P.; Jiang, B. *Nanotechnology* **2008**, 19, 475604.
- (187) Bogush, G. H.; Tracy, M. A.; Zukoski, C. F. *Journal of Non-Crystalline Solids* **1988**, 104, 95.
- (188) Johnson, S. A.; Ollivier, P. J.; Mallouk, T. E. *Science* **1999**, 283, 963.
- (189) Arriagada, F. J.; Osseo-Asare, K. *Journal of Colloidal and Interface Science* **1999**, 211, 210.
- (190) Bird, R. B.; Stewart, W. E.; Lightfoot, E. N. *Transport Phenomena; 2nd ed.*; Wiley: Chichester, NY **1999**.
- (191) Vermant, J.; Solomon, M. J. *Journal of Physics Condensed Matter* **2005**, 17, R187.
- (192) Ackerson, B. J. *Journal of Physics Condensed Matter* **1990**, 2, SA389.
- (193) Jiang, P.; Hwang, K. S.; Mittleman, D. M.; Bertone, J. F.; Colvin, V. L. *Journal of the American Chemical Society* **1999**, 121, 11630.
- (194) Yang, H.; Jiang, P. *Langmuir* **2010**, 26, 13173.
- (195) Mittleman, D. M.; Bertone, J. F.; Jiang, P.; Hwang, K. S.; Colvin, V. L. *Journal of Chemical Physics* **1999**, 111, 345.
- (196) Watanabe, S.; Inukai, K.; Mizuta, S.; Miyahara, M. T. *Langmuir* **2009**, 25, 7287.
- (197) Lide, D. R.; Frederikse, H. P. R. *CRC Handbook of Chemistry and Physics, 76<sup>th</sup> ed.* Boca Raton, FL **1995**.
- (198) Zhang, Z.; Satpathy, S. *Physics Review Letters* **1990**, 65, 2650.
- (199) Bertone, J. F.; Jiang, P.; Hwang, K. S.; Mittleman, D. M.; Colvin, V. L. *Physics Review Letters* **1999**, 83, 300.
- (200) Sobhan, M. A.; Kivisa, R. T.; Stjerna, B.; Granqvist, C. G. *Solar Energy Materials and Solar Cells* **1996**, 44, 451.
- (201) Pluddemann, E. P. *Silane Coupling Agents, 2<sup>nd</sup> ed.*; Plenum Press; New York **1991**.
- (202) Houle, F. A.; Pettner, C. T.; Miller, D. C.; Sooriyakumaran, R. *Applied Physics Letters* **2007**, 90, 213103.
- (203) Velev, O. D.; Jede, T. A.; Lobo, R. F.; Lenhoff, A. M. *Nature* **1997**, 389, 447.

- (204) Miwa, M.; Nakajima, A.; Fujishima, A.; Hashimoto, K.; Watanabe, T. *Langmuir* **2000**, *16*, 5754.
- (205) Cassie, A. B. D.; Baxter, S. *Transactions of the Faraday Society* **1944**, *40*, 546.
- (206) Wenzel, R. N. *Industrial & Engineering Chemistry Research* **1936**, *28*, 588.
- (207) Weissman, J. M.; Sunkara, H. B.; Tse, A. S.; Asher, S. A. *Science* **1996**, *274*, 959.
- (208) Pan, G. S.; Kesavamoorthy, R.; Asher, S. A. *Physics Review Letters* **1997**, *78*, 3860.
- (209) Kim, S. H.; Jeong, W. C.; Yang, S. M. *Chemistry of Materials* **2009**, *21*, 4993.

## BIOGRAPHICAL SKETCH

Hongta Yang received a bachelor's degree in chemical engineering from National Taiwan University in 2001, a master's degree in chemical engineering from New Jersey Institute of Technology in 2006, and a master's degree in paper science and engineering from the Georgia Institute of Technology in 2008. He began his graduate studies at the University of Florida in August 2008 and joined Professor Peng Jiang's nanostructured material research group to pursue a doctorate degree. He graduated in the spring of 2011 after spending two and half years being educated in chemical engineering and material science.